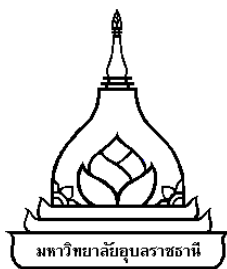


**NOVEL BENZOCHROMENE AND THIOARENE
FOR ORGANIC ELECTRONIC DEVICES**

THIKHAMPORN UPPALABAT

**A THESIS SUBMITTED IN PARTIAL FULFILLMENT OF THE REQUIREMENTS
FOR THE DEGREE OF MASTER OF SCIENCE
MAJOR IN CHEMISTRY
FACULTY OF SCIENCE
UBON RATCHATHANI UNIVERSITY
ACADEMIC YEAR 2018
COPYRIGHT OF UBON RATCHATHANI UNIVERSIT**



UBON RATCHATHANI UNIVERSITY
THESIS APPROVAL
MASTER OF SCIENCE
MAJOR IN CHEMISTRY FACULTY OF SCIENCE

TITLE NOVEL BENZOCHROMENE AND THIOARENE FOR ORGANIC
ELECTRONIC DEVICES

AUTHOR MISS THIKHAMPORN UPPALBAT

EXAMINATION COMMITTEE

DR. SOMBOON SAHASITHIWAT	CHAIRPERSON
ASST. PROF. DR. RUKKIAT JITCHATI	MEMBER
ASST. PROF. DR. KITTIYA WONGKHAN	MEMBER

ADVISORS

.....
(ASST. PROF. DR. RUKKIAT JITCHATI)

.....
(ASST. PROF. DR. CHARIDA PUKAHUTA)
DEAN, FACULTY OF SCIENCE

.....
(ASSOC. PROF. DR. ARIYAPORN PONGRAT)
VICE PRESIDENT FOR ACADEMIC AFFAIRS

COPYRIGHT OF UBON RATCHATHANI UNIVERSITY
ACADEMIC YEAR 2018

ACKNOWLEDGEMENTS

Firstly, I would like to thank my advisor; Asst. Prof. Dr. Rukkiat Jitchati for his guidance and encouragement. He has truly shared his generously valuable time and expertise to provide insight and constructive suggestions throughout the course of this work. The help has enabled me to carry out my work successfully. Many thank to Asst. Prof. Dr. Kittiya Wongkhan for her comments and suggestions in completion of the thesis.

I also would like to thank Dr. Somboon Sahasithiwat and Mrs. Laongdao Kangkeaw from National Metal and Materials Technology Center (MTEC) for their content advice and sharing their extensive knowledge about the fabrication of OLEDs and OFETs device. I would like to acknowledge the Organometallic and Catalytic Center (OCC), Department of Chemistry, Faculty of Science, Ubon Ratchathani University for the synthesis facilities. I am grateful to the financial support from the Science Achievement Scholarship of Thailand (SAST) for providing all laboratory facilities.

Finally, I must express my deepest gratitude to my family for their always encouraged me to pursue my goals, always succeed, and never admit defeat. Thanks everyone in the RJ & KW group for contributed and helped me to make this research work possible at Ubon Ratchathani University.

Thikhamporn Uppalabat
Researcher

บทคัดย่อ

เรื่อง : สารเบนโซโครมีนและไทโอเอรีนชนิดใหม่สำหรับอุปกรณ์อิเล็กทรอนิกส์ชนิดสารอินทรีย์

ผู้วิจัย : ทิฆัมพร อุปลาบัติ

ชื่อปริญญา : วิทยาศาสตร์มหาบัณฑิต

สาขาวิชา : เคมี

อาจารย์ที่ปรึกษา: ผู้ช่วยศาสตราจารย์ ดร. รักเกียรติ จิตคตติ

คำสำคัญ : ไดโอดเปล่งแสงชนิดสารอินทรีย์, ทรานซิสเตอร์สนามไฟฟ้าชนิดสารอินทรีย์, เบนโซโครมีน, ไทโอเอรีน, ระบบไฟคอนจูเกต

การออกแบบและพัฒนาโครงสร้างสารอินทรีย์ด้วยระบบไฟ-คอนจูเกตกำลังเป็นที่ได้รับความสนใจอย่างกว้างขวาง เพื่อใช้เป็นวัสดุในชิ้นงานอุปกรณ์อิเล็กทรอนิกส์ชนิดสารอินทรีย์ อาทิ อุปกรณ์ไดโอดเปล่งแสงชนิดสารอินทรีย์ และอุปกรณ์ทรานซิสเตอร์สนามไฟฟ้าชนิดสารอินทรีย์ เป็นต้น ในการวิจัยนี้ได้ทำการสังเคราะห์ไฟ-คอนจูเกตของอนุพันธ์เบนโซโครมีน (ARAR2 และ ARAR3) และอนุพันธ์ไทโอเอรีน (ARTH2, ARTH3 และ THTH2) ผ่านปฏิกิริยาคู่ควบโซโนกาซิระ ปฏิกิริยาคู่ควบโดยตรง ปฏิกิริยาการปิดวงด้วยโลหะรูทีเนียม และปฏิกิริยาสกอลล์ ตามลำดับ ซึ่งสารโมเลกุลเป้าหมายทั้งหมดถูกนำไปพิสูจน์เอกลักษณ์ด้วย $^1\text{H NMR}$, $^{13}\text{C NMR}$, FT-IR และแมส สเปกโตรสโคปี นอกจากนี้สาร ARTH2 ยังถูกยืนยันโครงสร้างทางเคมีด้วย 2D NMR (เทคนิค COSY และ HMBC) สำหรับการศึกษาคุณสมบัติทางแสงของสารโมเลกุลเป้าหมาย พบว่าสารทั้งหมดเกิดการคายแสงในช่วงของแสงสีเขียวผ่านกระบวนการการคายแสงแบบฟลูออเรสเซนซ์ จากนั้นทำการศึกษาคูสมบัติทางความร้อนของสารโมเลกุลเป้าหมาย พบว่าสารที่เป็นอนุพันธ์ของไทโอเอรีน (ARTH2, ARTH3 และ THTH2) จะมีเสถียรภาพทางความร้อนสูง หลังจากนั้นสารโมเลกุลเป้าหมายทั้งหมดถูกนำไปศึกษาประสิทธิภาพการเป็นชิ้นงานอุปกรณ์ไดโอดเปล่งแสงชนิดสารอินทรีย์ โดยใช้โครงสร้างเป็น ITO/NPB/MADN: 20 %wt ของสารโมเลกุลเป้าหมาย/Bphen/LiF/Al พบว่าสาร ARTH2 ให้ประสิทธิภาพที่ดีที่สุดและคายแสงในช่วงของแสงสีเขียวเหลือง ด้วยค่าการเปล่งแสงสูงสุดเท่ากับ $4,699 \text{ cd/m}^2$ ค่าประสิทธิภาพเชิงกระแสและค่าประสิทธิภาพเชิงกำลังไฟฟ้าเท่ากับ 2.71 cd/A และ 0.79 Lm/W ตามลำดับ นอกจากนี้สารโมเลกุลเป้าหมายทั้งหมดยังถูกนำไปศึกษาประสิทธิภาพการเป็นชิ้นงานอุปกรณ์ทรานซิสเตอร์สนามไฟฟ้าชนิดสารอินทรีย์ ซึ่งพบว่าสาร THTH2 แสดงคุณสมบัติการเป็นทรานซิสเตอร์ชนิดบวกด้วยค่าสภาพคล่องทางไฟฟ้าเท่ากับ $1.64 \times 10^{-2} \text{ cm}^2/\text{Vs}$ และอัตราส่วนกระแสไฟฟ้าเปิดและปิดเท่ากับ 6.48

ABSTRACT

TITLE : NOVEL BENZOCHROMENE AND THIOARENE FOR ORGANIC ELECTRONIC DEVICES
AUTHOR : THIKHAMPORN UPPALABAT
DEGREE : MASTER OF SCIENCE
MAJOR : CHEMISTRY
ADVISOR : ASST. PROF. RUKKIAT JITCHATI, Ph. D.
KEYWORDS : ORGANIC LIGHT EMITTING DIODES (OLEDs), ORGANIC FIELD EFFECT TRANSISTORS (OFETs), BENZOCHROMENE, THIOARENE, *PI*-CONJUGATED SYSTEM

Design and development of the organic structures with π -conjugated system were interested for using in electronic device such as organic light emitting diodes (OLEDs) and organic field effect transistors (OFETs). In this work, we synthesized π -conjugated of benzochromene (**ARAR2** and **ARAR3**) and thioarene (**ARTH2**, **ARTH3** and **THTH2**) derivatives via Sonogashira coupling, direct cross-coupling, ruthenium cyclization and Scholl reactions, respectively. All target compounds were characterized by ^1H NMR, ^{13}C NMR, FT-IR and mass spectroscopy. Moreover, the chemical structure of **ARTH2** was clearly characterized by 2D NMR (COSY and HMBC spectroscopy). The photophysical properties of target compounds showed photoluminescence emission which appeared in range of green regions with fluorescence process. The **ARTH2**, **ARTH3** and **THTH2** which are thioarene products showed a high thermal stability. After that, all target compounds were studied OLED performance by using the structure of ITO/NPB/MADN: 20 %wt of targeted compounds/Bphen/LiF/Al. The results indicated that **ARTH2** showed the best performance and exhibited yellowish green colour with maximum luminance at $4,699\text{ cd/m}^2$, current and power efficiencies at 2.71 cd/A and 0.79 Lm/W , respectively. In addition, the target compounds were investigated in OFETs. It was found that **THTH2** showed the p-type character with hole mobility of $1.64 \times 10^{-2}\text{ cm}^2/\text{Vs}$ and on/off current ratio of 6.48.

CONTENTS

	PAGE
ACKNOWLEDGEMENTS	I
THAI ABSTRACT	II
ENGLISH ABSTRACT	III
CONTENTS	IV
LIST OF SCHEMES	VI
LIST OF TABLES	VII
LIST OF FIGURES	VIII
LIST OF APPREVIATIONS	XV
CHAPTER 1 INTRODUCTION	
1.1 Organic light emitting diodes (OLEDs)	3
1.2 Organic field effect transistors (OFETs)	9
1.3 Objectives of thesis	12
CHAPTER 2 LITERATURE REVIEWS	13
CHAPTER 3 EXPERIMENTAL	21
3.1 Chemicals	21
3.2 Instruments	23
3.3 Synthesis	26
3.4 OLEDs device fabrication	34
3.5 OFETs device fabrication	37
CHAPTER 4 RESULTS AND DISCUSSIONS	
4.1 Synthesis and reaction mechanism	41
4.2 Characterization and structure identification	49
4.3 Photophysical study	61
4.4 Electrochemical study	68
4.5 Thermal study	71
4.6 OLEDs performance	72
4.7 OFETs performance	76

CONTENTS (CONTINUED)

	PAGE
CHAPTER 5 CONCLUSIONS	79
REFERENCES	81
APPENDICES	
A Characterized data	89
B Photophysical and electrochemical data	106
C Device performance data	120
D Publication	134
CURRICULUM VITAE	139

LIST OF SCHEMES

SCHEME		PAGES
4.1	The synthetic pathway for the target molecules	41
4.2	The conditions for used synthesis	42
4.3	Sonogashira reaction mechanism for ARAR1 , ARTH1 and TH1	43
4.4	Synthesis pathway for THTH1	44
4.5	Direct cross-coupling reaction mechanism for THTH1 and THTH1/1	45
4.6	Synthesis pathways for ARAR2 , ARTH2 and THTH2	46
4.7	Ruthenium cyclization reaction mechanism for ARAR2 , ARTH2 and THTH2	47
4.8	Synthesis pathways for ARAR3 and ARTH3	48
4.9	Scholl reaction mechanism for ARAR3 and ARTH3	48

LIST OF TABLES

TABLE		PAGES
3.1	Chemicals for the synthesis	21
3.2	Chemicals for OLEDs performance study	22
3.3	Chemicals for OFETs performance study	23
3.4	Instruments for the molecular characterization	23
3.5	Instruments for OLEDs study	24
3.6	Instruments for OFETs study	24
3.7	The optimization of intramolecular Scholl reaction	28
4.1	FT-IR characterization of all targeted	58
4.2	Characterization and structure identification for all compounds	59
4.3	The maximum absorption wavelengths of products in toluene solution	62
4.4	Photoluminescence characteristics of all products in toluene solution	67
4.5	Electrochemical property and energy levels of products	70
4.6	The optimization of OLEDs device fabrication	72
4.7	Summary of OLEDs performances of target compounds with configuration of ITO/NPB(30nm)/MADN: Dopant(20 %wt, 40nm)/Bphen(30nm)/LiF(0.5nm)/Al(100nm)	75
4.8	Summary of OFETs device performances with configurations of the materials investigated in this work	78

LIST OF FIGURES

FIGURE		PAGES
1.1	Examples of small organic molecules	1
1.2	Examples of organic polymeric molecules	2
1.3	Example of OLED displays	3
1.4	The multi-layer OLED structures	4
1.5	Schematic energy diagram of basic process in multi-layer OLED	4
1.6	Jablonski energy diagram	5
1.7	Electronic processes of host-guest molecules	6
1.8	Energy level relationship in guest-host systems	7
1.9	Luminance, current density and turn on voltage characteristic	7
1.10	The CIE 1931 color space chromaticity diagram	8
1.11	Examples of OFET in the future	9
1.12	OFET device configuration of bottom-gate-top-contact	9
1.13	Schematic description of the principle of operation for OFET	10
1.14	Threshold voltage, transfer curve and on/off current characteristics	11
1.15	Output characteristic	12
2.1	Benzo[<i>d,e</i>]chromene derivatives synthesis from iridium catalyst by Yan and co-worker	13
2.2	Benzo[<i>d,e</i>]chromene derivatives synthesis from rhodium catalyst by Wang and co-worker	14
2.3	Benzo[<i>d,e</i>]chromene derivatives synthesis from rhodium catalyst by Miura and co-worker	14
2.4	Benzo[<i>d,e</i>]chromene derivatives synthesis from rhodium catalyst by Tan and co-worker	14
2.5	Benzo[<i>d,e</i>]chromene derivatives synthesis from ruthenium catalyst by Xie and co-worker	15

LIST OF FIGURES (CONTINUED)

FIGURE		PAGES
2.6	Benzo[<i>d,e</i>]chromene derivatives synthesis from ruthenium catalyst by Thirunavukkarasu and co-worker	15
2.7	The structures and emission spectra of benzo[<i>d,e</i>]chromene derivatives by Mochida and co-worker	16
2.8	Benzo[<i>d,e</i>]chromene derivatives for OLEDs device by Miss Benjawan Somchob and co-worker	16
2.9	Thioarene derivatives synthesis from AlCl ₃ catalyst by Badger and co-worker	17
2.10	Thioarene derivatives synthesis from FeCl ₃ catalyst by Larsen and co-worker	17
2.11	Thioarene derivatives synthesis from FeCl ₃ catalyst by Jian and co-worker	18
2.12	The structure and photophysical property of thioarene derivatives by Daniel and co-worker	18
2.13	Thioarene derivatives for OFETs device by Lui and co-worker	19
2.14	Thioarene derivatives for OFETs device by Katz and co-workers	19
2.15	Thioarene derivatives for OFETs device by Yanming and co-worker	19
2.16	Thioarene derivatives for OFETs device by Takimiya and co-worker	20
2.17	Thioarene derivatives for OFETs device by Yamamoto and co-worker	20
3.1	Cleaning process of ITO substrate	35
3.2	Coating process of organic thin film	36
3.3	Coating process of cathode electrode	36
3.4	Cleaning process of Si/SiO ₂ substrate	38
3.5	Coating process of organic thin film	39

LIST OF FIGURES (CONTINUED)

FIGURE		PAGES
3.6	Coating process of source-drain-gate electrodes	39
4.1	Molecular structures of the target compounds	40
4.2	¹ H NMR in CDCl ₃ and the assignment of ARAR1	49
4.3	¹ H NMR in CDCl ₃ and the assignment of ARTH1	50
4.4	¹ H NMR in CDCl ₃ and the assignment of TH1	51
4.5	¹ H NMR in CDCl ₃ of mixed THTH1 and THTH1/1	52
4.6	¹³ C NMR in CDCl ₃ and the assignment of THTH1 and THTH1/1	53
4.7	¹ H NMR in CDCl ₃ and the assignment of five target products	54
4.8	¹³ C NMR in CDCl ₃ and the assignment of all target products	55
4.9	COSY spectrum in CDCl ₃ and the relation of ARTH2	56
4.10	HMBC spectrum in CDCl ₃ and the relation of ARTH2	57
4.11	UV-Visible absorption spectra of target products	62
4.12	UV-Visible absorption spectra and structures of ARAR2 and ARTH2	63
4.13	UV-Visible absorption spectra and structures of ARTH2 and THTH2	64
4.14	UV-Visible absorption spectra and structures of ARAR2 and ARAR3	65
4.15	UV-Visible absorption spectra and structures of ARAR3 and ARTH3	66
4.16	Photoluminescence spectra of target products	67
4.17	All target products in solid state (top) and solution (below) under UV lamp	68
4.18	Cyclic voltammogram of target products reported compared with ferrocene/ferrocenium ion	69
4.19	Schematic HOMO and LUMO levels of target products	70

LIST OF FIGURES (CONTINUED)

FIGURE		PAGES
4.20	TGA curves of target products	71
4.21	OLEDs device configuration (upper left), the relative HOMO and LUMO energy levels of the materials investigated in this work (upper right) and structures of NPB, MADN and Bphen (bottom)	73
4.22	Current density and luminance versus applied bias voltage of the device structure ITO/NPB(30nm)/MADN: Dopant(20 % wt, 40nm)/Bphen(30nm)/LiF(0.5nm)/ Al(100nm)	74
4.23	The relative HOMO and LUMO energy levels of ARTH2 device	75
4.24	CIE coordinates and emission colour for OLED devices of target compounds	76
4.25	OFETs device configuration in this work	77
4.26	Transfer curve (left) and output curve (right) of pentacene	77
4.27	Transfer curve (left) and output curve (right) of THTH2	78
A.1	¹ H NMR in CDCl ₃ and the assignment of ARAR2 , ARTH2 and THTH2	90
A.2	¹ H NMR in CDCl ₃ and the assignment of ARAR2 and ARAR3	90
A.3	¹ H NMR in CDCl ₃ and the assignment of ARTH2 and ARTH3	91
A.4	¹³ C NMR in CDCl ₃ and the assignment of ARAR2 , ARTH2 and THTH2	91
A.5	¹³ C NMR in CDCl ₃ and the assignment of ARAR2 and ARAR3	92
A.6	¹³ C NMR in CDCl ₃ and the assignment of ARTH2 and ARTH3	92
A.7	Mass spectra and the assignment of ARAR1	93
A.8	Mass spectra and the assignment of ARTH1	94

LIST OF FIGURES (CONTINUED)

FIGURE		PAGES
A.9	Mass spectra and the assignment of TH1	95
A.10	Mass spectra and the assignment of THTH1	96
A.11	Mass spectra and the assignment of THTH1/1	97
A.12	Mass spectra and the assignment of ARAR2	98
A.13	Mass spectra and the assignment of ARTH2	99
A.14	Mass spectra and the assignment of THTH2	100
A.15	Mass spectra and the assignment of ARAR3	101
A.16	Mass spectra and the assignment of ARTH3	102
A.17	FT-IR spectra and the assignment of ARAR2	103
A.18	FT-IR spectra and the assignment of ARTH2	103
A.19	FT-IR spectra and the assignment of THTH2	104
A.20	FT-IR spectra and the assignment of ARAR3	104
A.21	FT-IR spectra and the assignment of ARTH3	105
A.22	UV-Visible absorption spectra of all products	107
A.23	Lifetime spectra of ARAR2	109
A.24	Lifetime spectra of ARTH2	109
A.25	Lifetime spectra of THTH2	110
A.26	Lifetime spectra of ARAR3	110
A.27	Lifetime spectra of ARTH3	111
A.28	Fluorescence quantum yield spectra of ARAR2	111
A.29	Fluorescence quantum yield spectra of ARTH2	112
A.30	Fluorescence quantum yield spectra of THTH2	112
A.31	Fluorescence quantum yield spectra of ARAR3	113
A.32	Fluorescence quantum yield spectra of ARTH3	113
A.33	Cyclic voltammogram of ferrocene in acetonitrile	114
A.34	Reduction potentials of ARAR2 in acetonitrile	115
A.35	Reduction potentials of ARTH2 in acetonitrile	116

LIST OF FIGURES (CONTINUED)

FIGURE	PAGES
A.36 Reduction potentials of THTH2 in acetonitrile	117
A.37 Reduction potentials of ARAR3 in acetonitrile	118
A.38 Reduction potentials of ARTH3 in acetonitrile	119
A.39 OLEDs device fabrication and energy level diagram of ARAR2	121
A.40 Current density and luminance versus applied bias voltage (left) and current and power efficiencies (right) of ARAR2 device	121
A.41 PL, EL, CIE coordinate and emission colour of ARAR2 device	122
A.42 OLEDs device fabrication and energy level diagram of ARTH2	122
A.43 Current density and luminance versus applied bias voltage (left) and current and power efficiencies (right) of ARTH2 device	123
A.44 PL, EL, CIE coordinate and emission colour of ARTH2 device	123
A.45 OLEDs device fabrication and energy level diagram of THTH2	124
A.46 Current density and luminance versus applied bias voltage (left) and current and power efficiencies (right) of THTH2 device	124
A.47 PL, EL, CIE coordinate and emission colour of THTH2 device	125
A.48 OLEDs device fabrication and energy level diagram of ARAR3	125
A.49 Current density and luminance versus applied bias voltage (left) and current and power efficiencies (right) of ARAR3 device	126
A.50 PL, EL, CIE coordinate and emission colour of ARAR3 device	126

LIST OF FIGURES (CONTINUED)

FIGURE		PAGES
A.51	OLEDs device fabrication and energy level diagram of ARTH3	127
A.52	Current density and luminance versus applied bias voltage (left) and current and power efficiencies (right) of ARTH3 device	127
A.53	PL, EL, CIE coordinate and emission colour of ARTH3 device	128
A.54	Transfer curve at gate-source voltage 10 to -60 V of pentacene	129
A.55	Transfer curve (left) and output curve (right) of pentacene	129
A.56	Transfer curve at gate-source voltage 10 to -60 V of ARAR2	130
A.57	Transfer curve at gate-source voltage 10 to -60 V of ARTH2	130
A.58	Transfer curve at gate-source voltage 10 to -100 V of THTH2	131
A.59	Transfer curve (left) and output curve (right) of THTH2	131
A.60	Transfer curve at gate-source voltage 10 to -60 V of ARAR3	132
A.61	Transfer curve at gate-source voltage 10 to -60 V of ARTH3	133

LIST OF ABBREVIATIONS

ABBREVIATION	FULL WORD
AIE	Aggregation-induced emission
A	Ampere
Å	Angstrom
br	Broad
cd	Candela
C_i	Capacitance per unit area of the gate dielectric layer
^{13}C NMR	Carbon nuclear magnetic resonance spectroscopy
cm	Centimeter
L	Channel length
W	Channel width
δ	Chemical shift
CIE	Commission internationale de l'éclairage
COSY	Correlation spectroscopy
C	Coulomb
J	Coupling constant
J	Current density
J - V - L	Current density-voltage-luminance
CE, η_L	Current efficiency
CV	Cyclic voltammetry
°C	Degree Celsius
DFT	Density functional theory
Ru-cymene	Dichloro(<i>p</i> -cymene)ruthenium (II) dimer
Bphen	4,7-Diphenyl-1,10-phenanthroline
d	Doublet
I_{DS}	Drain-source current
V_{DS}	Drain-source voltage
V_D	Drain voltage

LIST OF ABBREVIATIONS (CONTINUED)

ABBREVIATION	FULL WORD
EL	Electroluminescence
ETL	Electron transport layer
eV	Electron volt
EML	Emission layer
E _g	Energy gap
E _{HOMO}	Energy level of HOMO
E _{LUMO}	Energy level of LUMO
eq.	Equivalent
FT-IR	Fourier-transform infrared spectroscopy
F	Farad
V _{GS}	Gate-source voltage
V _G	Gate voltage
GC	Glassy carbon electrode
g	Gram
E _{1/2, Fe/Fe+}	Half potential of ferrocene/ferrocenium redox couple
T _{sub}	Heat substrate
Hz	Hertz
HMBC	Heteronuclear multiple bond correlation spectroscopy
HOMO	Highest occupied molecular orbital
HTL	Hole transport layer
hr	Hour
ITO	Indium tin oxide
IC	Internal conversion
ISC	Intersystem crossing
τ	Lifetime
LCDs	Liquid crystal displays
LUMO	Lowest unoccupied molecular orbital

LIST OF ABBREVIATIONS (CONTINUED)

ABBREVIATION	FULL WORD
Lm	Lumen
<i>L</i>	Luminance
m/z	Mass/charge ratio
MS	Mass spectroscopy
$\lambda_{\text{max, abs}}$	Maximum absorption wavelength
$\lambda_{\text{max, em}}$	Maximum emission wavelength
λ_{max}	Maximum wavelength
M	Mega
m.p.	Melting point
MADN	2-Methyl-9,10-bis(naphthalen-2-yl)anthracene
μA	Microampere
μm	Micrometer
μmol	Micromole
mbar	Millibar
mg	Milligram
mL	Milliliter
mm	Millimeter
mmol	Millimole
mV	Millivolt
min	Minute
μ	Mobility
M	Molarity
m	Multiplet
nm	Nanometer
ns	Nanosecond
NPB	(<i>N,N'</i> -diphenyl)- <i>N,N'</i> -bis(<i>1</i> -naphthyl)- <i>1,1'</i> -biphenyl- 4,4'-diamine

LIST OF ABBREVIATIONS (CONTINUED)

ABBREVIATION	FULL WORD
NMR	Nuclear magnetic resonance spectroscopy
OTS	Octadecyltrichlorosilane
I_{on}/I_{off}	On/off current ratio
λ_{onset}	Onset of absorption spectra
$E_{ox, onset}$	Onset of oxidation potential
$E_{re, onset}$	Onset of reduction potential
OFETs	Organic field effect transistors
OLEDs	Organic light emitting diodes
ppm	Part per million
%	Percentage
PL	Photoluminescence
π	Pi
PE, η_P	Power efficiency
$^1\text{H NMR}$	Proton nuclear magnetic resonance spectroscopy
QY	Quantum yield
s	Second
σ	Sigma
Si/SiO ₂	Silicon wafer
s	Singlet
S	Singlet state
V_S	Source voltage
cm ²	Square centimeter (unit of surface)
m ²	Square meter (unit of surface)
TMS	Tetramethylsilane
TGA	Thermogravimetric analysis
TLC	Thin layer chromatography
V_T	Threshold voltage

LIST OF ABBREVIATIONS (CONTINUED)

ABBREVIATION	FULL WORD
t	Triplet
T	Triplet state
$V_{\text{turn on}}$	Turn-on voltage
2D NMR	Two-dimensional nuclear magnetic resonance spectroscopy
UV	Ultraviolet
V	Volt
% v/v	Volume/volume percent concentration
cm^{-1}	Wavenumber

CHAPTER 1

INTRODUCTION

Organic electronics is a field of materials science concerning the design, synthesis, characterization, and application of small organic molecules or polymers which shows desirable electronic properties such as high conductivity. Unlike conventional inorganic conductors and semiconductors, organic electronic materials are constructed from organic (carbon-based) small molecules or polymers using chemistry synthetic strategies. The example small organic and organic polymer materials are shown in Figure 1.1 and 1.2.

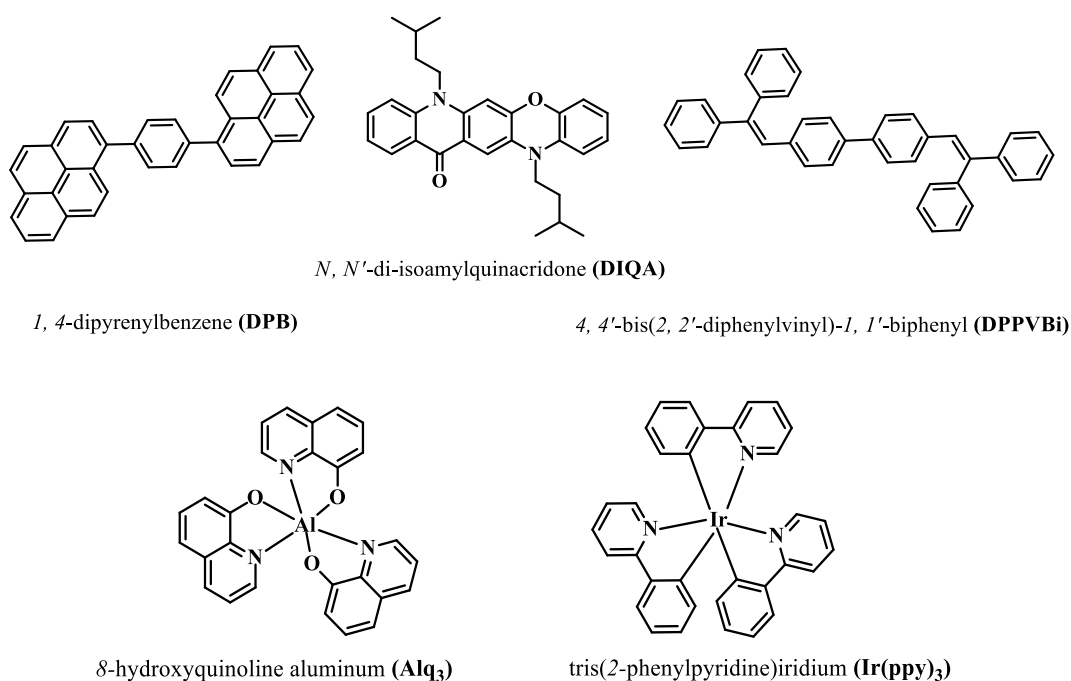


Figure 1.1 Examples of small organic molecules [1-3]

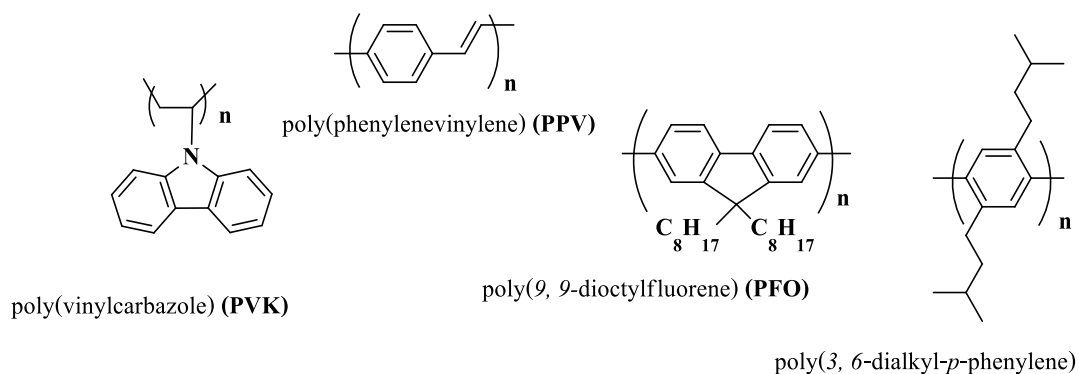


Figure 1.2 Examples of organic polymeric molecules [4-6]

The small organic molecules are characterized by a low molecular mass. The thin layer deposition is generally obtained by evaporation under vacuum. The first report of efficient devices using small molecule was created by Kodak [7] which gave moderately low bias voltage ($< 10\text{V}$) with attractive luminance efficiency. By comparison, polymers have long molecules and high molecular weights. Several forms may be encountered: homopolymers, copolymers and dendrimers. The optical and electrical properties of polymer materials depend on the monomer and periphery. In this thesis, we are interested in benzo[*d,e*]chromene and thioarene derivatives because they showed good characteristics e.g. solubility, thermal stability and environmental friendly. The flexibility and easy for forming a work piece can be possible. So, benzo[*d,e*]chromene and thioarene will be a futuristic new materials that would lead to the next generation of electronic and optical devices.

Until now, organic electronics present in modern technology of academic interest such as organic light emitting diodes (OLEDs) and organic field effect transistors (OFETs).

1.1 Organic light emitting diodes (OLEDs)

OLEDs are the new generation of full-colour flat panel displays [8]. This technology offers many advantages over traditional liquid crystal displays (LCDs) which are thinner, lighter, and more efficient. Moreover, OLEDs are extremely robust and they may be deposited on many substrates either rigid or flexible [9]. Today, they are used in sophisticated flat panel displays and a wide variety of information terminals such as mobile phones and television, which are shown in Figure 1.3.



Figure 1.3 Example of OLED displays [10-11]

1.1.1 OLED structure

In principle, a simple OLED structure can consist of an organic layer sandwiched between two electrodes as anode and cathode [12]. However, a multi-layer OLED were made of several different functional organic layers which are superior in terms of efficiency and lifetime. The multi-layer OLED structure is depicted in Figure 1.4. It comprises of an anode, hole transport layer (HTL), emission layer (EML) and electron transport layer (ETL). Frequently, the anode is made from a high work function material of indium tin oxide (ITO), which is transparent and good electrical conductivity. For the cathode, it was made from low work function metal such as calcium (Ca) or aluminum (Al) often used in combination with highly reflective and less reactive metals. While the emission layer composed of an organic dopant.

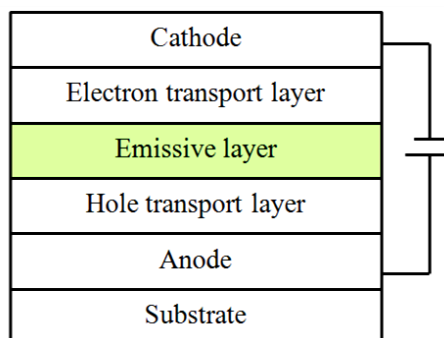


Figure 1.4 The multi-layer OLED structures

1.1.2 Working principle of OLED

The basic process of OLED, the external potential source is applied to the devices. The negative charges or electrons are generated from the cathode, while the positive charges or holes are generated from the anode. Both charges transfer towards via a hopping mechanism. After arriving at the emission layer, electrons and holes accumulate at the lowest unoccupied molecular orbital (LUMO) and highest occupied molecular orbital (HOMO) of emitting materials, respectively. The electron-hole pair formation occurs leading to an exciton generation. Exciton relaxation from the excited to the ground state results in the emission of light [13], which are shown in Figure 1.5.

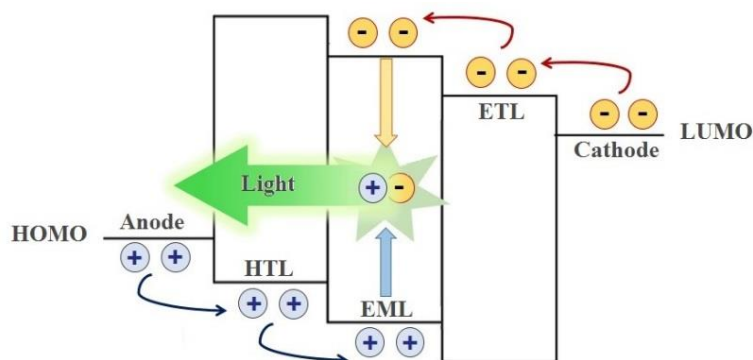


Figure 1.5 Schematic energy diagram of basic process in multi-layer OLED

The principle of the electronic processes in molecules can be schematically illustrated with the classical Jablonski diagram (Figure 1.6) which is basically an energy diagram, arranged with energy on a vertical axis. The first transition is the absorption of a photon with specific energy. This transition occurs from ground state (S_0) to excited state (S_1 and S_2). Once an electron is excited, the vibrational relaxation of excited state

to its lowest vibrational level. The next process of nonradiative transition is internal conversion (IC) which transition from a vibration level to another vibration level in a lower electronic state. The system relaxes to ground state by emitting fluorescence. Another emission process is phosphorescence which generated by intersystem crossing (ISC) ($S_1 \rightarrow T_1$) and eventually emitted the light [14].

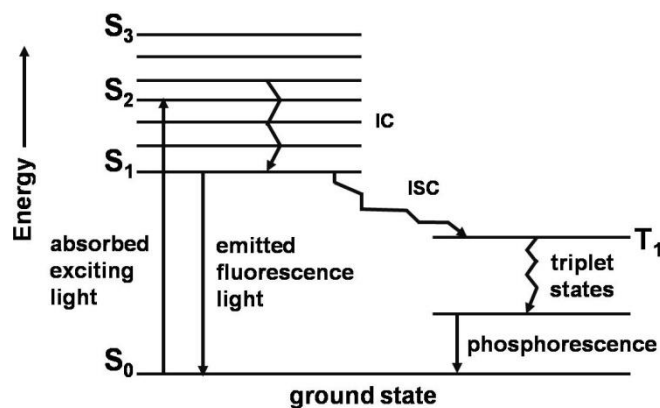


Figure 1.6 Jablonski energy diagram

1.1.3 Host-guest for OLED

When a host molecule is excited from the ground state by either absorbing light energy or being driven by electric energy. It can directly release its energy through radiative decay or nonradiative decay processes to the ground state. However, in the presence of a suitable guest molecule, energy transfer processes will occur. The latter event, it is depicted in the left side of the diagram as an energy transfer transition from the host molecule to the guest molecule by Förster, Dexter, or radiative energy transfer processes. At this point, the radiative decay processes will occur from the luminescent guest molecules. It may be noted that the emission spectrum observed is sometimes the emission from only the guest molecules due to complete energy transfer processes. The mechanism is illustrated in Figure 1.7.

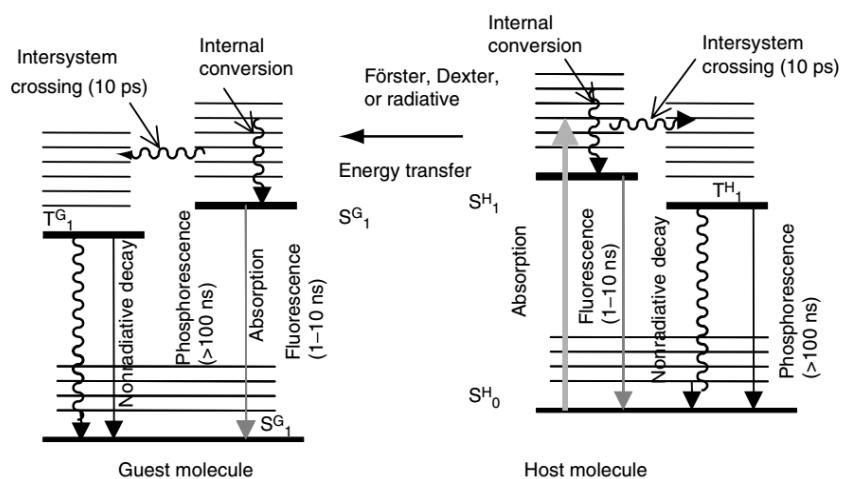


Figure 1.7 Electronic processes of host-guest molecules [15]

During host-guest operation, singlet and, in some cases, triplet excitations may first be created in the host material. Then through charge or energy transfer from the host to the guest, singlet or triplet excited states are formed in the guest. For an effective guest-host system, several factors must be considered, such as the phase compatibility of the host and guest, the aggregation of the molecules, and the host-guest energy level and orbital alignment. Thomas and coworkers studied efficient energy level in a host-guest system using computation methods [16]. They found that the charge transfer process, the band gap of the guest should fall within the band gap of the host favor transport of electrons and holes from the host to the guest, where they should then recombine. If such energy transfers processes dominate. Efficient energy transfer requires that the energy of the excited state of the host should be higher than that of the emissive excited state of the guest. This applies to both singlet excited states of the host and the guest as shown in Figure 1.8.

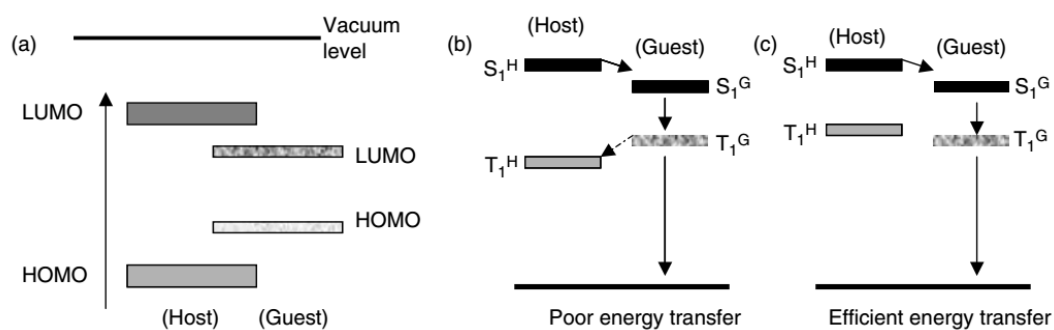


Figure 1.8 Energy level relationship in guest-host systems [17]

1.1.4 OLED parameter

In OLED technology the most important parameters to characterize the performance of OLED devices are describe in this section [18].

1.1.4.1 Luminance (L): the expression of amount of light emitted by the device was measured in candela per surface unit (cd/m^2).

1.1.4.2 Current density (J): the flux of current through the device was measured in ampere per surface unit (A/m^2).

1.1.4.3 Turn on voltage ($V_{\text{turn on}}$): the intersection between current density (J) and luminance (L) versus applied bias voltage (V), it is shown in Figure 1.9.

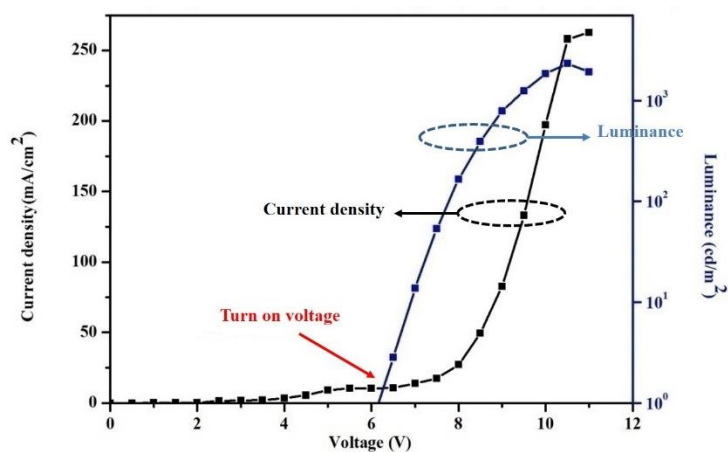


Figure 1.9 Luminance, current density and turn on voltage characteristic

1.1.4.4 Current efficiency (CE, η_L): emitted light per electric flux, expressed as candela per ampere (cd/A). This parameter is commonly used to measurement value for the luminous emission efficiency of an OLED where η_L is represented by below equation.

$$\eta_L = \frac{L}{J} \quad (1.1)$$

L : the luminance

J : the current density

1.1.4.5 Power efficiency (PE, η_P): the ratio of the optical flux to the electrical input, expressed as lumens per watt (Lm/W) where η_P is given by following equation.

$$\eta_P = \frac{\eta_L \pi}{V} \quad (1.2)$$

η_L : the current efficiency

V : the apply voltage

1.1.4.6 Commission internationale de l'éclairage (CIE) coordinates: the univocal definition of the emission color according to universally accepted international standards that can be calculated from the luminescence spectrum. This method originally recommended in 1931 by the CIE defines all metameric pairs by giving the amount an X , Y , Z of three imaginary primary colors required by a standard observer to match the color being specified (Figure 1.10).

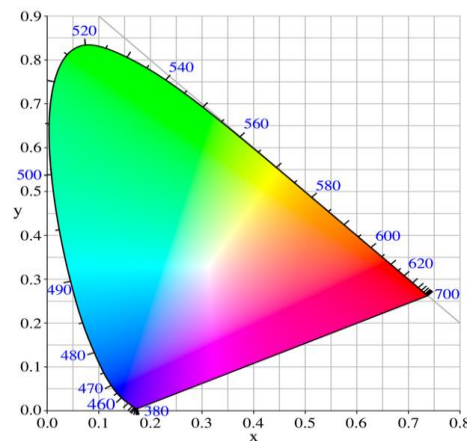


Figure 1.10 The CIE 1931 color space chromaticity diagram

1.2 Organic field effect transistors (OFETs)

The interest for OFET has drastically increased over the past few years, and they have been intensively studied for many applications such as displays, smart tags and sensors. The reason for focused research interest in the field of “plastic electronics” is the opportunity to produce low cost devices on plastic substrates on large areas, opening, indeed, an entire new market segment in the future which are shown in Figure 1.11.



Figure 1.11 Examples of OFET in the future [19-20]

1.2.1 OFET structure

OFETs are the basic building blocks for flexible integrated circuits and displays. To make OFET, materials ranging from conductors (source, drain and gate electrodes), semiconductors (organic materials), to insulators (gate dielectric layers) are needed shown in Figure 1.12. A wide range of organic molecules available in this section of the catalog are researched as potential high-performance p- and n-types organic semiconductors [21].

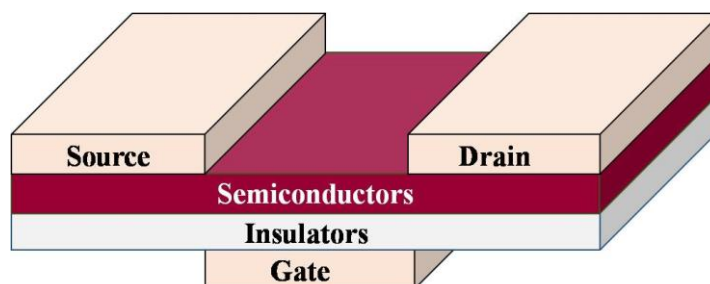


Figure 1.12 OFET device configuration of bottom-gate-top-contact

1.2.2 Working principle of OFET

An OFET consists of a semiconductor layer, an insulator layer, and three electrodes (source, drain and gate electrodes). The source and drain electrodes are connected to the semiconductor layer, whereas the gate electrode is electrically isolated from the semiconductor layer by gate dielectric in the insulator layer. Normally, voltage is applied to the gate electrode (V_G) and drain electrode (V_D) with respect to the source electrode, which is grounded ($V_S = 0$ V). The current between the source and drain electrodes (I_{DS}) depends on both the gate bias and drain bias. The different operating regimes can be identified [22], as shown in Figure 1.13.

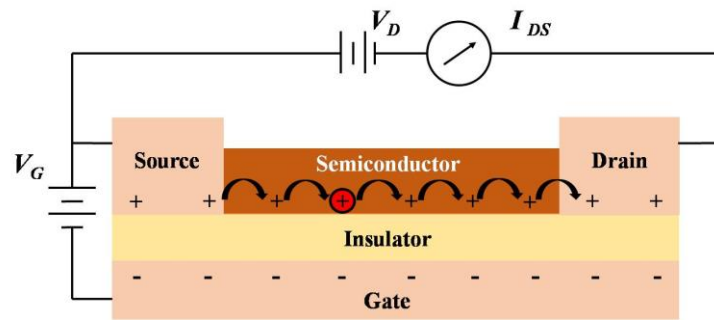


Figure 1.13 Schematic description of the principle of operation for OFET

1.2.3 OFET parameter

In OFET technology the most important parameters to characterize the performance of OFETs devices are describe in this section [23].

1.2.3.1 Mobility (μ): the relationship between the carrier speed in a material and the applied electric field, measured in unit of square centimeter par volt second (cm^2/Vs). The mobility was calculated from the saturation region with the following equation.

$$\mu = \frac{I_{DS}2L}{WC_i(V_G - V_T)^2} \quad (1.3)$$

Where I_{DS} is the drain-source current in unit of ampere or coulomb per second (A or C/s), W is the channel width in unit of micrometer (μm), L is the channel length in unit of micrometer (μm), C_i is the capacitance per unit area of the gate dielectric layer in unit of farad per square centimeter or coulomb per volt square centimeter (F/cm^2 or

$C/V\text{cm}^2$), and V_G and V_T are the gate voltage and threshold voltage in unit of volte (V), respectively.

1.2.3.2 Threshold voltage (V_T): the threshold voltage is to extrapolate the linear part of a $\sqrt{-I_{DS}}$ curve to the intercept on the V_{GS} axis which is a black line in Figure 1.14.

1.2.3.3 Transfer curve: the transfer characteristic relates drain-source current (I_{DS}) response to the input gate-source driving voltage (V_{GS}) which is a blue curve in Figure 1.14.

1.2.3.4 On/off current ratio (I_{on}/I_{off}): the characteristic of logic transistors. That is ratio of currents with $V_{GS} = \text{logic low}$ and $V_{GS} = \text{logic high}$ while $V_{DS} = \text{constant}$ and equal to maximum allowed voltage (Figure 1.14).

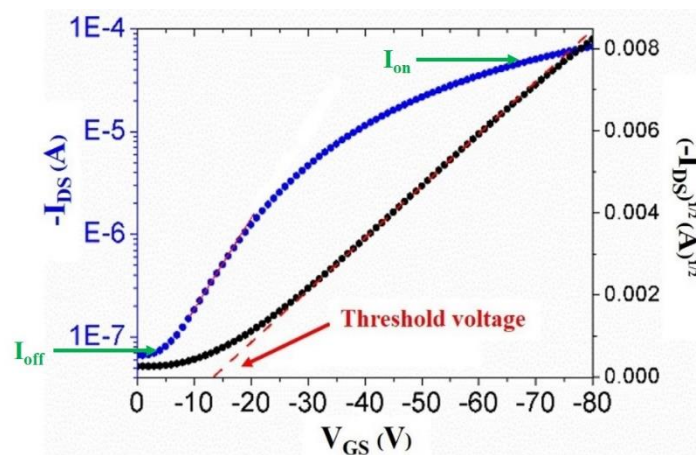


Figure 1.14 Threshold voltage, transfer curve and on/off current characteristics

1.2.3.5 Output curve: the output characteristic plot drain-source current (I_{DS}) versus drain-source voltage (V_{DS}) for several values of gate-source driving voltage (V_{GS}), in Figure 1.15.

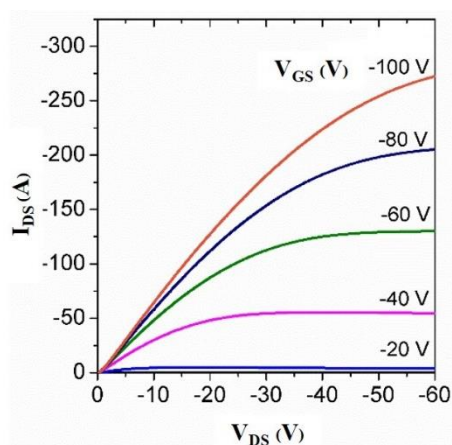
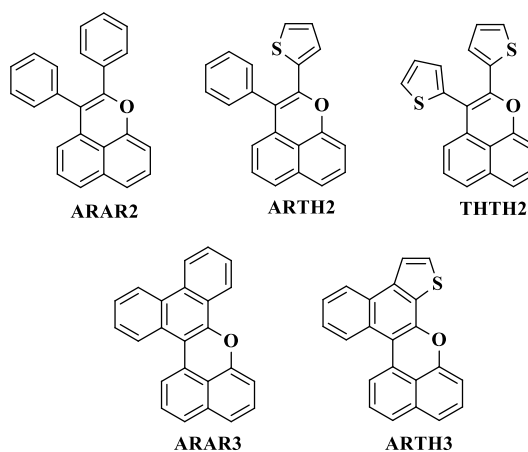


Figure 1.15 Output characteristic

1.3 Objectives of thesis

1.3.1 To synthesize and characterize a series of benzo[*d,e*]chromene (**ARAR2** and **ARAR3**) and thioarene (**ARTH2**, **ARTH3** and **THTH2**) derivatives



1.3.2 To study the photophysical, electrochemical and thermal properties of the target molecules

1.3.3 To study their OLED performances

1.3.4 To study their OFET performances

CHAPTER 2

LITERATURE REVIEW

The design and synthesis of a new organic compound for using in organic electronics was of interested because it showed potentially new applications in organic materials such as organic light emitting diodes (OLEDs) and organic field effect transistors (OFETs). In this thesis, we focused on the study of a new π -conjugated molecule of the benzo[*d,e*]chromene and thioarene derivatives.

Yan and co-worker [24] reported the synthesis of benzo[*d,e*]chromene derivatives by annulation reactions with diazo compound proceed efficiently in the presence of an iridium catalyst to give the product was obtained in moderate to good yields (Figure 2.1).

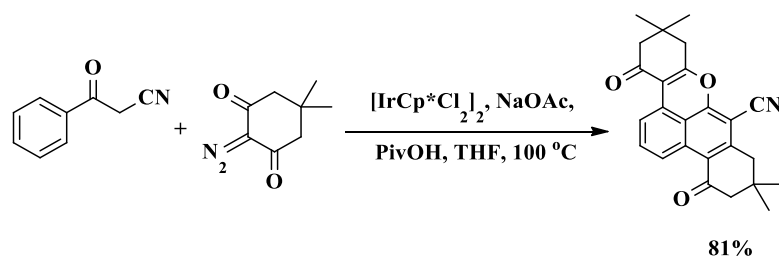


Figure 2.1 Benzo[*d,e*]chromene derivatives synthesis from iridium catalyst by Yan and co-worker

Wang and co-worker [25] reported the method for the synthesis of benzo[*d,e*]chromene derivatives from the electron-deficient naphthoquinones and alkynes via rhodium catalyzed which the reactions achieved in the good yield (Figure 2.2)

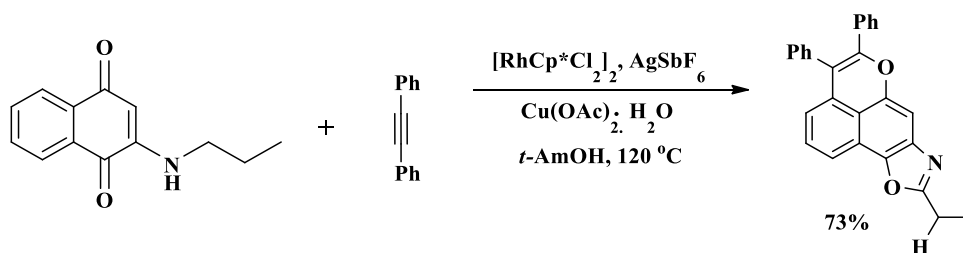


Figure 2.2 Benzo[*d,e*]chromene derivatives synthesis from rhodium catalyst by Wang and co-worker

Miura and co-worker [26] reported the synthesis of the weak chelation-assistance by using rhodium catalyzed in the annulation reactions of aromatic compounds with internal alkynes to give the benzo[*d,e*]chromene derivatives in moderate to good yields (Figure 2.3).

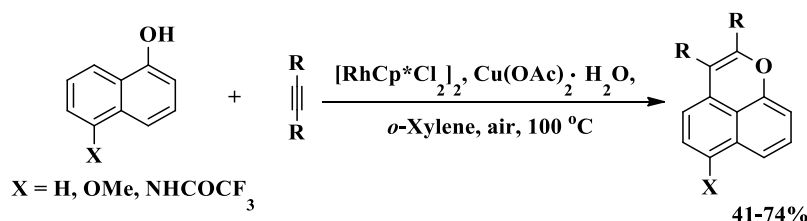


Figure 2.3 Benzo[*d,e*]chromene derivatives synthesis from rhodium catalyst by Miura and co-worker

Tan and co-worker [27] reported the synthesis of the oxidative annulation reactions of benzo[*d,e*]chromene derivatives with internal alkynes proceed efficiently in the presence of a rhodium catalyst and a copper oxidant to give the substrate with excellent yields (Figure 2.4).

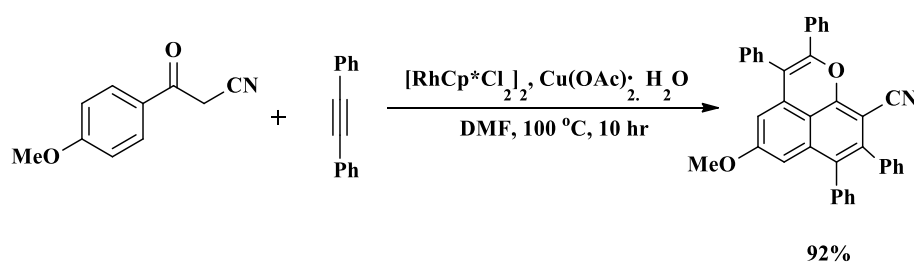


Figure 2.4 Benzo[*d,e*]chromene derivatives synthesis from rhodium catalyst by Tan and co-worker

Xie and co-worker [28] reported a novel synthetic route for the synthesis of benzo[*d,e*]chromene derivatives in Figure 2.5. The key step for synthesizing involved the rapid construction of oxaphenalene structure by a one-step reaction of ruthenium catalyzed to obtain the target compound with high yields.

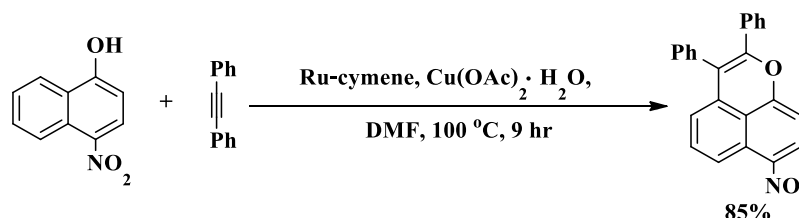


Figure 2.5 Benzo[*d,e*]chromene derivatives synthesis from ruthenium catalyst by Xie and co-worker

Thirunavukkarasu and co-worker [29] reported the synthesis of benzo[*d,e*]chromene derivatives by using ruthenium catalyzed oxidative C-H bond functionalization through hydroxyl assistance. Thus, a ruthenium catalyst used for the annulation reactions of varied symmetry alkynes with naphthols to give the products in moderate to good yields (Figure 2.6).

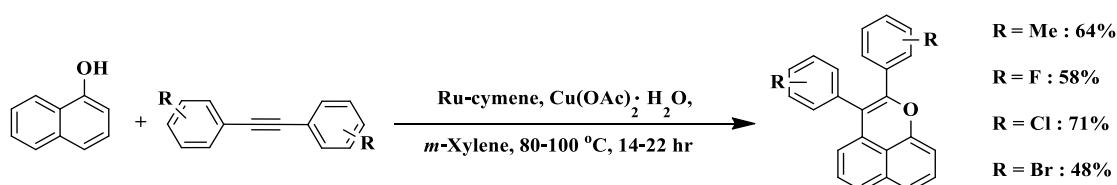


Figure 2.6 Benzo[*d,e*]chromene derivatives synthesis from ruthenium catalyst by Thirunavukkarasu and co-worker

Mochida and co-worker [30] reported the synthesis and characterization of benzo[*d,e*]chromene derivatives which achieved by the rhodium catalyzed oxidative coupling of naphthols or phenolic and alcoholic substrates with alkynes. All products showed the emission wavelength in the range of 480-580 nm (Figure 2.7).

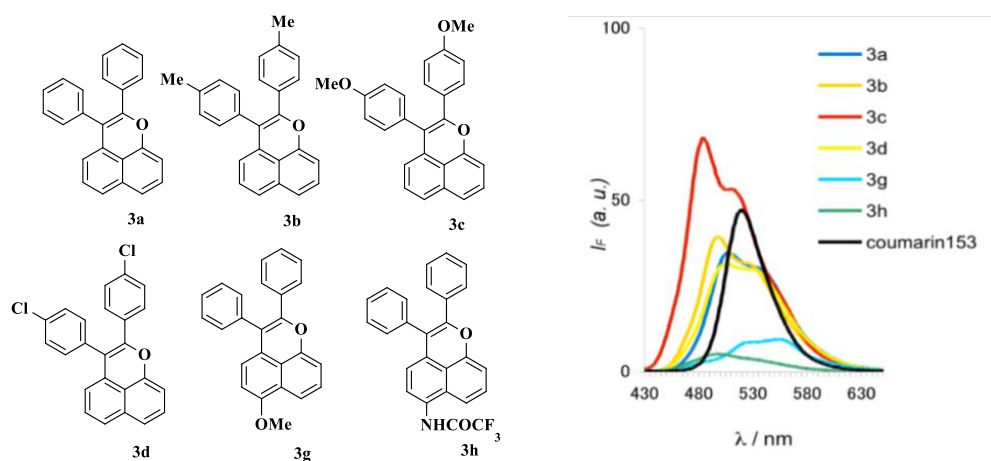


Figure 2.7 The structures and emission spectra of benzo[*d,e*]chromene derivatives by Mochida and co-worker

Recently, our group by Miss Benjawan Somchob [31] reported the synthesis and characterization of benzo[*d,e*]chromene derivatives (**BS01-BS04**) which were designed based on fluorophenyl acceptor (Figure 2.8). Moreover, **BS01-BS04** compounds were studied in OLEDs. The OLEDs device of **BS02** exhibited a green color with the maximum current and power efficiencies at 1.28 cd/A and 0.47 Lm/W, respectively.

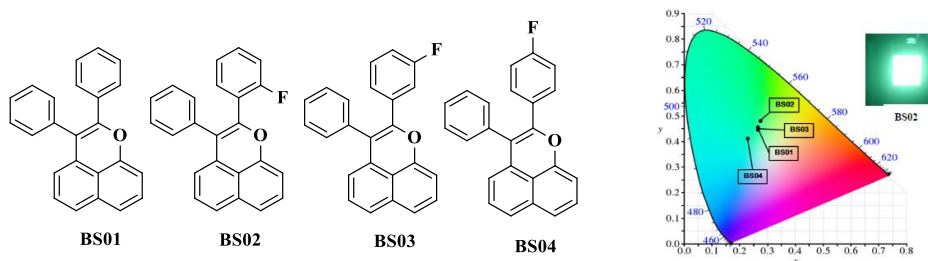


Figure 2.8 Benzo[*d,e*]chromene derivatives for OLEDs device by Miss Benjawan Somchob and co-worker

Scholl reaction or oxidative dehydrogenative cyclization used for the construction of new carbon-carbon bonds to fuse π -conjugated systems has been witnessed as a useful chemical strategy for the synthesis of novel fluorophore [32]. Badger and co-worker [33] reported the synthesis of the rigid thioarene derivatives from 2, 3, 4, 5-tetraphenylthiophene (**41**) when it was subjected to classical Scholl conditions with

aluminium chloride (AlCl_3) as an oxidative coupling catalyst to give the flavophen (**42**) in 26% yield (Figure 2.9).

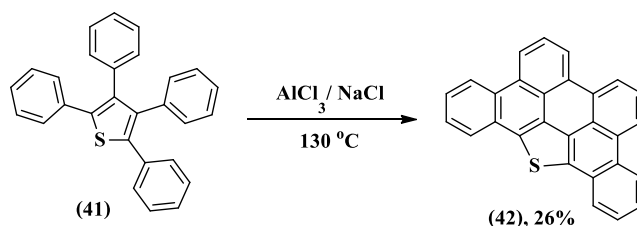


Figure 2.9 Thioarene derivatives synthesis from AlCl_3 catalyst by Badger and co-worker

Larsen and co-worker [34] reported the synthesis of the rigid thioarene derivatives by using an oxidative coupling with ferric chloride (FeCl_3) for the preparation of thiaheterohelicenes. In a model study, it was shown that bis(3-thienyl)-substituted catechol diether (**132**) cyclized upon treatment with FeCl_3 (4 eq.) gave naphtho[2, 1-*b*: 3, 4-*b'*]-dithiophene (**133**) in 93% yield (Figure 2.10).

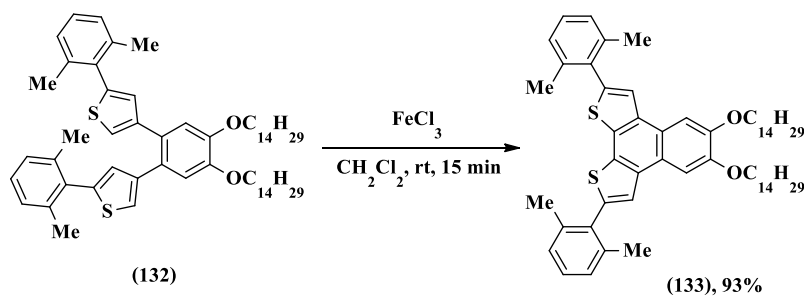


Figure 2.10 Thioarene derivatives synthesis from FeCl_3 catalyst by Larsen and co-worker

Jian and co-worker [35] reported the synthesis of the rigid thioarene derivatives (**1a-b**) by using FeCl_3 as an oxidative coupling reagent via the intramolecular Scholl reaction to obtain a good yields (Figure 2.11).

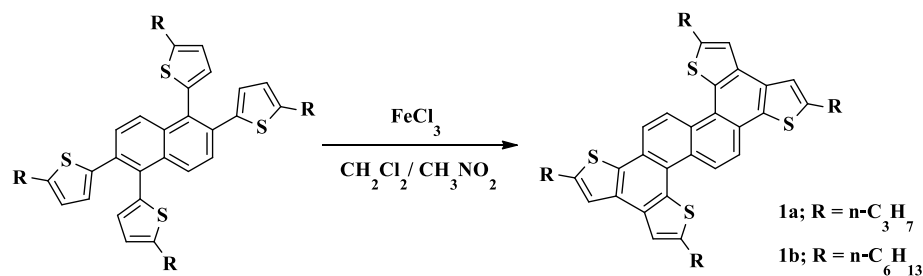


Figure 2.11 Thioarene derivatives synthesis from FeCl₃ catalyst by Jian and co-worker

Daniel and co-worker [36] reported the synthesis of thioarene derivatives with electron-donating and electron-withdrawing substituent in different positions. They found that 7, 9-dihydroxy-thieno[2, 3-*c*]coumarin gave a high fluorescence quantum yield at 36% (Figure 2.12).

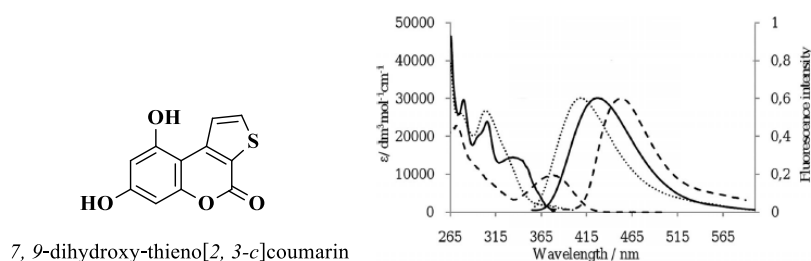


Figure 2.12 The structure and photophysical property of thioarene derivatives by Daniel and co-worker

Lui and co-worker [37] reported the synthesis of thioarene derivatives (**65**) with thienyl in the 1-, 3-, 6- and 8-positions of pyrene cores (Figure 2.13). Then they studied the OFET device by using (**65**) as the active material exhibited p-type performance which was observed the mobility up to 0.0037cm²/Vs with an on/off ratio of 10⁴, and the threshold voltage at -21 V.

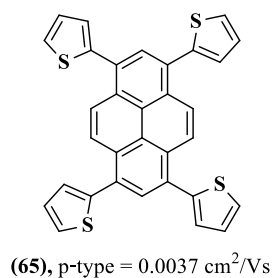


Figure 2.13 Thioarene derivatives for OFETs device by Lui and co-worker

Katz and co-workers [38] reported the synthesis of thioarene derivatives with terminally alkyl substituted anthradithiophenes (Figure 2.14) for OFETs performance. The OFET charge-carrier mobilities were obtained 0.01-0.02 cm²/Vs for the dihexylanthradithiophene.

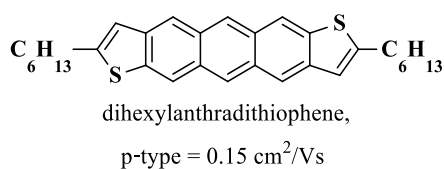


Figure 2.14 Thioarene derivatives for OFETs device by Katz and co-workers

Yanming and co-worker [39] developed the thioarene derivatives (Figure 2.15) constitute for used materials in OFETs. The result showed that the thiophene-benzene (**5d**) exhibited mobilities up to 0.42 cm²/Vs and on/off current ratios up to 5x10⁶.

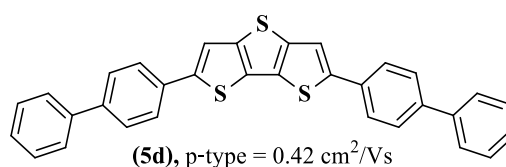
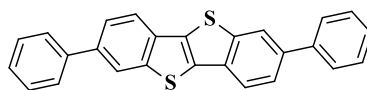


Figure 2.15 Thioarene derivatives for OFETs device by Yanming and co-worker

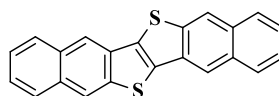
Takimiya and co-worker [40] developed the thioarene derivatives for organic semiconductors based on fused chalcogenophene compounds. The 2, 7-diphenyl[1]benzothieno[3, 2-*b*]-[1]benzothiophene (**DPh-BTBT**, Figure 2.16) demonstrated OFETs performance in air-stable. The OFETs device exhibited a high mobility at 2.0 cm²/Vs.



DPh-BTBT, p-type = $2.0 \text{ cm}^2/\text{Vs}$

Figure 2.16 Thioarene derivatives for OFETs device by Takimiya and co-worker

Yamamoto and co-worker [41] developed the thioarene derivatives with a highly π -extended heteroarenes which the dinaphtho-[2, 3-*b*: 2', 3'-*f*]chalcogenopheno[3, 2-*b*]chalcogenophene (**DNTT**, Figure 2.17) gave a promising characteristic of organic semiconductors. The excellent OFET characteristics with a higher than $2.0 \text{ cm}^2/\text{Vs}$ and $I_{\text{on}}/I_{\text{off}}$ of 10^7 were observed.



DNTT, p-type $> 2.0 \text{ cm}^2/\text{Vs}$

Figure 2.17 Thioarene derivatives for OFETs device by Yamamoto and co-worker

CHAPTER 3

EXPERIMENT

This chapter explain the synthesis and characterization of benzo[*d,e*]chromene and thioarene derivatives which will be used as organic electronics emitting material. The preparation, characterization and fabrication for OLEDs and OFETs are described.

3.1 Chemicals

All chemicals and solvents were purchased and used without further purification unless otherwise noted. The chemicals for the synthesis, OLEDs and OFETs performances used in this work are shown in the following table (Table 3.1, 3.2 and 3.3 for synthesis, OLEDs and OFETs performances study, respectively).

Table 3.1 Chemicals for the synthesis

Chemicals	Formula	Grade	Manufacturer
Acetone	C ₃ H ₆ O	Commercial	CARLO ERBA
Acetonitrile	CH ₃ CN	99.8%	CARLO ERBA
Chloroform- <i>d</i>	CDCl ₃	99.8%	CARLO ERBA
Copper (II) acetate hydrate	Cu(OAc) ₂ •H ₂ O	99%	ACROS
Copper (I) iodide	CuI	99%	ACROS
Dichloromethane	CH ₂ Cl ₂	99.8%	ACROS
Dichloro(<i>p</i> -cymene)ruthenium (II) dimer (Ru-cymene)	C ₂₀ H ₂₈ Cl ₄ Ru ₂	Synthesis	[42]
Ethyl acetate	C ₄ H ₈ O ₂	Commercial	CARLO ERBA
Ferric chloride anhydrous	FeCl ₃	≥ 99%	ALDRICH
Ferrocene	C ₁₀ H ₁₀ Fe	> 98%	ACROS
Hexane	C ₆ H ₁₄	Commercial	CARLO ERBA

Table 3.1 Chemicals for the synthesis (continued)

Chemicals	Formula	Grade	Manufacturer
Iodobenzene	C ₆ H ₅ I	98%	ACROS
2-Iodothiophene	C ₄ H ₃ IS	99%	TCI
Methanol	CH ₃ OH	Commercial	CARLO ERBA
Phenylacetylene	C ₈ H ₆	98%	ACROS
Silver carbonate	Ag ₂ CO ₃	99%	ACROS
Sodium sulphate anhydrous	Na ₂ SO ₄	≥ 99%	CARLO ERBA
Tetrabutylammonium chloride	C ₁₆ H ₃₆ ClN	99%	ACROS
Tetra- <i>n</i> -butylammoniumhexa Fluorophosphates	(Bu ₄ N)PF ₆	98%	ACROS
Tetrahydrofuran	C ₄ H ₈ O	99.8%	CARLO ERBA
Tetrakis(triphenylphosphine) palladium (0)	Pd(PPh ₃) ₄	Synthesis	[43]
Triethylamine	C ₆ H ₁₅ N	99%	ALDAICH
Trimethylsilylacetylene	C ₅ H ₁₀ Si	99%	ACROS

Table 3.2 Chemicals for OLEDs performance study

Materials	Grade	Manufacturer
Acetone	99.8%	RCI LABSCAN
Aluminium (Al)	99%	ACROS
4, 7-Diphenyl-1, 10-phenanthroline (Bphen)	> 99.5%	LÜM-TEC
Ethanol	99.8%	RCI LABSCAN
Indium-doped tin oxide (ITO) glass	99.5%	LÜM-TEC
Lithium fluoride (LiF)	99.9%	ALDRICH
2-Methyl-9, 10-bis(naphthalen-2-yl) anthracene (MADN)	> 99.5%	LÜM-TEC
(<i>N</i> , <i>N'</i> -diphenyl)- <i>N</i> , <i>N'</i> -bis(1-naphthyl)-1, 1'-biphenyl-4, 4'-diamine (NPB)	> 99.5%	LÜM-TEC
2-Propanol	99.8%	RCI LABSCAN

Table 3.3 Chemicals for OFETs performance study

Materials	Grade	Manufacturer
Gold (Au)	99.9%	ACROS
Hellmanex III	99%	ALDAICH
Octadecyltrichlorosilane (OTS)	97%	ACROS
2-Propanol	99.8%	RCI LABSCAN
Silicon wafer (Si/SiO ₂) substrate	Prime	UNIVERSITY WAFER
Toluene	99.9%	ALDAICH

3.2 Instruments

Instruments used in this thesis are shown in the following table for the molecular characterization, OLEDs and OFETs measurements.

Table 3.4 Instruments for the molecular characterization

Instruments	Company	Model
Nuclear magnetic resonance spectrometer (NMR)	Brüker	AVANCE
Fourier-transform infrared spectrometer (FT-IR)	Perkin-Elmer	Spectrum TWO
Mass spectrometer (MS)	Brüker	MicroTOF-Q II
UV-Visible spectrophotometer	Perkin Elmer	Lamda25
Fluorescence spectrophotometer	Perkin Elmer	LS55
Lifetime (τ)	Fluoromax-4	HORIBA
Quanta- ϕ integrating sphere spectrofluorometer	F-3029	HORIBA
Cyclic voltammetry (CV)	Metrohm	PG11
Thermogravimetric analysis (TGA)	Rigaku Japan	TG8120 Thermoplus
Melting point (m.p.)	Büchi	530

Table 3.5 Instruments for OLED study

Instruments	Company	Model
Vacuum oven	BINDER	VD23
Ultrasonic cleaner	CREST	-
UV ozone cleaner	JELIGHT	42-220
Thermal evaporator	EDWARDS	AUTO306
Vacuum coating organic deposition	Kurt J. Lesker	SPECTROS 150
Luminance detector	MINOLTA	LS-110
Power supply and multimeter	KEITHLEY	2420

Table 3.6 Instruments for OFET study

Instruments	Company	Model
Vacuum oven	BINDER	VD23
Ultrasonic cleaner	CREST	-
UV ozone cleaner	JELIGHT	42-220
Thermal evaporator	EDWARDS	AUTO306
Vacuum coating organic deposition	Kurt J. Lesker	SPECTROS 150
Semiconductor characterization system	KEITHLEY	4200 SCS

3.2.1 Structural characterization techniques

The structural of the target products were characterized by ^1H , ^{13}C NMR, FT-IR and mass spectroscopy techniques, respectively. The optical properties, lifetime and quantum yield were characterized by UV-Visible absorption and fluorescence spectroscopy, respectively. Whereas the electrochemical property was characterized by cyclic voltammetry. Finally, the thermal properties were characterized by melting point and thermogravimetric analysis, respectively.

3.2.1.1 Nuclear magnetic resonance spectroscopy (NMR)

^1H NMR (300 MHz), ^{13}C NMR (75 MHz) and 2D NMR (COSY and HMBC) were recorded on Brüker AVANCE spectrometer. TMS was used as the internal reference (0.00 ppm) where the samples were dissolved in CDCl_3 . Data for NMR spectra are reported as followed: the chemical shifts (δ), reported relative to the

residual solvent peak in part per million (ppm), and the coupling constants (J) given in hertz (Hz). The multiplicities are quoted as singlet (s), broad (br), doublet (d), triplet (t), and multiplet (m), respectively.

3.2.1.2 Fourier-transform infrared spectroscopy (FT-IR)

FT-IR spectra were characterized by using Perkin-Elmer FT-IR spectroscopy. Spectra were recorded from 4000-400 wavenumber (cm^{-1}).

3.2.1.3 Mass spectroscopy (MS)

Molecular weights were measured on Brüker MicroTOF- Q II by electrospray ionization techniques.

3.2.1.4 Photophysical properties

UV-visible spectra were studied in a 1 cm path length quartz cell on a Perkin-Elmer UV Lamda25 spectrometer at room temperature. The 2×10^{-6} M sample solutions were dissolved in spectroscopic toluene. The fluorescence spectra of 2×10^{-7} M sample solutions in spectroscopic toluene were measured in a 1 cm path length quartz cell on Perkin-Elmer LS55 luminescence spectrometer. Moreover, the decay times were performed on HORIBA Fluoromax-4 spectrofluorometer NANOLED 370 nm by using 0.001 M LUDOX as standard prompted solution. The sample solutions were dissolved in spectroscopic toluene. In addition, the photoluminescence quantum yields were measured with quanta- ϕ model HORIBA F-3029 from integrating sphere in the dark.

3.2.1.5 Cyclic voltammetry (CV)

Cyclic voltammograms were reported by using an Autolab Metrohm PG11. The solutions were prepared at a concentration of 1×10^{-3} M in acetonitrile containing 0.1 M $(\text{Bu}_4\text{N})\text{PF}_6$ as supporting electrolyte and purged with argon gas prior to use at a scan rate of 50 mV/s at room temperature.

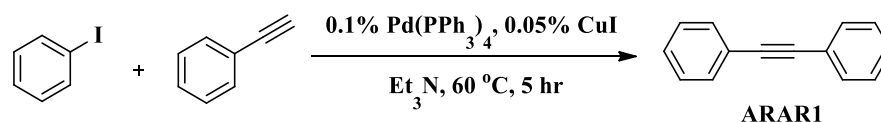
3.2.1.6 Thermal properties

Melting points were obtained on Büchi 530 scientific melting point apparatus in open capillary method and are uncorrected and reported in degree Celsius ($^{\circ}\text{C}$). The thermal gravimetical analysis (TGA) was carried out on a Rigaku Japan TG8120 Thermoplus instrument with $10^{\circ}\text{C}/\text{min}$ heating rate under nitrogen atmosphere at 25-800 $^{\circ}\text{C}$.

3.3 Synthesis

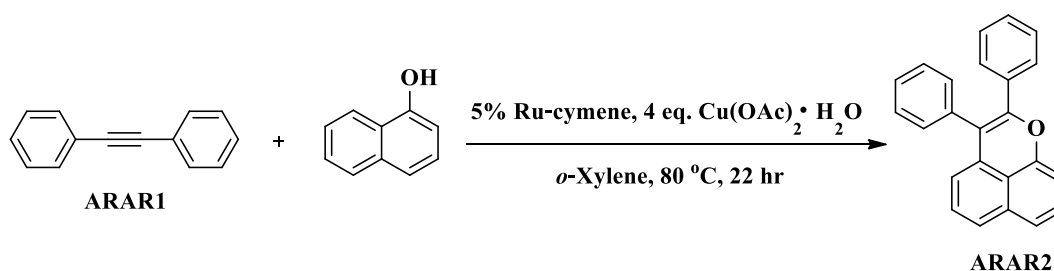
3.3.1 2, 3-Diphenylbenzo[*d,e*]chromene (ARAR2)

3.3.1.1 1, 2-Diphenylethylene (ARAR1)



The mixture of iodobenzene (3.00 mL, 26.80 mmol), Pd(PPh₃)₄ catalyst (31 mg, 26.8 μmol), phenylacetylene (3.10 mL, 28.23 mmol), CuI (2.55 mg, 13.4 μmol) and NEt₃ (200 mL) were placed in a 500 mL round bottom flask. The mixture reaction was flowed with nitrogen gas several times with nitrogen balloon and then refluxed under nitrogen balloon at 60 °C overnight. After that, the reaction mixture was cooled to room temperature. Crude reaction was extracted with hexane and water. Then it was purified by column chromatography using hexane as a mobile phase to obtain the pure product as a white crystal (0.4281 g, 98 % yield); m.p. 54-55 °C; ¹H NMR (300 MHz, CDCl₃) δ 7.54 (d, *J* = 7.4 Hz, 4H), 7.36-7.34 (m, 6H) ppm; HRMS calcd for C₁₄H₁₁ (M+H⁺): 179.0861, found: 179.0861.

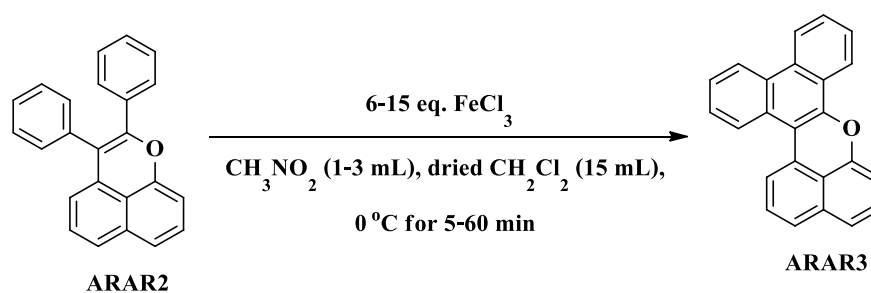
3.3.1.2 2, 3-Diphenylbenzo[*d,e*]chromene (ARAR2)



The mixture of **ARAR1** (500 mg, 2.80 mmol), 1-naphthol (807 mg, 5.60 mmol), **Ru-cymene** catalyst (86 mg, 0.14 mmol), Cu(OAc)₂•H₂O (6.36 g, 11.20 mmol) and *o*-Xylene (20 mL) were placed in a 50 mL round bottom flask. The mixture reaction was flowed with nitrogen balloon several times and then refluxed at 80 °C overnight. After that, the reaction mixture was cooled to room temperature. Crude reaction was extracted with ethyl acetate and water. Then it was purified by column chromatography using hexane as a mobile phase to obtain the yellow solid product

(0.3277 g, 73 %yield); m.p. 134-138 °C; ^1H NMR (300 MHz, CDCl_3) δ 7.38-7.12 (m, 14H), 6.87 (d, $J = 7.0$ Hz, 1H), 6.45 (d, $J = 7.1$ Hz, 1H) ppm; ^{13}C NMR (75 MHz, CDCl_3) δ 152.7, 149.4, 135.5, 134.8, 134.2, 131.9, 130.9, 129.0, 128.9, 128.3, 127.6, 127.5, 127.4, 123.6, 122.9, 119.1, 117.5, 115.6, 106.9 ppm; HRMS calcd for $\text{C}_{24}\text{H}_{17}\text{O}$ ($\text{M}+\text{H}^+$): 321.1279, found: 321.1279; FTIR: 3047, 1638, 1580, 1365, 1248, 810, 683 cm^{-1} .

3.3.2 Tribenzo[*a,c,k,l*]xanthene (ARAR3)



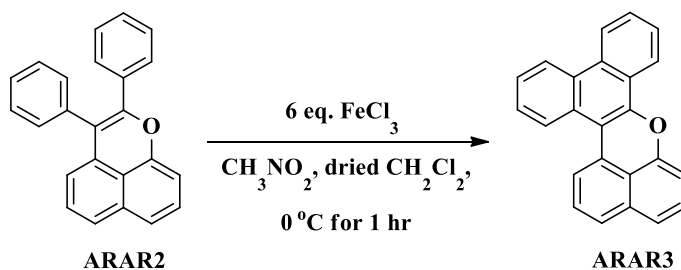
The intramolecular Scholl reaction of **ARAR2** was studied to obtain tribenzo[*a,c,k,l*]xanthenes (**ARAR3**) based on the literatures [44-45]. The mixture of **ARAR2** (0.94 mmol, 1 eq.) in dried CH_2Cl_2 (15 mL) at 0 °C and then anhydrous FeCl_3 (6-15 eq.) in CH_3NO_2 (1-3 mL) was added in a 100 mL three neck round bottom flask which was stirred under nitrogen balloon for 5-60 minutes. After that, the reaction was quenched by methanol and water, respectively. Crude reaction was extracted with dichloromethane and water. Then the organic portion was purified by column chromatography using dried hexane as a mobile phase. The studies are summarized in Table 3.7.

Table 3.7 The optimization of intramolecular Scholl reaction*

Entry	eq. of FeCl ₃	Time (min)	%Separated yield (ARAR3)
1[44]	15	5	6
2		30	11
3		60	18
4[45]	12	5	12
5		30	26
6		60	33
7	10	5	11
8		30	30
9		60	38
10	6	5	18
11		30	44
12		60	75

*The intramolecular Scholl reaction of **ARAR2** was studied with a varied equivalent of FeCl₃. The results found that the entry 12 with 6 equivalents of FeCl₃ after 60 minutes showed a high yield at 75%.

3.3.2.1 Tribenzo[*a,c,k,l*]xanthene (**ARAR3**)

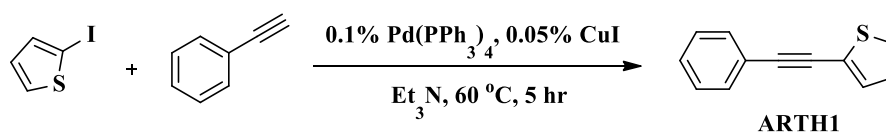


The mixture of **ARAR2** (300 mg, 0.94 mmol) in 15 mL dried CH₂Cl₂ at 0 °C was added by a solution of FeCl₃ (752 mg, 5.64 mmol) in CH₃NO₂ (3 mL). The mixture was stirred in a 100 mL three neck round bottom flask under nitrogen balloon for 1 hour. After that, the reaction was quenched by the addition of methanol (20 mL) and water (20 mL), respectively. Crude reaction was extracted with dichloromethane and water. Then the organic portion was purified by column chromatography using dried

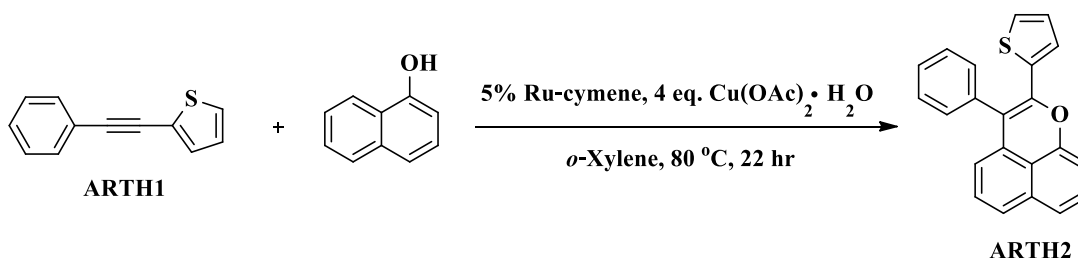
hexane as a mobile phase to obtain the yellow solid product (0.2236 g, 75 % yield); m.p. 162-164 °C; ^1H NMR (400 MHz, CDCl_3) δ 7.54 (d, $J = 7.4$ Hz, 1H), 7.38 (t, $J = 7.3$ Hz, 1H), 7.32-7.09 (m, 10H), 6.90 (d, $J = 7.7$ Hz, 1H), 6.31 (d, $J = 7.8$ Hz, 1H) ppm; ^{13}C NMR (75 MHz, CDCl_3) δ 152.6, 149.5, 135.2, 133.9, 131.9, 131.2, 130.9, 129.2, 128.9, 128.6, 128.5, 127.8, 127.7, 127.2, 123.6, 117.3, 116.2, 115.6, 108.2 ppm; HRMS calcd for $\text{C}_{24}\text{H}_{14}\text{NaO}$ ($\text{M}+\text{Na}^+$): 341.0942, found: 341.0944; FTIR: 3054, 1636, 1579, 1306, 1251, 828, 695 cm^{-1} .

3.3.3 2-Phenyl-3-(thiophen-2-yl)benzo[*d,e*]chromene (ARTH2)

3.3.3.1 2-(Phenylethynyl)thiophene (ARTH1)

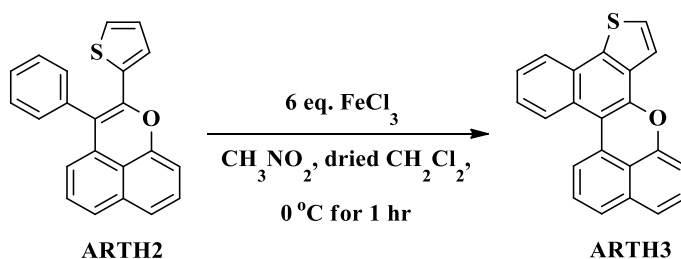


The mixture of 2-iodothiophene (2.0 mL, 18 mmol), $\text{Pd}(\text{PPh}_3)_4$ catalyst (21 mg, 18 μmol), phenylacetylene (2.4 mL, 22 mmol), CuI (1.70 mg, 9 μmol) and NEt_3 (25 mL) were placed in a 50 mL round bottom flask. The mixture reaction was flowed with nitrogen gas several times with nitrogen balloon and then refluxed under nitrogen atmosphere at 60 °C overnight. After that, the reaction mixture was cooled to room temperature. Crude reaction was extracted with hexane and water. Then it was purified by column chromatography using hexane as a mobile phase to obtain the pure product as a pale yellow solid (3.0367 g, 91 % yield); m.p. 49-50 °C; ^1H NMR (300 MHz, CDCl_3) δ 7.63 (dd, $J = 6.0, 2.6$ Hz, 2H), 7.44-7.34 (m, 5H), 7.09 (t, $J = 7.0$ Hz, 1H) ppm; HRMS calcd for $\text{C}_{12}\text{H}_9\text{S}$ ($\text{M}+\text{H}^+$); 185.0425 found; 185.0391.

3.3.3.2 2-Phenyl-3-(thiophen-2-yl)benzo[*d,e*]chromene (**ARTH2**)

The mixture of **ARTH1** (500 mg, 2.70 mmol), *l*-naphthol (778 mg, 5.40 mmol), **Ru-cymene** catalyst (81 mg, 0.13 mmol), $\text{Cu(OAc)}_2 \cdot \text{H}_2\text{O}$ (6.13 g, 10.80 mmol) and *o*-Xylene (20 mL) were placed in a 50 mL round bottom flask. The mixture reaction was flowed with nitrogen balloon several times and then refluxed at 80 °C overnight. After that, the reaction mixture was cooled to room temperature. Crude reaction was extracted with ethyl acetate and water. Then it was purified by column chromatography using hexane as a mobile phase to obtain the yellow solid product (0.5048 g, 57 % yield); m.p. 136-140 °C; $^1\text{H NMR}$ (300 MHz, CDCl_3) δ 7.61-7.53 (m, 3H), 7.40-7.31 (m, 5H), 7.22-7.15 (m, 2H), 6.97-6.88 (m, 3H), 6.27 (d, $J = 8.6$ Hz, 1H) ppm; $^{13}\text{C NMR}$ (75 MHz, CDCl_3) δ 151.7, 143.6, 136.1, 134.7, 134.1, 131.7, 130.5, 129.4, 127.9, 127.2, 127.1, 126.9, 126.8, 126.1, 123.1, 121.9, 118.8, 115.7, 115.6, 106.5 ppm; HRMS calcd for $\text{C}_{22}\text{H}_{15}\text{OS}$ ($\text{M}+\text{H}^+$): 327.0844, found: 327.0844; FTIR: 3059, 1637, 1585, 1492, 1252, 817, 765, 684 cm^{-1} .

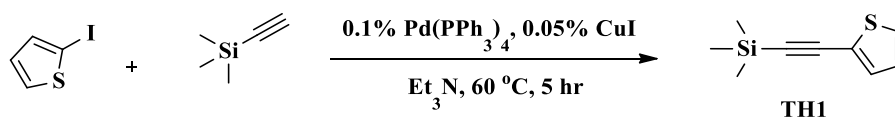
3.3.4 Dihydrodibenzo[*c,k,l*]thieno[2, 3-*a*]xanthene (ARTH3)



The mixture of **ARTH2** (300 mg, 0.92 mmol) in 15 mL of dried CH_2Cl_2 at 0 °C was added by a solution of FeCl_3 (736 mg, 5.52 mmol) in CH_3NO_2 (3 mL). The mixture was stirred in a 100 mL three neck round bottom flask under nitrogen balloon for 1 hour. After that, the reaction was quenched by the addition of methanol and water, respectively. Crude reaction was extracted with dichloromethane and water. Then the organic portion was purified by column chromatography using dried hexane as a mobile phase to obtain the yellow solid product (0.0954 g, 32 % yield); m.p. 170-172 °C; ^1H NMR (400 MHz, CDCl_3) δ 7.55 (t, $J = 8.0$ Hz, 3H), 7.46-7.12 (m, 5H), 6.92 (d, $J = 6.3$ Hz, 3H), 6.27 (d, $J = 7.1$ Hz, 1H) ppm; ^{13}C NMR (75 MHz, CDCl_3) δ 151.4, 145.9, 135.4, 135.0, 134.0, 131.9, 129.2, 127.9, 127.8, 127.6, 127.5, 127.4, 126.9, 126.3, 126.2, 123.3, 121.6, 119.2, 115.6, 108.1, 106.7 ppm; HRMS calcd for $\text{C}_{24}\text{H}_{12}\text{NaOS}$ ($\text{M}+\text{Na}^+$): 347.0507, found: 347.0507; FTIR: 3047, 1637, 1591, 1492, 1247, 840, 753, 696 cm^{-1} .

3.3.5 2, 3-Di(thiophen-2-yl)benzo[*d,e*]chromene (THTH2)

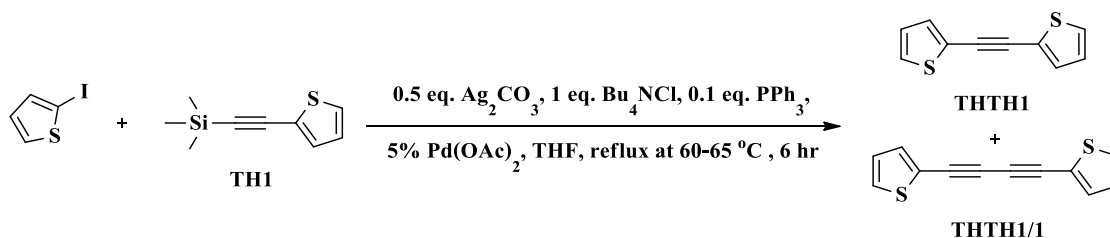
3.3.5.1 Trimethyl(2-thienylethynyl)silanen (TH1)



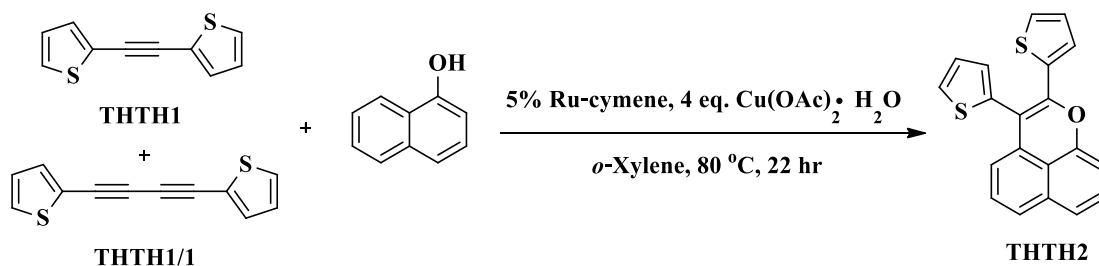
The mixture of 2-iodothiophene (2.0 mL, 18 mmol), $\text{Pd}(\text{PPh}_3)_4$ catalyst (21 mg, 18 μmol), trimethylsilylacetylene (2.4 mL, 17 mmol), CuI (1.70 mg, 9 μmol) and NEt_3 (25 mL) were placed in a 50 mL round bottom flask. The mixture reaction was flowed with nitrogen gas several times with nitrogen balloon and then refluxed under nitrogen atmosphere at 60 °C overnight. After that, the reaction mixture was cooled to room temperature. Crude reaction was extracted with hexane and water. Then it was purified by column chromatography using hexane as a mobile phase to

obtain the pure product as a yellow liquid (2.8736 g, 88 % yield); ^1H NMR (300 MHz, CDCl_3) δ 7.25 (d, $J = 5.4$ Hz, 2H), 6.98 (dd, $J = 5.0$ Hz, 3.8 Hz, 1H), 0.28 (s, 9H) ppm; HRMS calcd for $\text{C}_9\text{H}_{13}\text{SSi}$ ($\text{M}+\text{H}^+$): 181.0507, found: 181.0501.

3.3.5.2 1, 2-Di(thiophen-2-yl)ethyne (**THTH1**)



The mixture of **TH1** (500 mg, 2.77 mmol), 2-iodothiophene (17 mg, 3.60 mmol), Ag_2CO_3 (382 mg, 1.39 mmol), Bu_4NCl (770 mg, 2.77 mmol) and THF (2 mL) were placed in a 50 mL round bottom flask. The mixture reaction was flowed with nitrogen gas several times with nitrogen balloon. Next, the reaction was added by the solution of Pd(OAc)_2 (62 mg, 0.28 mmol) and PPh_3 (291 mg, 1.11 mmol) in 1 mL of THF and then refluxed under nitrogen atmosphere at 60-65 $^\circ\text{C}$ overnight. After that, the reaction mixture was cooled to room temperature. Crude reaction was extracted with diethyl ether and water. Then it was purified by column chromatography using hexane as a mobile phase to obtain the mixed products of **THTH1** (0.2378 g) and **THTH1/1** (0.1189 g) (45:20 % by NMR yields) which can't separate. The identical of ^1H NMR (300 MHz, CDCl_3) showed at δ 7.34-7.28 (m, 8H), 7.02 (d, $J = 6.2$ Hz, 4H) ppm. The ^{13}C NMR (75 MHz, CDCl_3) of **THTH1** showed at δ 86.2, 122.9, 127.1, 127.6, 132.1 ppm and the ^{13}C NMR (75 MHz, CDCl_3) of **THTH1/1** showed at δ 76.6, 77.8, 121.9, 127.2, 128.9, 134.4 ppm; HRMS calcd for **THTH1**; $\text{C}_{10}\text{H}_7\text{S}_2$ ($\text{M}+\text{H}^+$): 190.9989, found: 190.9989; HRMS calcd for **THTH1/1**; $\text{C}_{12}\text{H}_7\text{S}_2$ ($\text{M}+\text{H}^+$): 241.9987, found: 241.9987.

3.3.5.3 2, 3-Di(thiophen-2-yl)benzo[*d,e*]chromene (**THTH2**)

The mixture compounds (500 mg) of **THTH1** (333 mg, 1.75 mmol) and **THTH1/1** (167 mg, 0.78 mmol) were placed in a 50 mL round bottom flask. Then the reaction was added by *l*-naphthol (505 mg, 3.50 mmol), **Ru-cymene** catalyst (55 mg, 0.09 mmol), $\text{Cu}(\text{OAc})_2 \cdot \text{H}_2\text{O}$ (3.973 g, 7.00 mmol) and *o*-Xylene (20 mL). Next, the mixture reaction was flowed with nitrogen balloon several times and then refluxed at 80 °C overnight. After that, the reaction mixture was cooled at room temperature. Crude reaction was extracted with ethyl acetate and water. Then it was purified by column chromatography using hexane as a mobile phase to obtain the yellow solid product (0.1050 g, 18 % yield calculated based on **THTH1**); m.p. 182-184 °C; ^1H NMR (300 MHz, CDCl_3) δ 7.50 (d, $J = 7.0$ Hz, 1H), 7.29-7.18 (m, 7H), 7.00 (d, $J = 7.1$ Hz, 1H), 6.88-6.83 (m, 2H), 6.38 (d, $J = 7.1$ Hz, 1H) ppm; ^{13}C NMR (75 MHz, CDCl_3) δ 151.5, 145.9, 135.4, 135.1, 134.0, 131.9, 129.2, 127.9, 127.8, 127.7, 127.6, 127.4, 126.9, 126.3, 123.3, 121.7, 119.2, 115.6, 108.1, 106.7 ppm; HRMS calcd for $\text{C}_{20}\text{H}_{13}\text{OS}_2$ ($\text{M}+\text{H}^+$): 333.0408, found: 333.0408; FTIR: 3050, 1631, 1583, 1490, 1247, 817, 764, 696 cm^{-1} .

3.4 OLEDs study at Polymer Physics Laboratory, National Metal and Materials Technology Center (MTEC) under supervise of Dr. Somboon Sahasithiwat

The pure targeted molecules (**ARAR2**, **ARTH2**, **THTH2**, **ARAR3** and **ARTH3**) were used as an emitter for OLEDs devices. To obtain the current density-voltage-luminance (*J-V-L*) characteristics, devices were recorded by using Minolta LS-110 as a luminance detector and Keithley 2400 source measured as a power supply and multimeter. The device preparation and fabrication details are explained in the following section which will be divided into three steps (*i.e.*, cleaning process, organic coating and metal deposition).

3.4.1 Cleaning process for the patterned ITO glass

The patterned ITO glass substrates sizes 2.5×2.5 cm² were cleaned sequentially with detergent before the deposition of the other layer. They were scrubbed followed by immersing and sonicating with aqueous detergent solution, deionized water, acetone, 2-propanol and hot vapor ethanol, respectively. Finally, they were dried in vacuum oven and cleaned in UV ozone cleanser (Figure 3.1).

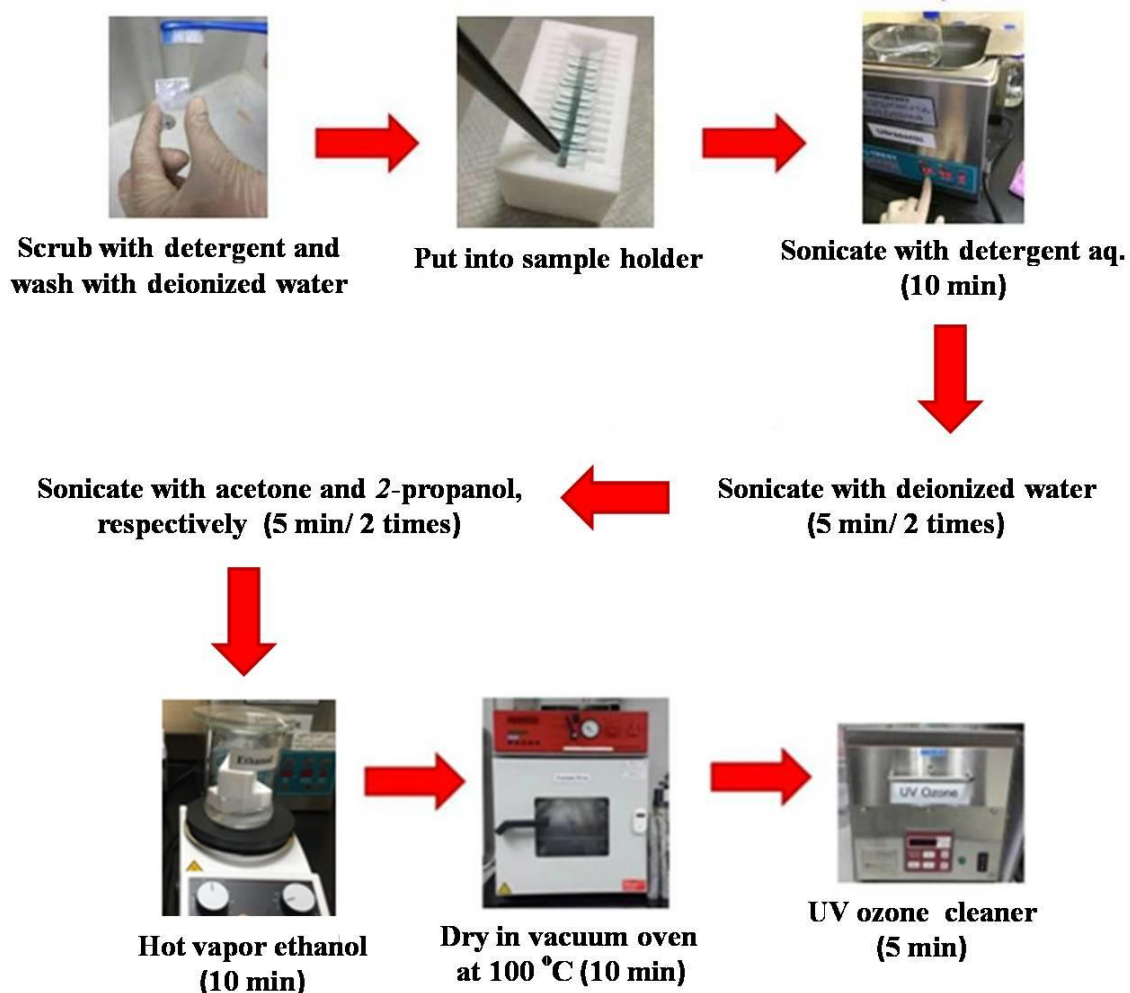


Figure 3.1 Cleaning process of ITO substrate

3.4.2 Organic thin film coating

The organic materials were coated to deposit onto an ITO glass substrate by thermal evaporation under pressure (10^{-6} mbar) at rate of 1 \AA/s in tooling factor of 15.74, which can be monitored in panel. The thickness parameter of NPB, MADN: 20% of target compounds (**ARAR2**, **ARAR3**, **ARTH2**, **ARTH3** and **THTH2**) and Bphen of each layer are 30, 40 and 30nm, respectively (Figure 3.2).

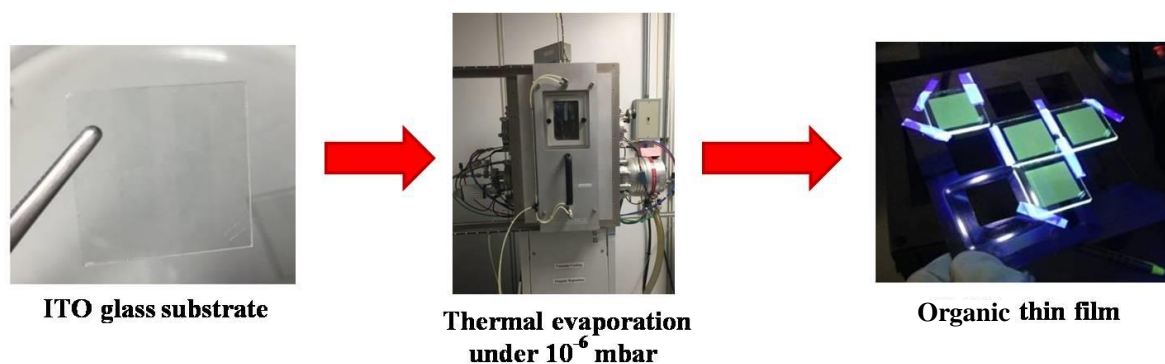


Figure 3.2 Coating process of organic thin film

3.4.3 Metal deposition

The LiF and Al cathodes were sequentially coevaporated through a shadow mask with 5 mm wide slits arranged perpendicularly to the ITO glass substrate form, to obtain an active area of $5 \times 5 \text{ mm}^2$. The operating vacuum for evaporation of this cathode was under pressure (10^{-6} mbar) with rate of 5-10 $\text{\AA}/\text{s}$. The thickness of LiF and Al were 0.5 and 100 nm, respectively (Figure 3.3).



Figure 3.3 Coating process of cathode electrode

3.5 OFETs study at Polymer Physics Laboratory, National Metal and Materials Technology Center (MTEC) under supervise of Dr. Somboon Sahasithiwat

All products were used as a semiconductor for OFETs. To obtain the mobility characteristic, we were recorded by using KEITHLEY 4200 SCS semiconductor parameter analyzer. The mobility was calculated from the saturation region with the following equation: $\mu = (I_{DS})(2L)/(W)(C_i)(V_G - V_T)^2$, where μ is the hole mobility, I_{DS} is the drain-source current, L is the channel length, W is the channel width, C_i is the capacitance per unit area of the gate dielectric layer, and V_G and V_T are the gate voltage and threshold voltage, respectively. The device preparation and fabrication details are explained which divided into three steps (*i.e.*, cleaning process, organic coating and metal deposition).

3.5.1 Cleaning process for the patterned Si/SiO₂ substrate

The patterned Si/SiO₂ substrates sizes 2.0×1.5 cm², as the gate electrode and dielectric layer were cleaned sequentially with 1 %v/v Hellmanex III before the deposition of the other layer. They was scrubbed followed by rinsing in hot water and sonicating in 2-propanol. Next, the substrates were rinsed with deionized water. After that, they were dried with nitrogen gas and cleaned in UV ozone cleanser. The Si/SiO₂ substrates were treated with OTS in an oven at a temperature of 120 °C, forming OTS self-assembled monolayers. The treated substrates were rinsed with toluene. Finally, they were dried in vacuum oven at 85 °C (Figure 3.4).

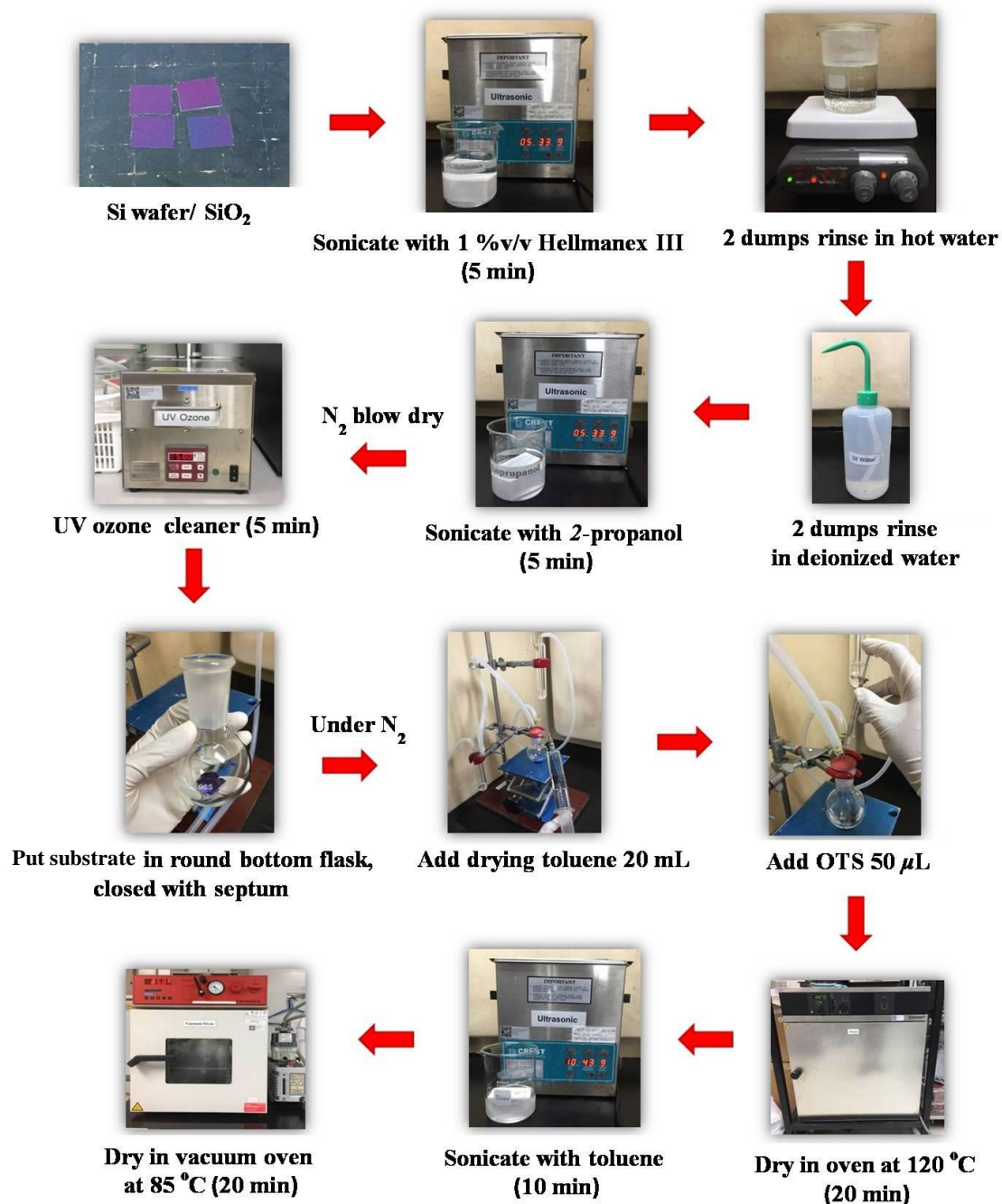


Figure 3.4 Cleaning process of Si/SiO₂ substrate

3.5.2 Organic thin film coating

The organic compounds (**ARAR2**, **ARAR3**, **ARTH2**, **ARTH3** and **THTH2**) were coated onto a substrate by thermal evaporation under pressure (10^{-6} mbar), rate of 0.1 \AA/s and heat substrates (T_{sub}) at $80 \text{ }^\circ\text{C}$. The thickness of organic semiconductor layer was 30 nm (Figure 3.5).

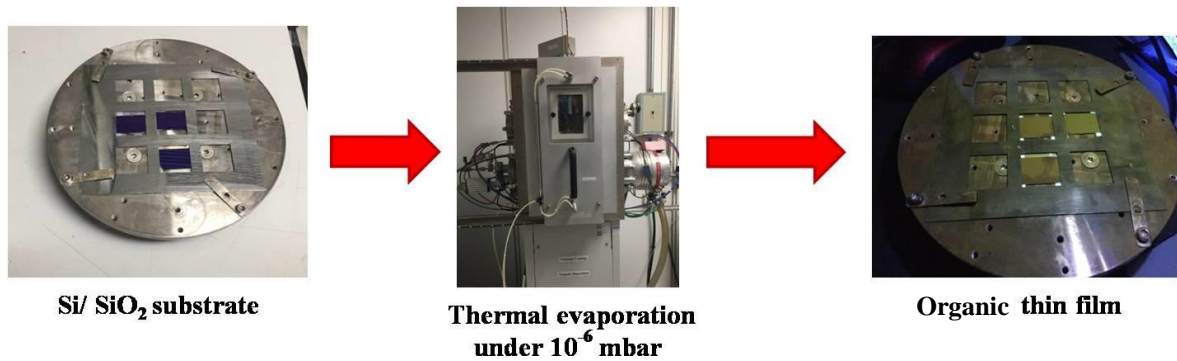


Figure 3.5 Coating process of organic thin film

3.5.3 Metal deposition

The Au source-drain-gate electrodes were sequentially evaporated through a shadow mask with $17 \text{ mm} \times 20 \mu\text{m}$ wide slits arranged perpendicularly to obtain an active area on thin films. The operating vacuum for evaporation of this electrode was under pressure (10^{-6} mbar) with rate of $5\text{-}10 \text{ \AA/s}$. The thickness of Au was 100 nm (Figure 3.6).



Figure 3.6 Coating process of source-drain-gate electrodes

CHAPTER 4

RESULTS AND DISCUSSIONS

Five target compounds of benzo[*d,e*]chromene and thioarene derivatives (**ARAR2**, **ARAR3**, **ARTH2**, **ARTH3** and **THTH2**) are shown in Figure 4.1.

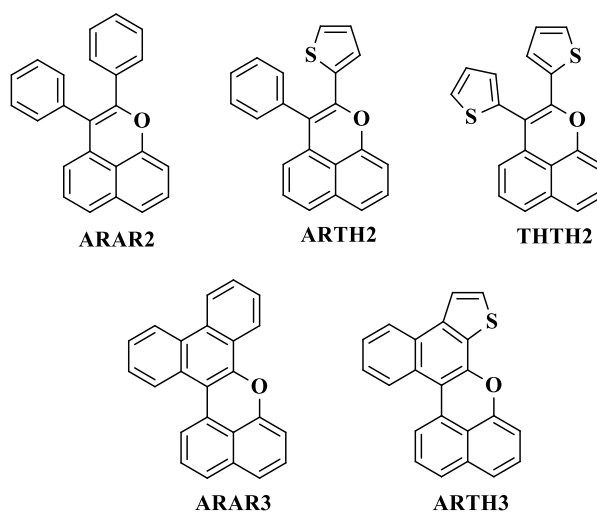


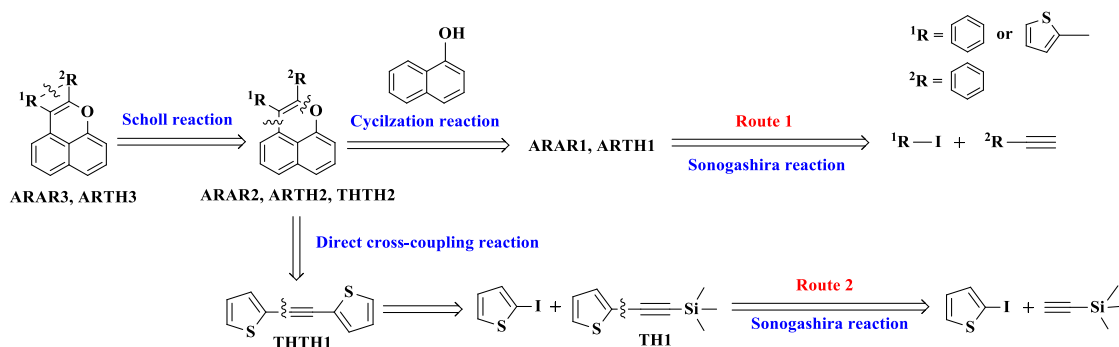
Figure 4.1 Molecular structures of the target compounds

This chapter is divided into seven parts.

- (I) Synthesis and reaction mechanism
- (II) Characterization and structure identification
- (III) Photophysical study
- (IV) Electrochemical study
- (V) Thermal study
- (VI) OLEDs performance
- (VII) OFETs performance

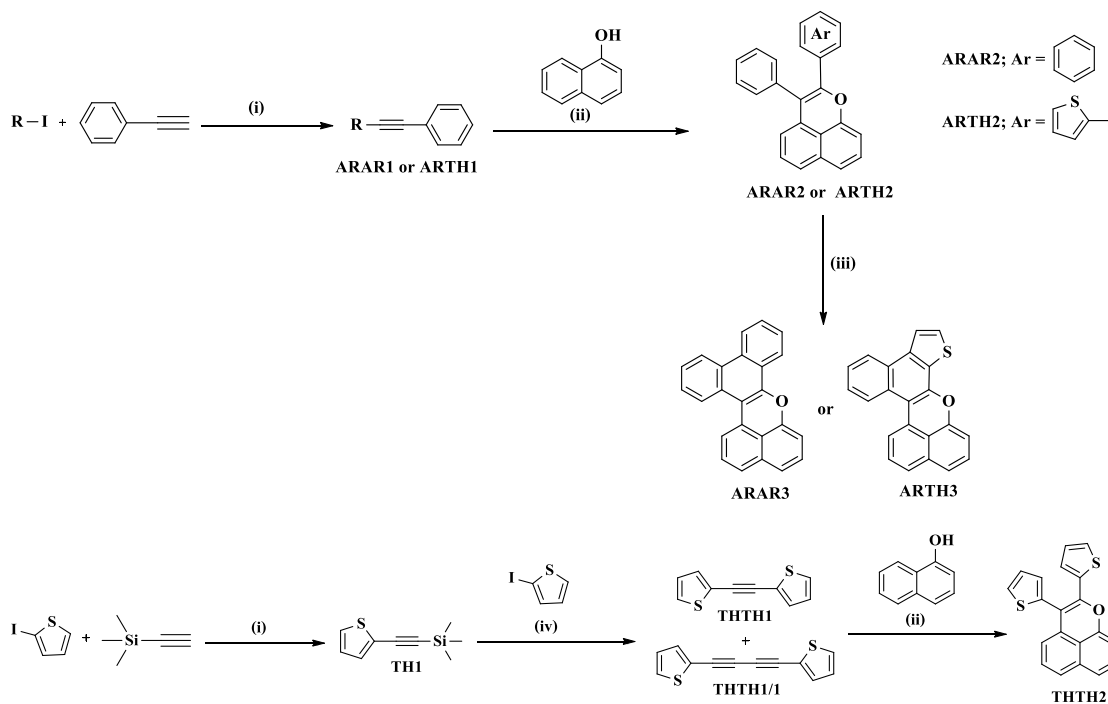
4.1 Synthesis and reaction mechanism

The synthetic route of benzo[*d,e*]chromenes (**ARAR2** and **ARAR3**) and thioarenes (**ARTH2**, **ARTH3** and **THTH2**) were designed and shown in Scheme 4.1. The synthetic pathway used Sonogashira, direct cross-coupling, ruthenium cyclization and Scholl reactions. The conditions are displayed in Scheme 4.2.



Scheme 4.1 The synthetic pathway for the target molecules

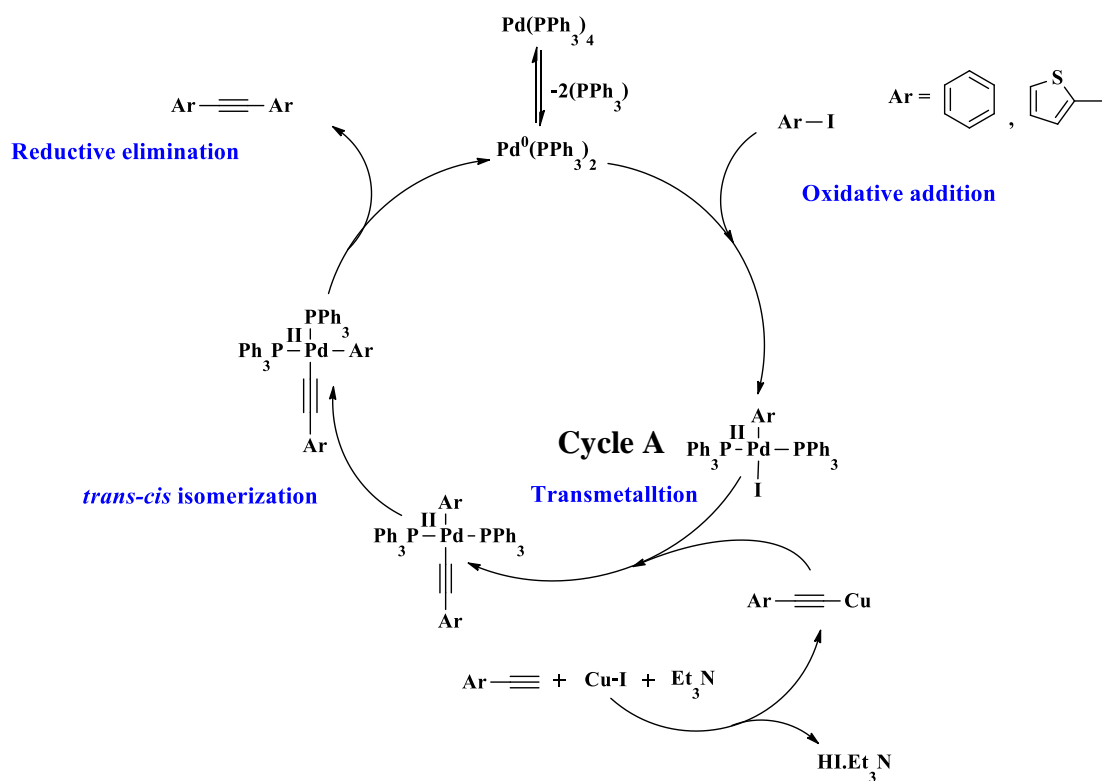
To obtain **ARAR2** and **ARTH2**, in the first step, the Sonogashira reaction was performed with palladium (0) catalyzed to give **ARAR1** and **ARTH1** (Route 1). After that, the intermediates were cyclized with *l*-naphthol in the condition of ruthenium catalytic. The **ARAR3** and **ARTH3** were synthesized by the Scholl reaction. In another route, the **TH1** was obtained from Sonogashira reaction and subjected to direct cross-coupling reaction with 2-iodothiophene to obtain **THTH1**. Compound **THTH2** was synthesized with similar approach as it used for **ARAR3** and **ARTH3** (Route 2).



Scheme 4.2 The conditions; (i) 0.1% Pd(PPh₃)₄, 0.05% CuI, Et₃N, reflux at 60 °C for 5 hr: (98%, 91% and 88% for ARAR1, ARTH1 and TH1), (ii) 5% Ru-cymene, 4 eq. Cu(OAc)₂•H₂O, *o*-Xylene, reflux at 80 °C for 22 hr: (73%, 57% and 18% for ARAR2, ARTH2 and THTH2), (iii) 6 eq. FeCl₃, CH₃NO₂, dried CH₂Cl₂, stirr at 0 °C for 1 hr: (75% and 32% yields for ARAR3 and ARTH3) and (iv) 0.5 eq. Ag₂CO₃, 1 eq. Bu₄NCl, 0.1 eq. PPh₃, 5% Pd(OAc)₂, THF, reflux at 60-65 °C for 6 hr: (45: 20% 0.2 by NMR yield for THTH1: THTH1/1)

4.1.1 Sonogashira reaction

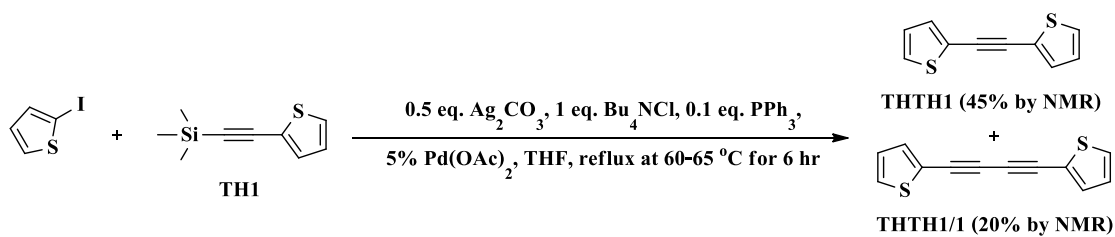
The mechanism of Sonogashira reaction (for the synthesis of **ARAR1**, **ARTH1** and **TH1**) are shown in Scheme 4.3. The first step, the ligand was dissociated in palladium complex before entering to cycle A. In oxidative addition step, the catalyst inserted to the carbon-halogen bond of aryl iodide. Then it went through transmetallation with alkyne complex to give a square planar palladium (II). Then, the *trans*- orientation converted to *cis*- in a *trans-cis* isomerization step. Finally, reductive elimination of palladium (II) gave the carbon-carbon bond meanwhile the catalyst (0) was regenerated and returned to catalytic cycle.



Scheme 4.3 Sonogashira reaction mechanism for ARAR1, ARTH1 and TH1

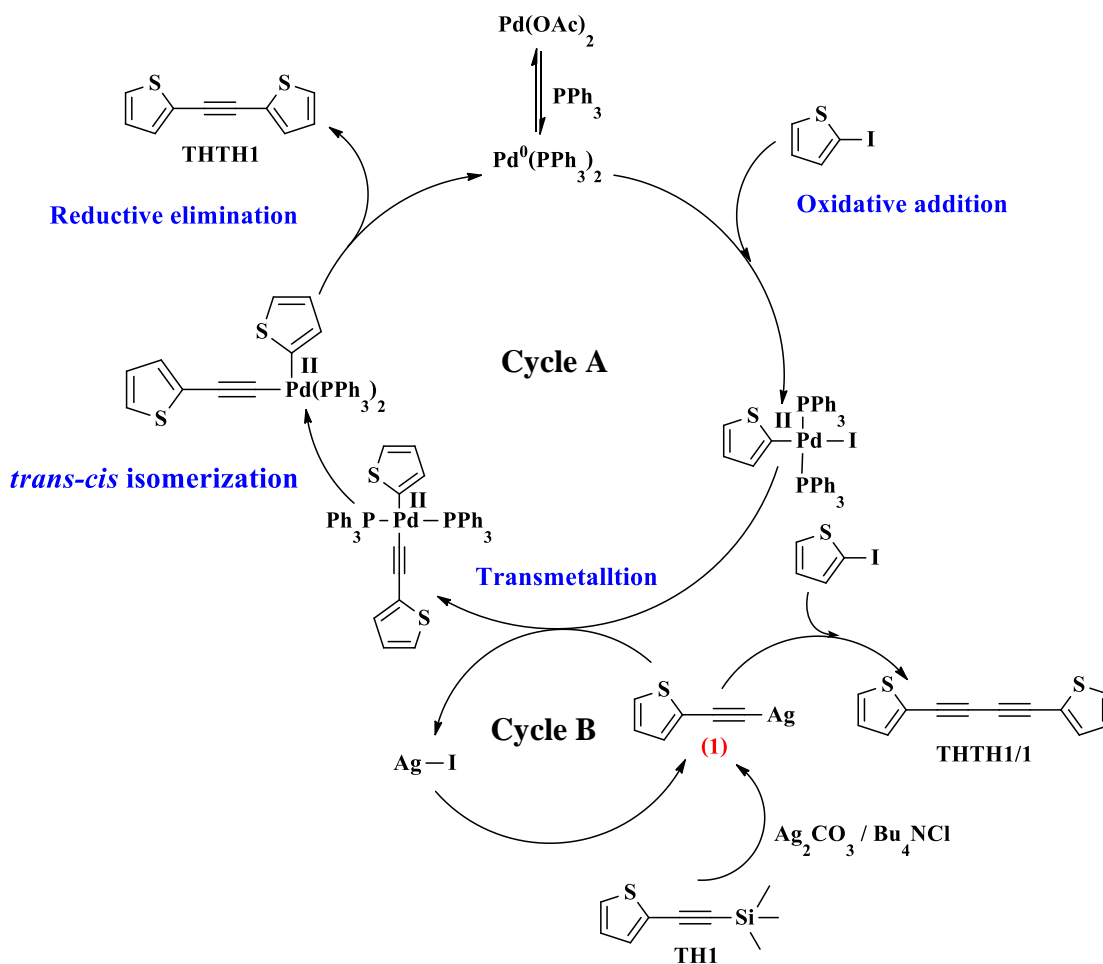
4.1.2 Direct cross-coupling reaction

For the synthesis of **THTH1**, the target intermediate was synthesized by using a direct cross-coupling reaction between an alkynylsilane and aryl iodide, with palladium (II) catalyst in the presence of Ag_2CO_3 [46] in Scheme 4.4. After completed reaction, the crude reaction was monitored by TLC. It was found that not only cross-coupling product (**THTH1**) was formed but a significant amount of homo-coupling product (**THTH1/1**) was also observed (2: 1 by ^{13}C NMR for **THTH1**: **THTH1/1**). We tried to separate the mixed cross and homo products. Unfortunately, with the similar polarity, they unable to separate via column chromatography. Another approach, $\text{Pd}(\text{PPh}_3)_4$ was used instead of $\text{Pd}(\text{OAc})_2$ but it was unsuccessful to improve the % yield.



Scheme 4.4 Synthesis pathway for THTH1

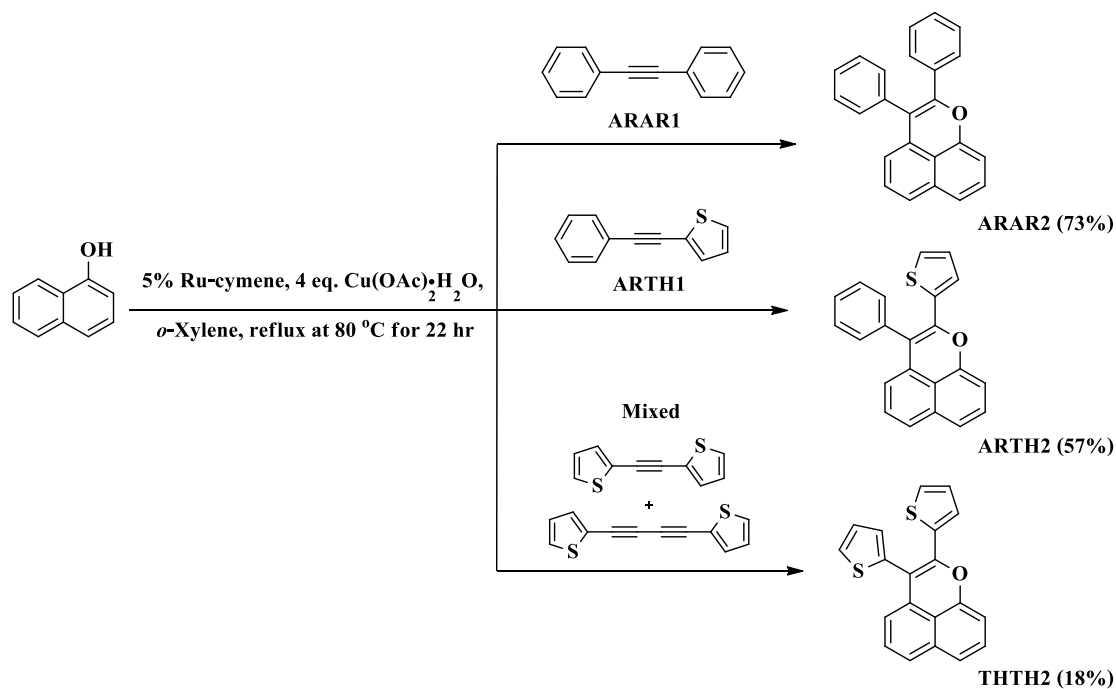
The reaction mechanism of direct cross-coupling reaction for **THTH1** and **THTH1/1** formation is shown in Scheme 4.5. In cycle A, the cross-coupling product was obtained with the same mechanism as it was described in Sonogashira reaction. However, the significant amount of homo-coupling was formed via cycle B. Two possible ways of the intermediate (**1**) proceeded either reacted with starting material (**TH1**) or transmetallation.



Scheme 4.5 Direct cross-coupling reaction mechanism for THTH1 and THTH1/1

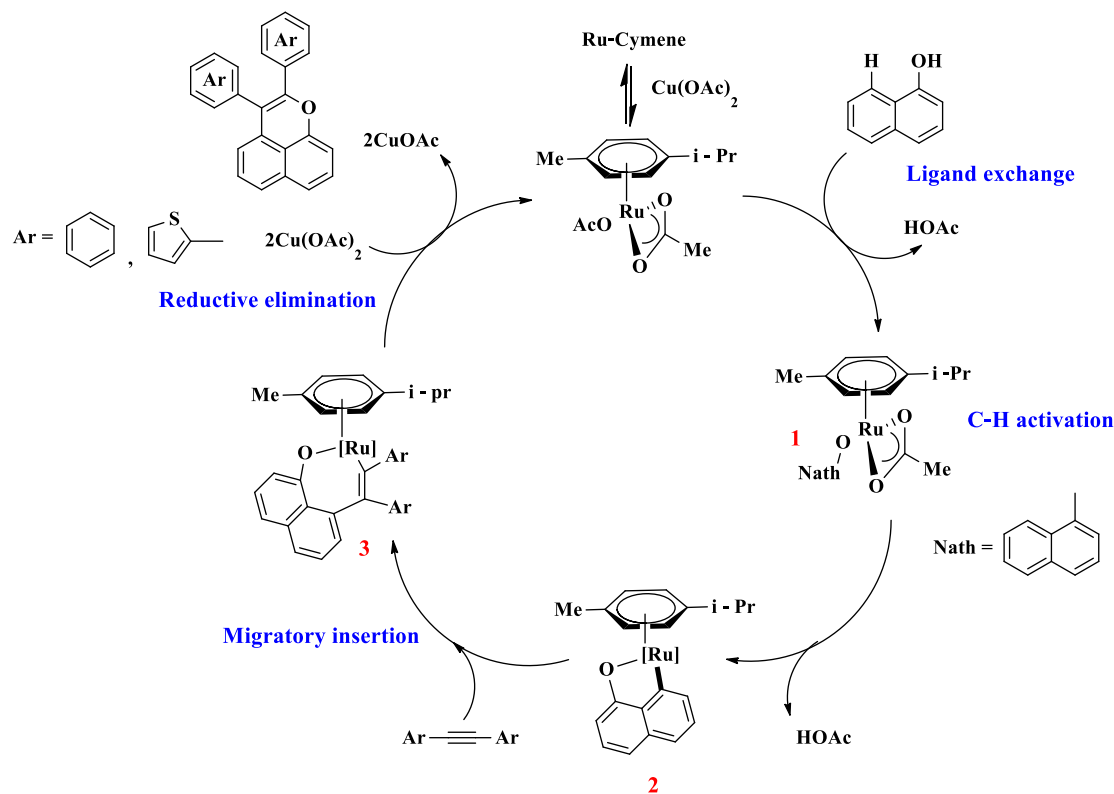
4.1.3 Ruthenium cyclization reaction

The ruthenium cyclization reaction with *l*-naphthol was used to obtain ARAR2, ARTH2 and THTH2 in Scheme 4.6. The target products were obtained for 73%, 57%, 18% yields, respectively. For THTH2 synthesis, a mixture THTH1 and THTH1/1 was used. It was found that the major product observed THTH2 from THTH1 and *l*-naphthol with some residue of the mixed products. By using column chromatography the pure THTH2 was obtained in 18% yield.



Scheme 4.6 Synthesis pathways for ARAR2, ARTH2 and THTH2

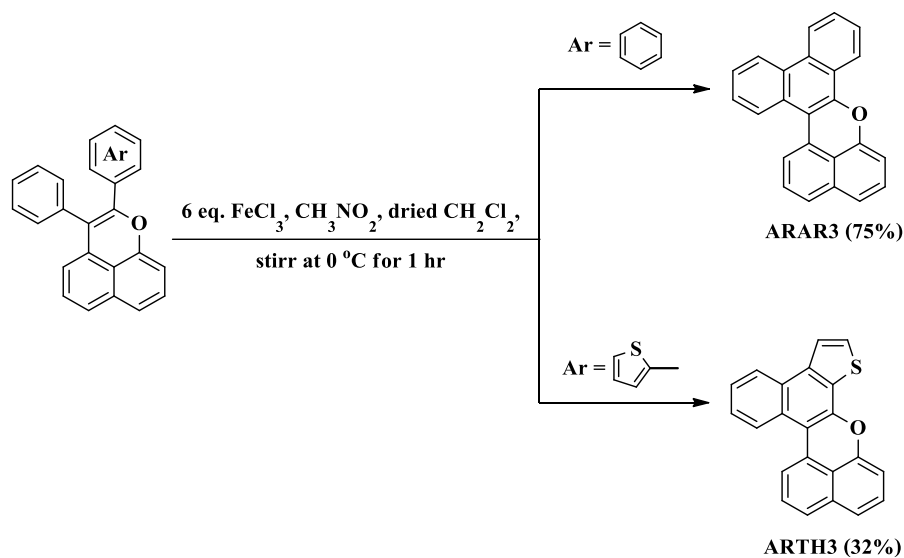
The reaction mechanism for ruthenium cyclization reaction to form **ARAR2**, **ARTH2** and **THTH2** is shown in Scheme 4.7. Firstly, the ligand of **Ru-cymene** was replaced. Then the ligand exchange of Ru intermediate generated intermediate **1** with *l*-naphthol. The five-membered compound **2** was formed by C-H activation and release acetic acid (HOAc). After that, the migratory insertion of alkyne into the ruthenium-carbon bond afforded intermediate **3** and the reductive elimination step gave a desired product.



Scheme 4.7 Ruthenium cyclization reaction mechanism for ARAR2, ARTH2 and THTH2

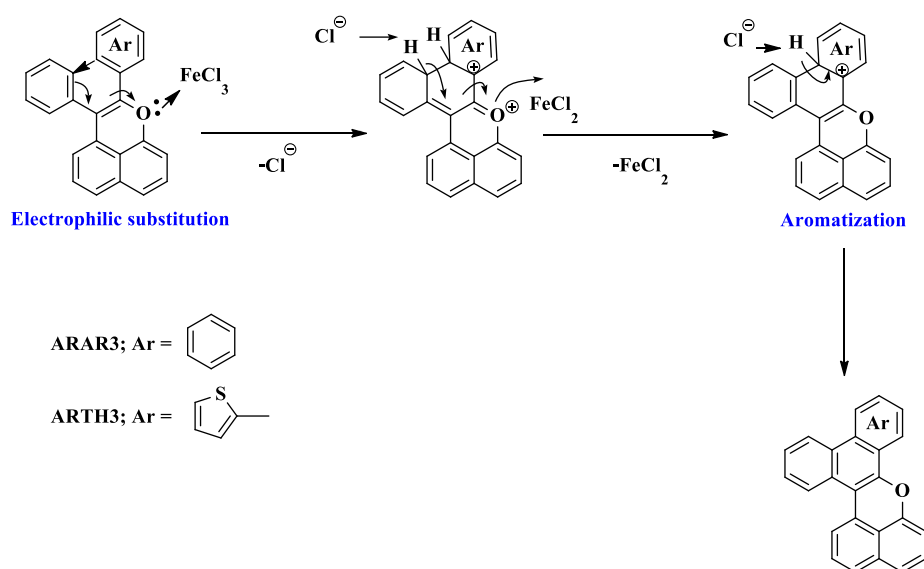
4.1.4 Scholl reaction

After ruthenium cyclization reaction were successfully, **ARAR2** and **ARTH2** were used for ring closure via Scholl reaction. The reaction screening were studied by a varied equivalent of FeCl_3 (6-15 eq.) as an oxidative reagent. It was found that the optimized condition was obtained with 6 equivalents of FeCl_3 to give a good yield. The target products (**ARAR3** and **ARTH3**) were obtained in 75% and 32% yields, respectively in Scheme 4.8.



Scheme 4.8 Synthesis pathways for ARAR3 and ARTH3

The Scholl reaction was proposed involving the aromatic substitution activated with the Lewis acid (FeCl_3). The aromatization was performed to get the cyclization products.



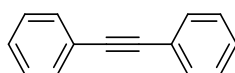
Scheme 4.9 Scholl reaction mechanism for ARAR3 and ARTH3

4.2 Characterization and structure identification

All compounds were characterized by ^1H and ^{13}C NMR, FT-IR, melting point and mass spectroscopy. FT-IR and mass spectrum are shown in Appendix. In this chapter, the ^1H and ^{13}C NMR will be divided into two parts of intermediate and target compounds.

4.2.1 ^1H and ^{13}C NMR characterization of intermediate compounds

4.2.1.1 1, 2-Diphenylethyne (ARAR1)



ARAR1 (98%)

^1H NMR spectrum of **ARAR1** is shown in Figure 4.2. With a symmetry molecule, the signal showed only two signals with the chemical shifts at 7.54 ppm (d, $J = 7.4$ Hz, 4H) assigned to *meta*-position (H_a) and 7.36-7.34 ppm (m, 6H) assigned to *ortho*- and *para*-positions (H_b) on phenyl rings, respectively.

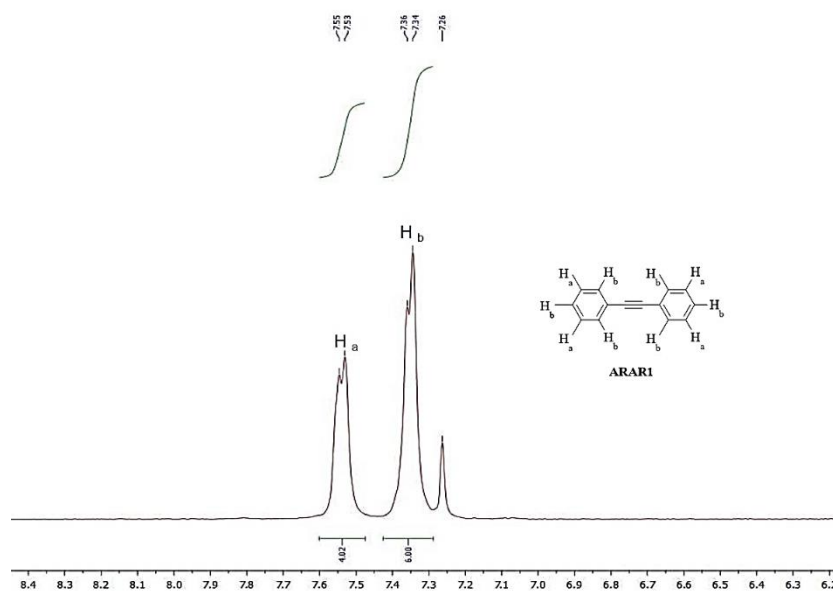
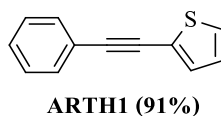


Figure 4.2 ^1H NMR in CDCl_3 and the assignment of ARAR1

4.2.1.2 2-(Phenylethynyl)thiophene (**ARTH1**)

^1H NMR spectrum of **ARTH1** is shown in Figure 4.3. The chemical shifts showed at 7.63 ppm (dd, $J = 6.0, 2.6$ Hz, 2H) assigned to proton signals of *meta*-position (H_a) on phenyl rings, 7.44-7.34 ppm (m, 5H) assigned to H_b on phenyl and thiophene rings and 7.09 ppm (t, $J = 7.0$ Hz, 1H) assigned to H_c position on thiophene ring, respectively.

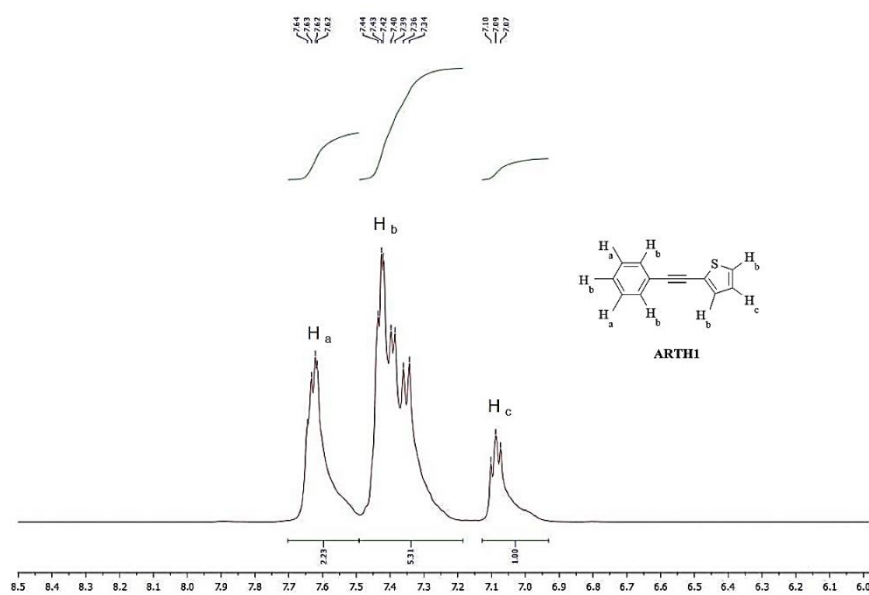
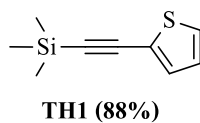


Figure 4.3 ^1H NMR in CDCl_3 and the assignment of **ARTH1**

4.2.1.3 Trimethyl(2-thienylethynyl)silanen (**TH1**)

^1H NMR spectrum of **TH1** in Figure 4.4, the chemical shifts at 7.25 ppm (d, $J = 5.4$ Hz, 2H) was assigned to H_a position and a signal at 6.98 ppm (dd, $J = 5.0$ Hz, 3.8 Hz, 1H) was assigned to H_b position on thiophene ring. The signal at 0.28 ppm (s, 9H) was assigned to C-H signals of TMS group.

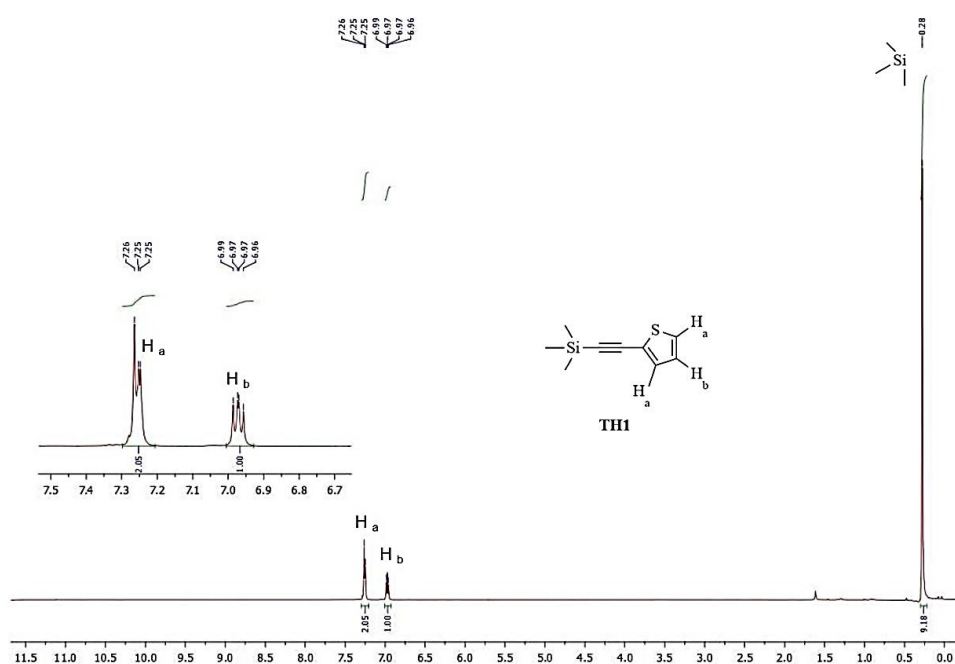
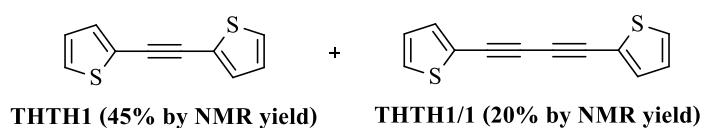


Figure 4.4 ^1H NMR in CDCl_3 and the assignment of **TH1**

4.2.1.4 Mixed products of 1, 2-di(thiophen-2-yl)ethyne (**THTH1**) and 1,4-di(thiophen-2-yl)buta-1,3-diyne (**THTH1/1**)



^1H NMR spectrum of **mixed THTH1** and **THTH1/1** is shown in Figure 4.5. The results showed that the exact data were obtained. We cannot identify the structure with the chemical shifts at 7.34-7.28 ppm (m, 8H) and 7.02 ppm (d, $J = 6.2$ Hz, 4H). However, the structures of mixed products were clearly characterized and resolved by using ^{13}C NMR spectroscopy in Figure 4.6. The ^{13}C NMR signals of cross-coupling product were observed at 86.2, 122.9, 127.1, 127.6 and 132.1 ppm assigned to C_1 , C_2 , C_5 , C_3 and C_4 , respectively. Additionally, the signals of homo-coupling product were observed at 76.6, 77.8, 121.9, 127.2, 128.9 and 134.4 ppm assigned to C_1' , C_2' , C_3' , C_6' , C_4' and C_5' , respectively. With the ^{13}C NMR in hand, the ratio of the mixture at low field carbons (C_4 and C_5') can be determined with carbon intensity. It was found that the ratio at 2: 1 for cross-coupling: homo-coupling products was observed.

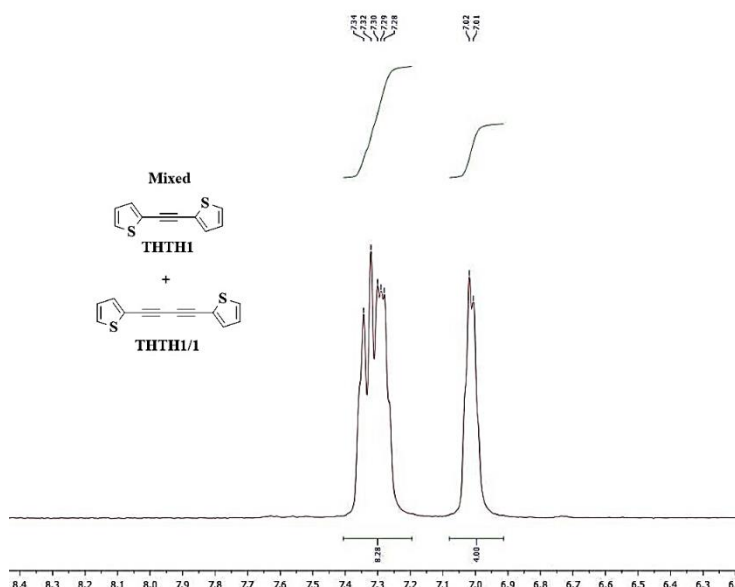


Figure 4.5 ^1H NMR in CDCl_3 of mixed **THTH1** and **THTH1/1**

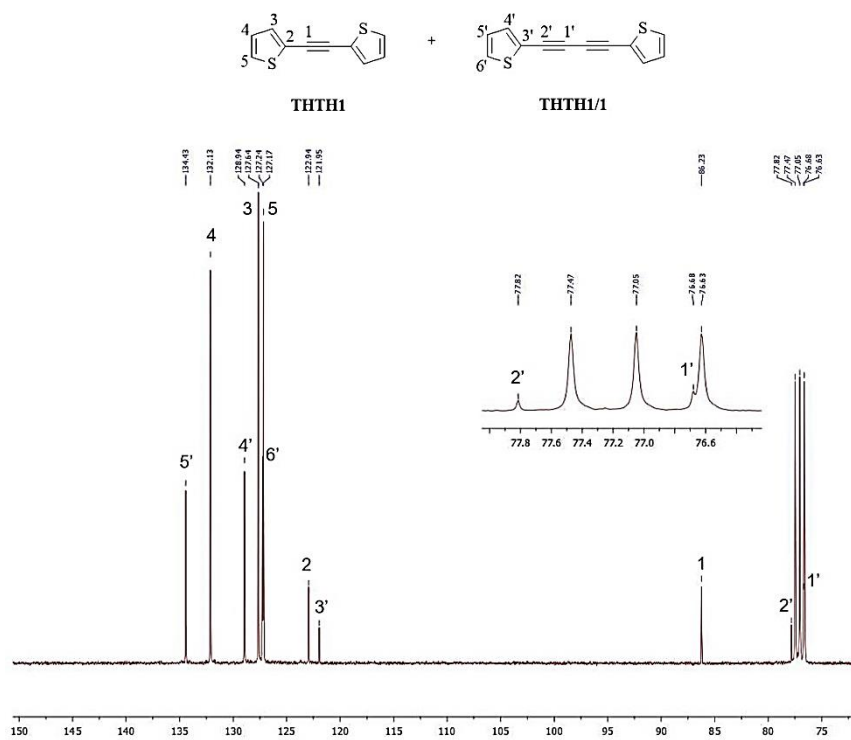


Figure 4.6 ^{13}C NMR in CDCl_3 and the assignment of THTH1 and THTH1/1

4.2.2 ^1H and ^{13}C NMR characterization of target compounds

The ^1H NMR spectrum of final compounds were shown and compared in Figure 4.7. The high field chemical shifts around 6.2-6.4 and 6.8-6.9 ppm were characterized with H_1 and H_3 positions which was assigned as *ortho*- and *para*-positions on core structure of benzo[*d,e*]chromene.

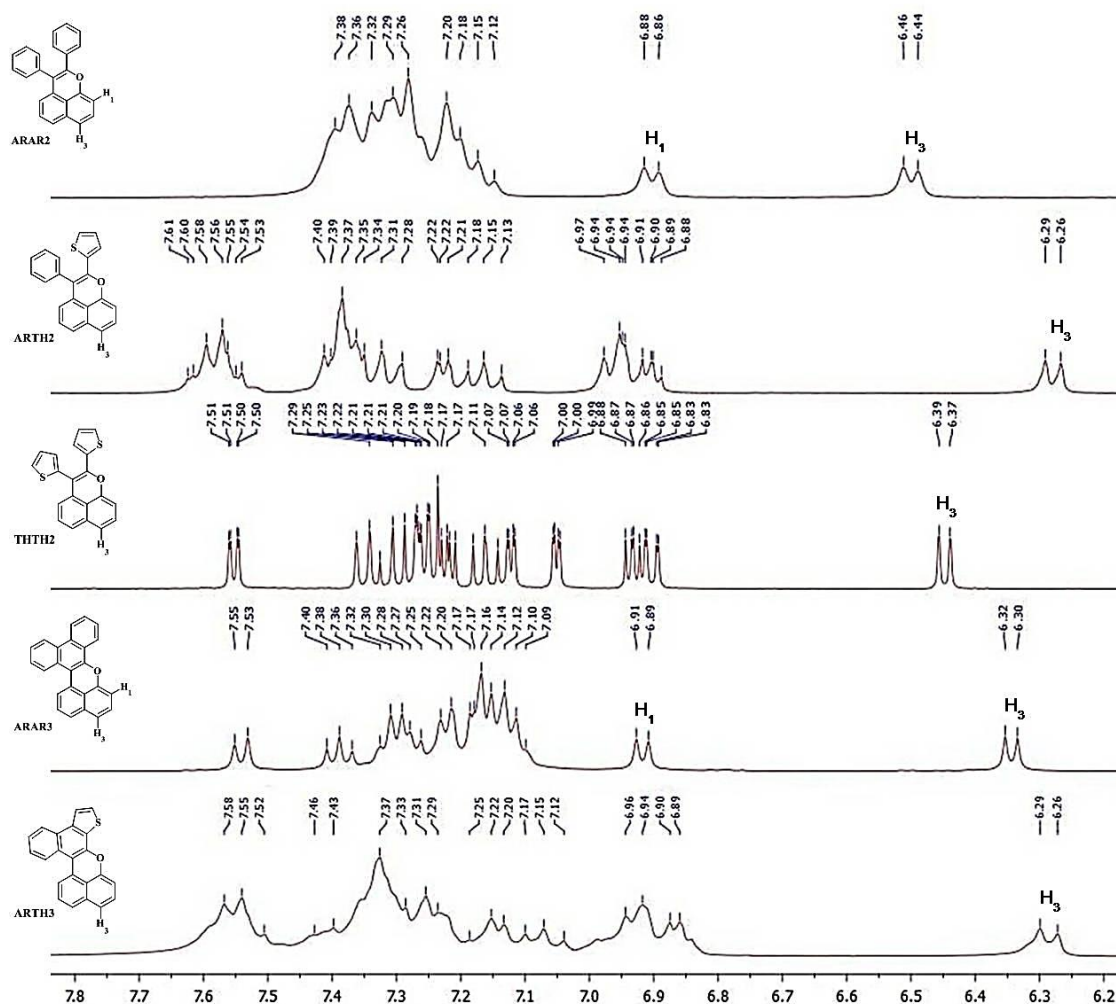


Figure 4.7 ^1H NMR in CDCl_3 and the assignment of five target products

The ^{13}C NMR comparison spectrum of target products are shown in Figure 4.8. It can be seen that the quaternary carbon connected with oxygen atom of the benzo[*d,e*]chromene core appeared at a low field (144-153 ppm) because of the inductive effect from high electronegativity of the oxygen atom. With the ^{13}C NMR in hand, the varied quaternary carbons of different aromatic at 144-150 were assigned to C₆, whereas the similar quaternary carbon at 152 ppm were assigned to C₁. Furthermore, we found a new quaternary carbon around 125 and 129 ppm of the closed ring with Scholl reaction (**ARAR3** and **ARTH3**) which were two signals of C₉ and C₁₀.

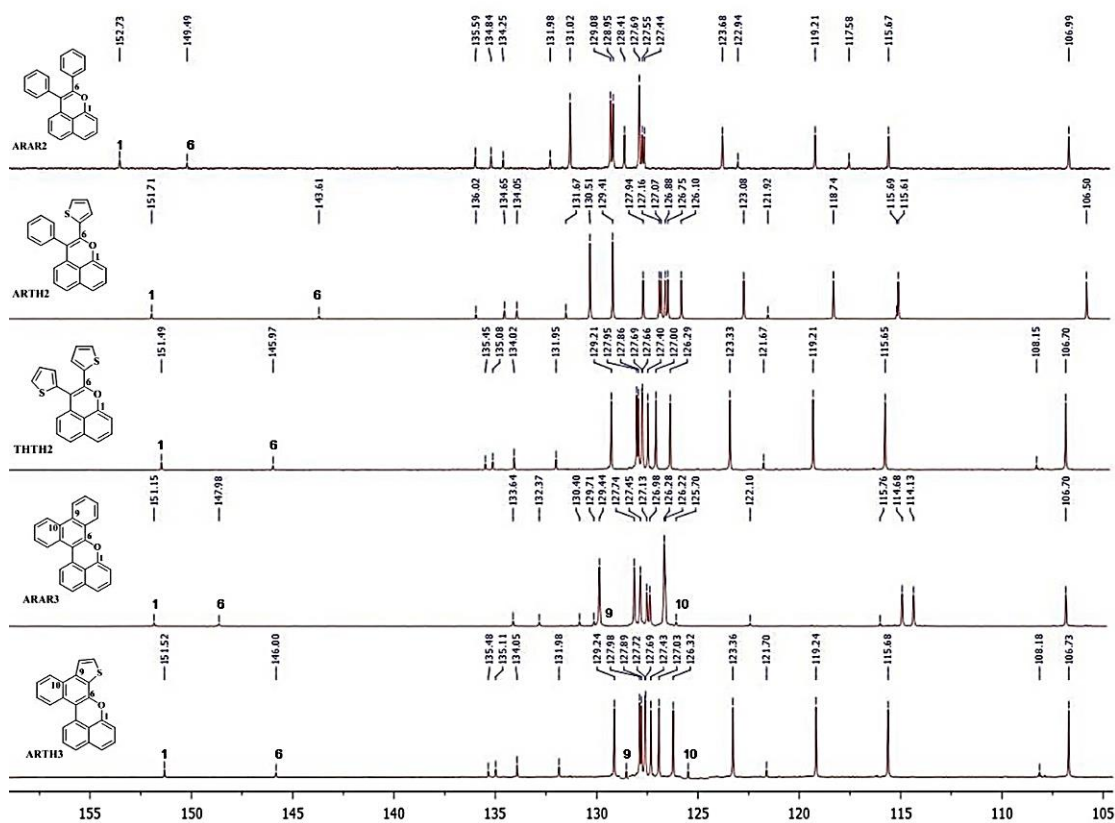


Figure 4.8 ^{13}C NMR in CDCl_3 and the assignment of all target products

For **ARTH2**, we used 2D NMR (correlation spectroscopy, COSY and heteronuclear multiple bond correlation spectroscopy, HMBC) for resolving the molecular isomer. COSY spectrum is shown in Figure 4.9. With the correlation of H₁, H₂ and H₃, they were confirmed that all these positions were the proton signals in benzo[*d,e*]chromene ring. The coupling constants of H₁ and H₂ (J₁₂) and H₂ and H₃ (J₂₃) were detected at 7.2 and 8.6 Hz, respectively. We also found a correlation of H_z with H_x and H_y that the low coupling constants of thiophene were detected at 4.6 and 5.9 Hz.

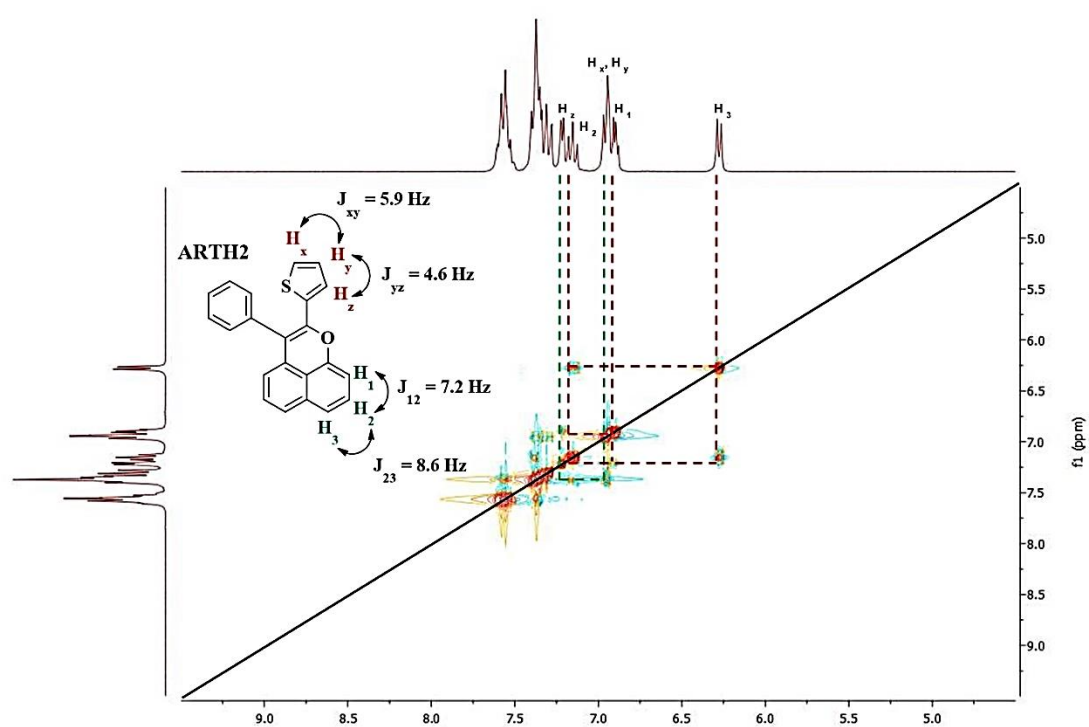


Figure 4.9 COSY spectrum in CDCl₃ and the relation of ARTH2

In addition, HMBC spectrum of **ARTH2** (Figure 4.10) showed the long correlation between carbon and proton connectivity. It was found that the quaternary carbon (C_6) correlated with H_y and H_z on the thiophene moiety. These data confirmed the position of thiophene ring on structure of **ARTH2**.

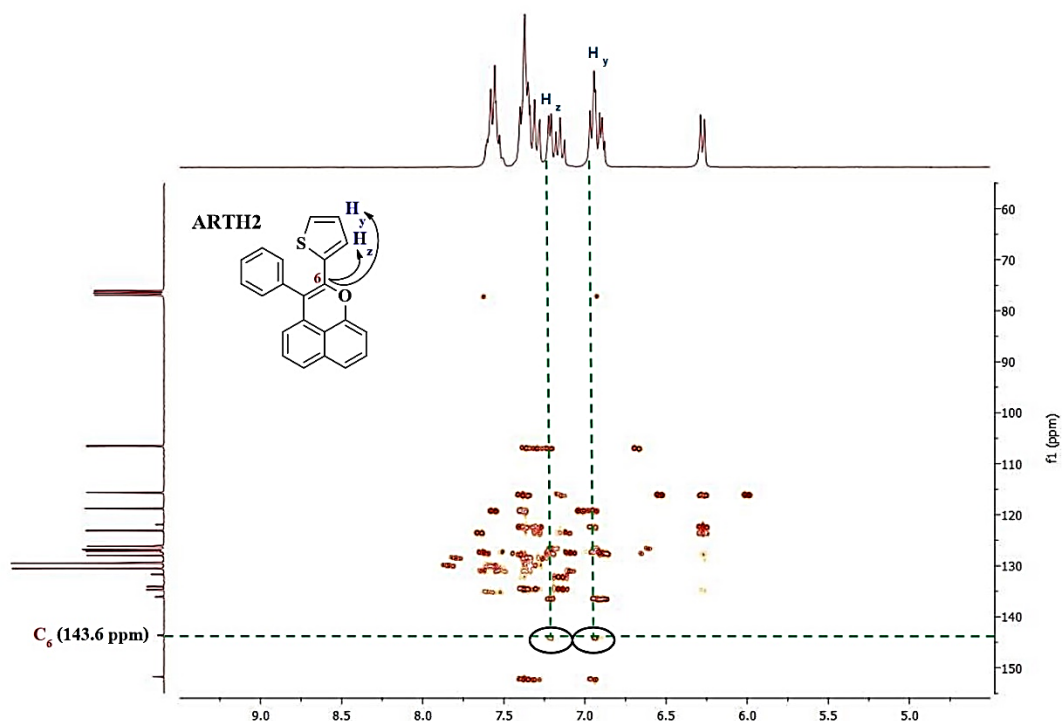
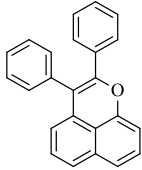
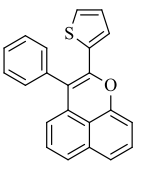
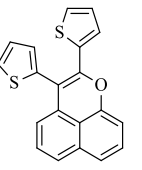
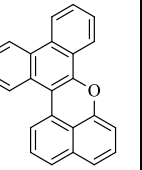
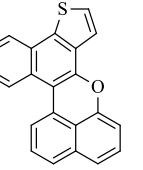


Figure 4.10 HMBC spectrum in $CDCl_3$ and the relation of **ARTH2**

The key functional groups of **ARAR2**, **ARTH2**, **THTH2**, **ARAR3** and **ARTH3** were characterized by FT-IR. The compounds showed the signal of sp^2 C-H stretching, aromatic C-C stretching, aromatic C=C stretching, C-O stretching, sp^2 C-H bending and aromatic C-H bending, C-S stretching and C-S bending which are summarized in Table 4.1.

Table 4.1 FT-IR characterization of all targeted

Structure Mode	Wavenumber (cm ⁻¹)				
	 ARAR2	 ARTH2	 THTH2	 ARAR3	 ARTH3
sp ² C-H stretching	3,047	3,059	3,050	3,054	3,047
C-C aromatic stretching	1,580 and 1,365	1,585	1,583	1,579 and 1,306	1,591
C=C aromatic stretching	1,638	1,637	1,631	1,636	1,637
C-O stretching	1,248	1,252	1,247	1,251	1,247
sp ² C-H bending	810	817	817	828	840
C-H aromatic bending	683	684	696	695	696
C-S stretching	-	1,492	1,490	-	1,492
C-S bending	-	765	764	-	753

The summerization data of percent yield, physical appearance, melting point and mass spectroscopy of all compounds are listed in Table 4.2.

Table 4.2 Characterization and structure identification for all compounds

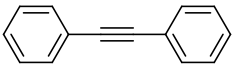
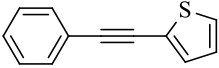
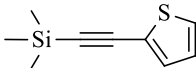
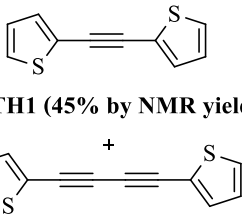
Structure	Physical appearance	Formular	m.p. (°C)	Mass (m/z)	
				Calcd	Found
 ARAR1 (98% yield)	 white crystal	C ₁₄ H ₁₀	54-55	179.0861 (M+H ⁺)	179.0861 (M+H ⁺)
 ARTH1 (91% yield)	 pale yellow solid	C ₁₂ H ₈ S	49-50	185.0425 (M+H ⁺)	185.0391 (M+H ⁺)
 TH1 (88% yield)	 pure yellow liquid	C ₉ H ₁₂ SSi	-	181.0507 (M+H ⁺)	181.0501 (M+H ⁺)
<p>Mixed product</p>  THTH1 (45% by NMR yield) THTH1/1 (20% by NMR yield)	 pale yellow powder	C ₁₀ H ₆ S ₂ for THTH1 C ₁₂ H ₆ S ₂ for THTH1/1	78-79	190.9989 (M+H ⁺) for THTH1 241.9987 (M+H ⁺) for THTH1/1	190.9989 (M+H ⁺) for THTH1 241.9987 (M+H ⁺) for THTH1/1

Table 4.2 Characterization and structure identification for all compounds (continued)

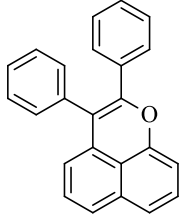
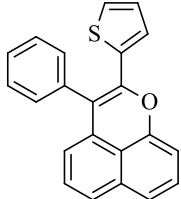
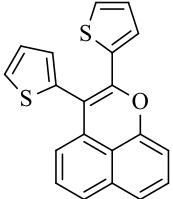
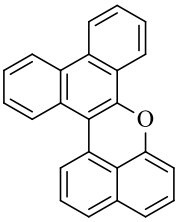
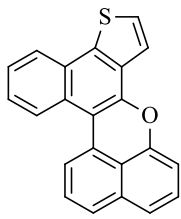
Structure	Physical appearance	Formular	m.p. (°C)	Mass (m/z)	
				Calcd	Found
 <p>ARAR2 (73% yield)</p>	 <p>yellow solid</p>	C ₂₄ H ₁₆ O	134-138	321.1279 (M+H ⁺)	321.1279 (M+H ⁺)
 <p>ARTH2 (57% yield)</p>	 <p>yellow solid</p>	C ₂₂ H ₁₄ OS	136-140	327.0844 (M+H ⁺)	327.0844 (M+H ⁺)
 <p>THTH2 (18% yield)</p>	 <p>yellow solid</p>	C ₂₀ H ₁₂ OS ₂	182-184	333.0408 (M+H ⁺)	333.0408 (M+H ⁺)
 <p>ARAR3 (75% yield)</p>	 <p>yellow solid</p>	C ₂₄ H ₁₄ O	162-164	341.0942 (M+Na ⁺)	341.0944 (M+Na ⁺)

Table 4.2 Characterization and structure identification for all compounds (continued)

Structure	Physical appearance	Formular	m.p. (°C)	Mass (m/z)	
				Calcd	Found
 <p>ARTH3 (32% yield)</p>	 <p>yellow solid</p>	C ₂₄ H ₁₂ OS	170-172	347.0507 (M+Na ⁺)	347.0507 (M+Na ⁺)

4.3 Photophysical study

Five target compounds were investigated for the photophysical properties with two factors. The first is to investigate the influence of different electron donor substituted on the benzo[*d,e*]chromene core. Second, the flexibility or rigidity affect to photophysical properties. The UV-Visible absorption spectra at 2×10^{-6} M sample solutions in spectroscopic toluene were measured at room temperature. The UV-Visible absorption spectra of **ARAR2**, **ARTH2**, **THTH2**, **ARAR3** and **ARTH3** are shown in Figure 4.11 and λ_{\max} are summarized in Table 4.3.

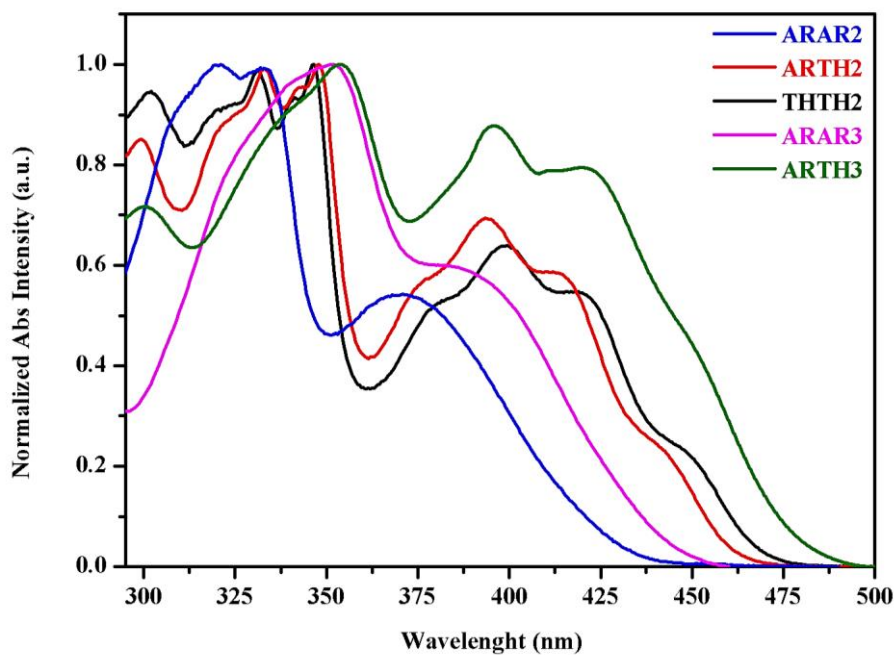


Figure 4.11 UV-Visible absorption spectra of target products

Table 4.3 The maximum absorption wavelengths of products in toluene solution

Compound	$\lambda_{\text{max,abs}}$ (nm)
ARAR2	320, 333, 371
ARTH2	332, 348, 375, 393, 413
THTH2	331, 346, 380, 399, 420
ARAR3	351, 383
ARTH3	354, 395, 396, 422

The target compounds give two main absorption bands. The maximum absorption bands located in the region of 320-365 nm originated from the delocalized π - π^* transition of benzo[*d,e*]chromene moiety. Moreover, the spectra showed peak around 366-500 nm which was assigned to the delocalized n - π^* transition. More detail on photophysical properties related molecular structure are discussed below.

The comparison of the UV-Visible absorption spectra of **ARAR2** and **ARTH2** are displayed in Figure 4.12. These two molecules were designed with different substitution. It was clearly seen that the absorption spectrum of **ARTH2** gave a red-shifted because of internal hydrogen bonding of sulfur atom and hydrogen phenyl ring.

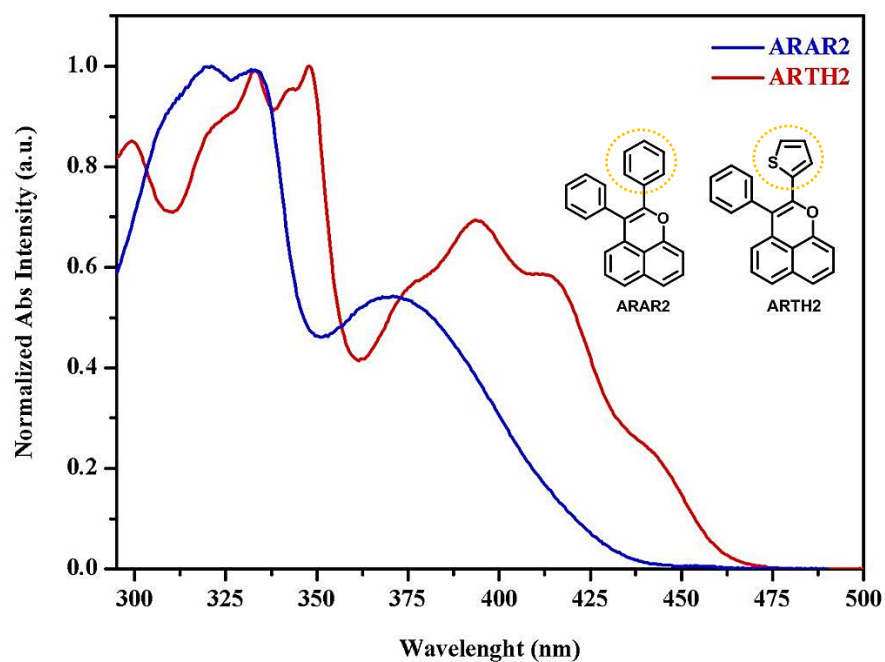


Figure 4.12 UV-Visible absorption spectra and structures of ARAR2 and ARTH2

Next, the investigation on the number of thiophene in the benzo[*d,e*]chromene core structure specifically **ARTH2** and **TTH2** (Figure 4.13). It was clearly seen that the similar absorption spectra were observed. That could be explained by frontier molecular orbitals and the planar molecules of both molecules (Figure 4.19).

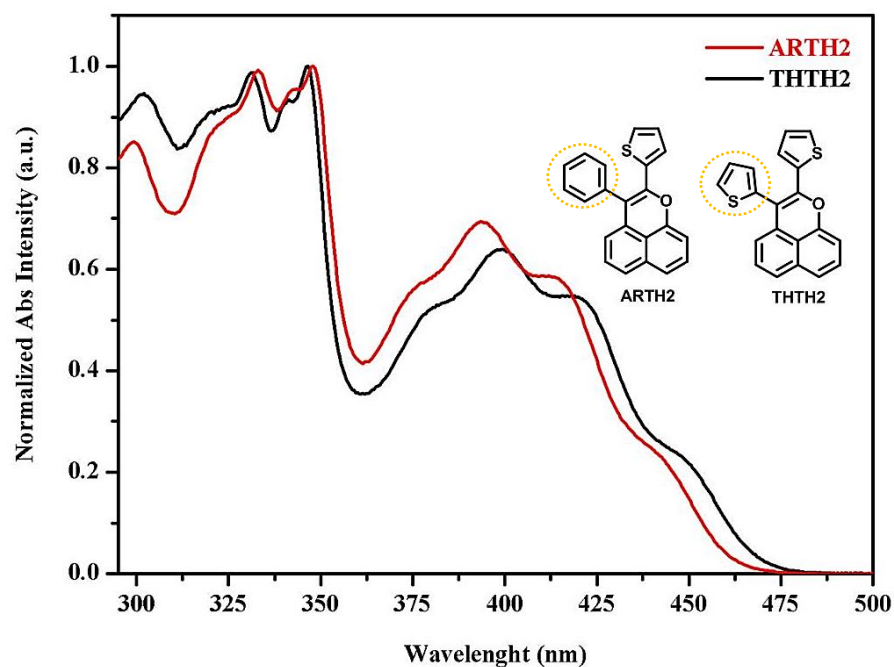


Figure 4.13 UV-Visible absorption spectra and structures of ARTH2 and TTH2

The comparison of the UV-Visible absorption spectra of **ARAR2** and **ARAR3** are displayed in Figure 4.14. These two molecules were designed to investigate the flexibility. It was clearly seen that both absorption spectrum of the rigid compounds gave a bathochromic (red) with hyperchromic shifts. From this observation, the fully conjugated absorption originated from the planar molecules could be a responsible.

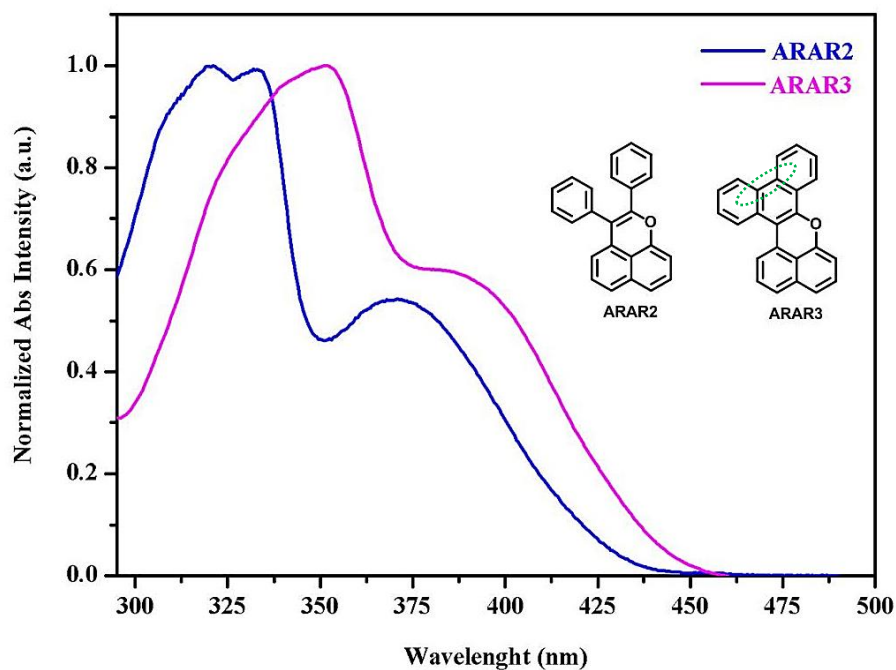


Figure 4.14 UV-Visible absorption spectra and structures of ARAR2 and ARAR3

The comparison of the UV-Visible absorption spectra of **ARAR3** and **ARTH3** are displayed in Figure 4.15. The closed ring phenyl-phenyl and phenyl-thiophene moieties connected to the benzo[*d,e*]chromene were designed. It was clearly seen that the absorption spectrum of **ARTH3** gave a red-shifted of $n-\pi^*$ transition with higher intensity from a rich electron aromatic thiophene.

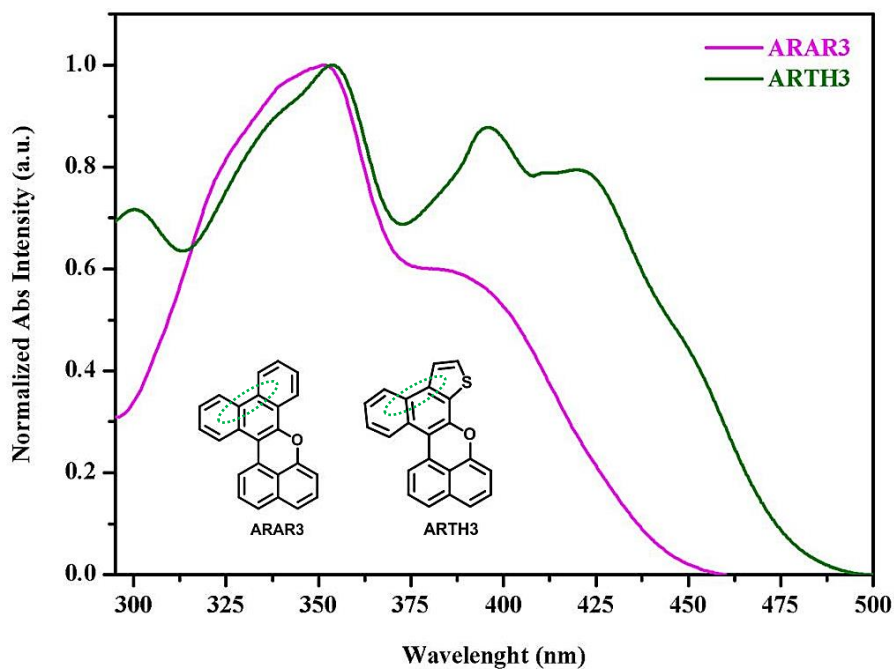


Figure 4.15 UV-Visible absorption spectra and structures of ARAR3 and ARTH3

The photoluminescence spectra measured in toluene solutions (2×10^{-7} M) at room temperature (Figure 4.16) gave the maximum emission wavelength at 490-513 nm which located in range of green regions. Their compounds exhibited nanosecond scale (ns) lifetime ($\tau_{f, 300K}$) with fluorescence process. The lifetime spectra of all compounds were showed in the Appendix and summarized in Table 4.4.

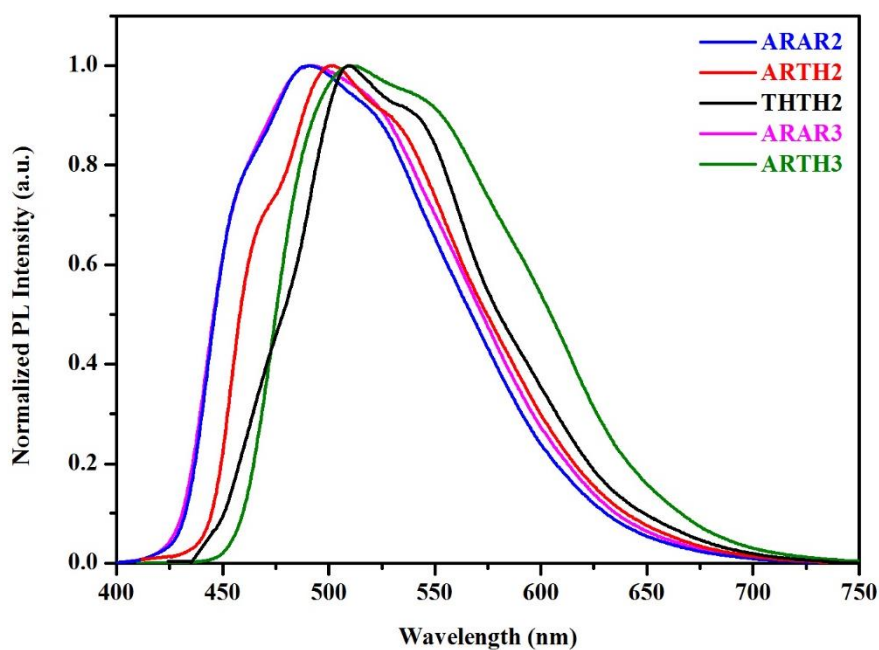


Figure 4.16 Photoluminescence spectra of target products

Table 4.4 Photoluminescence characteristics of all products in toluene solution

Compound	$\lambda_{\max, \text{em}}$ (nm)	$\tau_{f, 300K}$ (ns)
ARAR2	490	3.10
ARTH2	502	2.82
THTH2	508	2.46
ARAR3	495	2.76
ARTH3	513	2.55

The solution photoluminescence quantum efficiencies in toluene (2×10^{-6} M) were observed for **ARAR2** (16.23%), **ARTH2** (22.01%), **THTH2** (8.46%), **ARAR3** (18.06%) and **ARTH3** (26.74%). These data related to the emission photographs of the solutions under UV light in Figure 4.17. The low quantum yield of **THTH2** (8.46%) gave a weak emission light. Surprisingly, the emission photographs of **THTH2** in solid and solution states was not related. It originated that **THTH2** exhibited an aggregation-induced emission (AIE) [47].

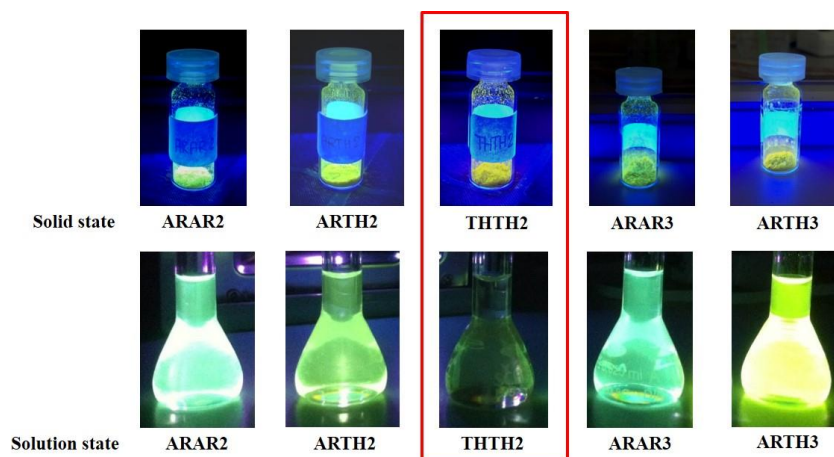


Figure 4.17 All target products in solid state (top) and solution (below) under UV lamp

4.4 Electrochemical study

The electrochemical properties were investigated by cyclic voltammetry (Figure 4.18). The cyclic voltammogram of target molecules in acetonitrile (1×10^{-3} M) containing $(\text{Bu}_4\text{N})\text{PF}_6$ (0.1 M) were measured with a glassy carbon (GC) electrode, scan rate at 50 mV/s under argon atmosphere and reported compared with ferrocene/ferrocenium ion (Fc/Fc^+) as an external standard (4.8 eV). The results showed that the quasi-reversible both oxidation and reduction were obtained. The data was summarized in Table 4.5.

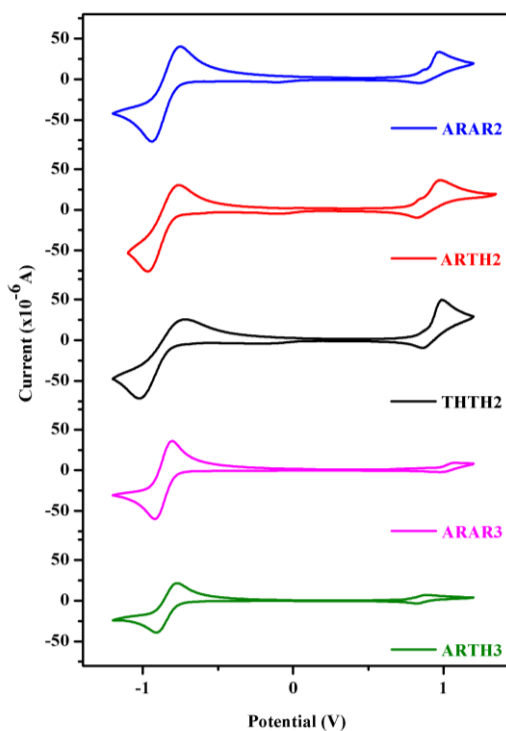


Figure 4.18 Cyclic voltammogram of target products reported compared with ferrocene/ferrocenium ion

The highest occupied molecular orbital (HOMO) and lowest unoccupied molecular orbital (LUMO) energy levels of materials were estimated according to the electrochemical performance and UV-Visible absorption spectra. The energy band gap (E_g) was estimated according to onset of absorption spectra ($E_g = 1240/\lambda_{onset}$). The LUMO energy level was calculated from equation $E_{LUMO} = -e (E_{re, onset} + 4.8 \text{ eV} - E_{1/2, Fe/Fe^+})$. Whereas the HOMO energy level was calculated from equation $E_g = LUMO - HOMO$. The detail for HOMO and LUMO calculation are described in the Appendix.

Table 4.5 Electrochemical property and energy levels of products

Compound	$E_{\text{re, onset}}$ (V)	E_{LUMO} (eV)	λ_{onset} (nm)	E_{g} (eV)	E_{HOMO} (eV)
ARAR2	-0.77	-3.60	435	2.85	-6.45
ARTH2	-0.79	-3.58	462	2.68	-6.26
TTH2	-0.78	-3.59	469	2.64	-6.23
ARAR3	-0.74	-3.63	446	2.78	-6.41
ARTH3	-0.76	-3.61	485	2.56	-6.17

The frontier energy levels of all target products were summarized in Figure 4.19. The HOMO energy levels of **ARAR2**, **ARTH2**, **TTH2**, **ARAR3**, and **ARTH3** were calculated to be -6.45, -6.26, -6.23, -6.41 and -6.17 eV, respectively. The LUMO energy levels of **ARAR2**, **ARTH2**, **TTH2**, **ARAR3**, and **ARTH3** were estimated -3.60, -3.58, -3.59, -3.63 and -3.61 eV, respectively. The results showed that the similar HOMO with varied LUMO was obtained in Figure 4.19.

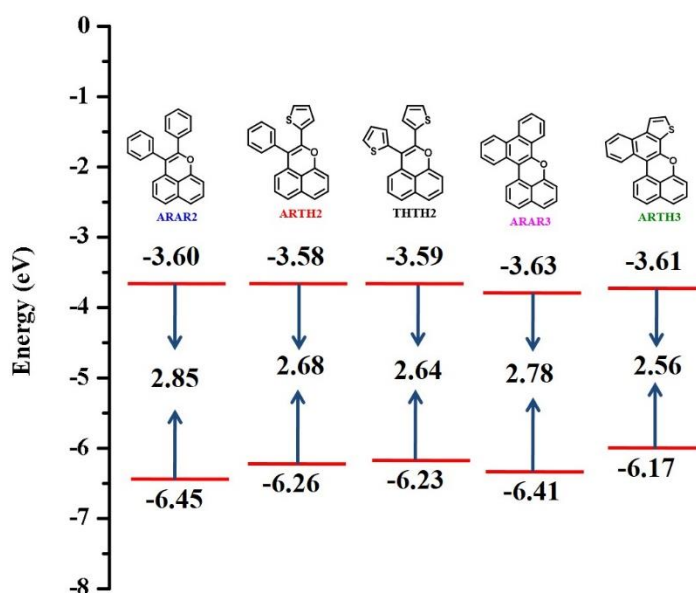


Figure 4.19 Schematic HOMO and LUMO levels of target products

4.5 Thermal study

The thermal properties of products were investigated by thermal gravimetric analysis (TGA) under nitrogen atmosphere. Curves of weight loss are shown in Figure 4.20. The TGA results showed that the compounds exhibited good thermal stability with decomposition temperatures in the range of 160-250 °C. By comparing all thioarene derivatives, it was found that **ARTH2**, **ARTH3** and **THTH2** show higher thermal stability than these **ARAR2** and **ARAR3**.

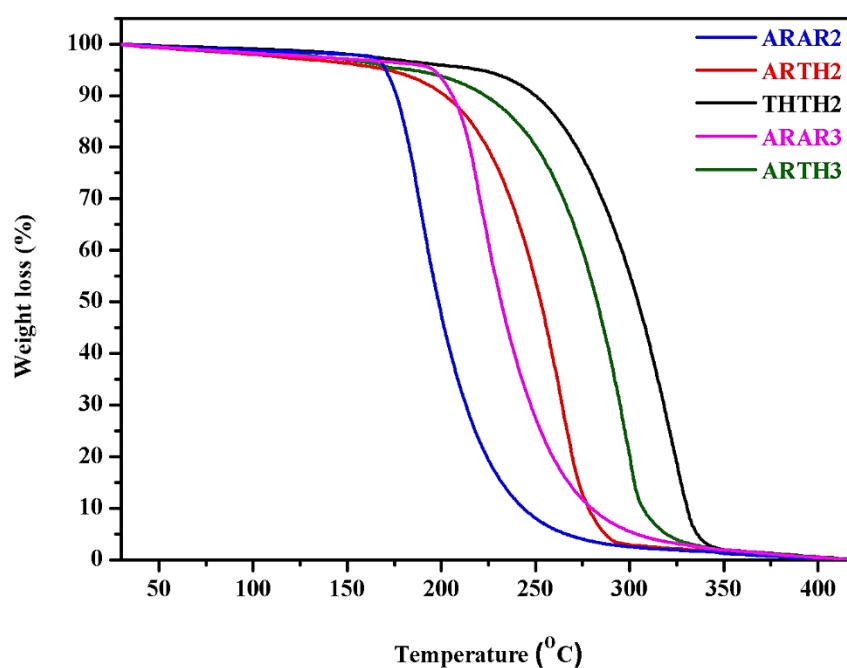


Figure 4.20 TGA curves of target products

4.6 OLED performances

For the preliminary evaluation of the electroluminescence performances, the **ARTH2** compound has been studied as the emitter of OLEDs. The maximum luminance of the device based on different configurations are shown in Table 4.6. From all data, it can be concluded that device **6** showed a good OLEDs efficiency at the maximum luminance 4,699 cd/m². In this devices, indium tin oxide (ITO) was used as the anode, (*N,N'*-diphenyl)-*N,N'*-bis(*1*-naphthyl)-*1,1'*-biphenyl-4,4'-diamine (NPB) was used as the hole transporting layer, 2-methyl-9,10-bis(naphthalen-2-yl)anthracene (MADN) was used as the host material, 4,7-diphenyl-1,10-phenanthroline (Bphen) was used as the electron transport and hole/exciton-blocking layer, LiF was used as the electron injection layer, and Al was used as the cathode. The device configuration and the corresponding HOMO and LUMO energy levels of the materials used in the work are depicted in Figure 4.21.

Table 4.6 The optimization of OLEDs device fabrication

Device	Configuration	Max. luminance (cd/m ²)
1	ITO/ ARTH2 (60nm)/Ca(10nm)/Al(100nm)	-
2	ITO/PEDOT:PSS/ ARTH2 (60nm)/Ca(10nm)/Al(100nm)	-
3	ITO/PEDOT:PSS/ ARTH2 (40nm)/Ca(10nm)/Al(100nm)	-
4	ITO/NPB(30nm)/ ARTH2 (40nm)/Bphen(30nm)/ LiF(0.5nm)Al(100nm)	2,570
5	ITO/NPB(30nm)/MADN:30% ARTH2 (40nm)/ Bphen(30nm)/LiF(0.5nm)Al(100nm)	4,284
6	ITO/NPB(30nm)/MADN:20% ARTH2 (40nm)/ Bphen(30nm)/LiF(0.5nm)Al(100nm)	4,699

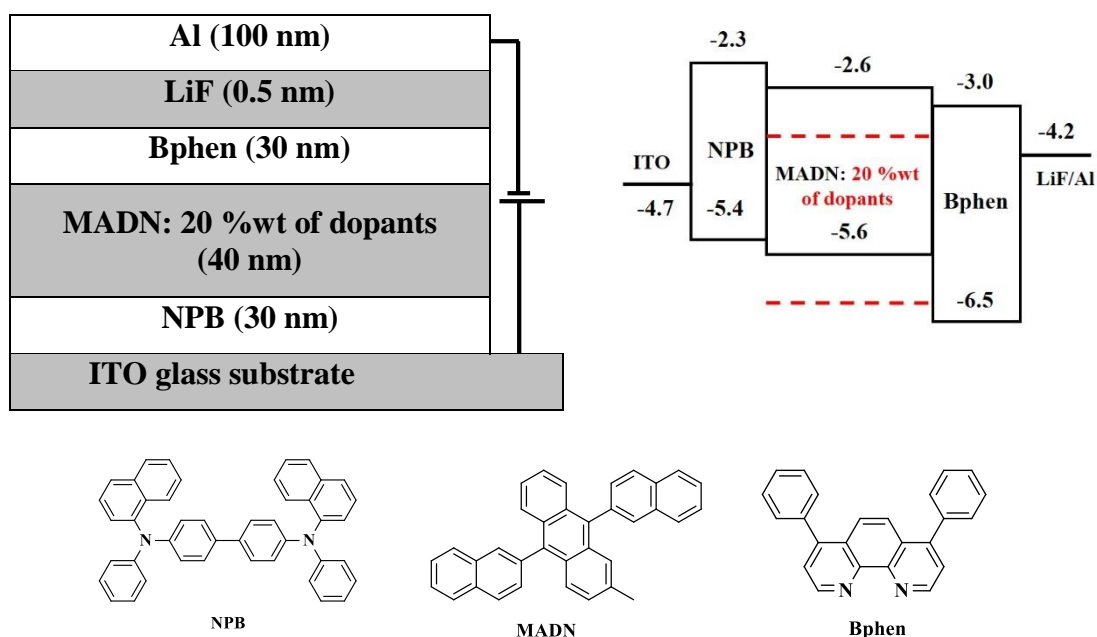


Figure 4.21 OLEDs device configuration (upper left), the relative HOMO and LUMO energy levels of the materials investigated in this work (upper right) and structures of NPB, MADN and Bphen (bottom)

With the optimized device in hand, all five compounds of **ARAR2**, **ARTH2**, **THTH2**, **ARAR3**, and **ARTH3** also were used as dopants for study the performance. The current density-voltage-luminance (*I-V-L*) characteristics are shown in Figure 4.22. Their electroluminescence performance data are summarized in Table 4.7.

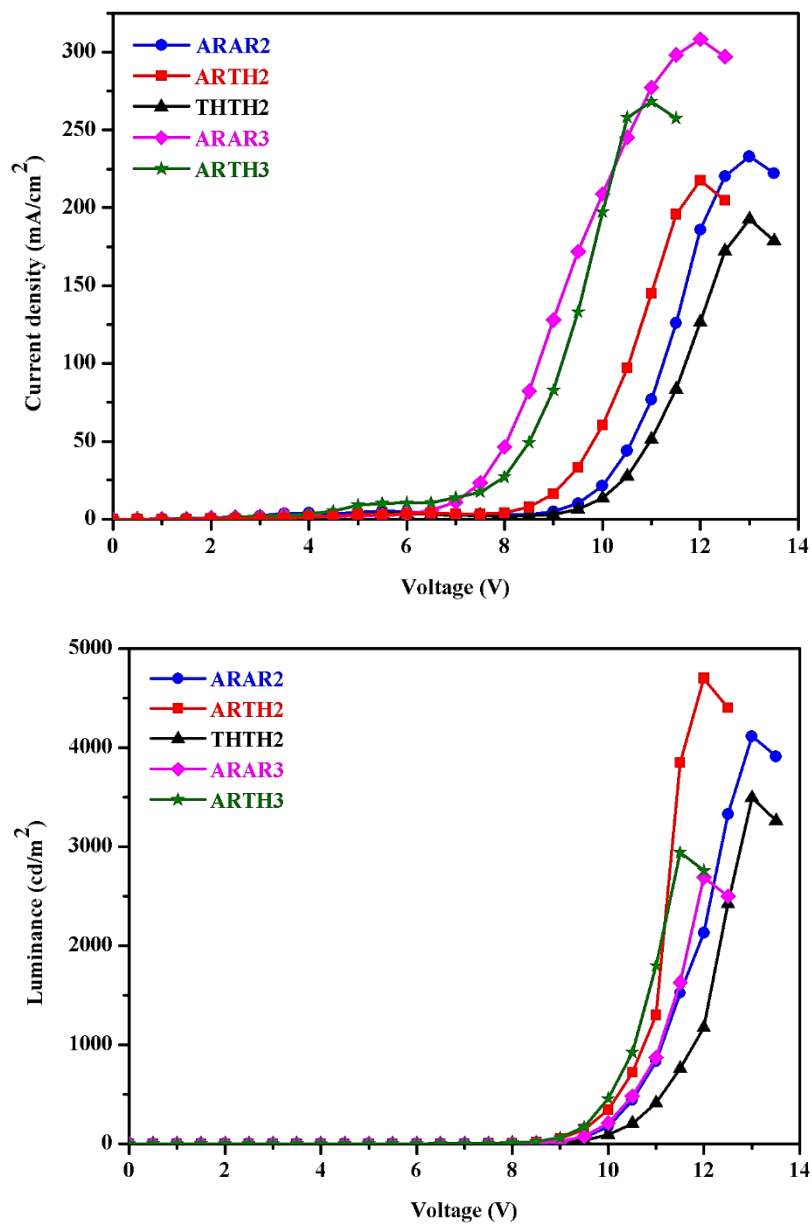


Figure 4.22 Current density and luminance versus applied bias voltage of the device structure ITO/NPB(30nm)/MADN: Dopant(20 %wt, 40nm)/Bphen (30nm)/LiF(0.5nm)/Al(100nm)

Table 4.7 Summary of OLEDs performances of target compounds with configuration of ITO/NPB(30nm)/MADN: Dopant(20 %wt, 40nm)/Bphen(30nm)/LiF (0.5nm)/Al(100nm)

Compound	CE ^a (cd/A)	PE ^b (lm/W)	L ^c (cd/m ²)	V _{turn on} ^d (V)	CIE ^e (x, y)
ARAR2	2.09	0.57	4,114	7.3	(0.36, 0.52)
ARTH2	2.71	0.79	4,699	6.3	(0.30, 0.48)
THTH2	1.36	0.33	3,492	6.5	(0.32, 0.49)
ARAR3	1.85	0.29	2,670	8.7	(0.28, 0.45)
ARTH3	2.28	0.43	2,941	7.5	(0.39, 0.47)

^aMaximum current efficiency, ^bMaximum power efficiency, ^cMaximum luminance, ^dTurn-on voltage and ^eInternational Commission on Illumination (CIE)

From Table 4.7, it was found that the best device can be achieved from **ARTH2** at turn on voltage of 6.3 V which showed maximum luminance at 4,699 cd/m², maximum current and power efficiencies of 2.71 cd/A and 0.79 Lm/W, respectively. From this result, it can be concluded that by matching of the HOMO and LUMO energy levels affect to an excellent electron and hole transporting for their device (Figure 4.23).

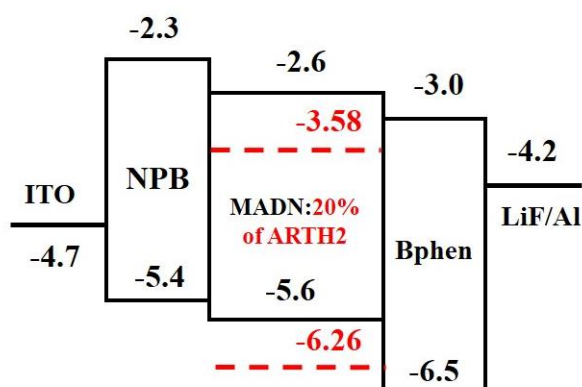


Figure 4.23 The relative HOMO and LUMO energy levels of ARTH2 device

The CIE coordinates of **ARAR2**, **ARTH2**, **THTH2**, **ARAR3**, and **ARTH3** were (0.36, 0.52), (0.30, 0.48), (0.32, 0.49), (0.28, 0.45) and (0.39, 0.47), respectively. Which are exhibited the emission in range of yellow green and yellowish green colour, as shown in the Figure 4.24.

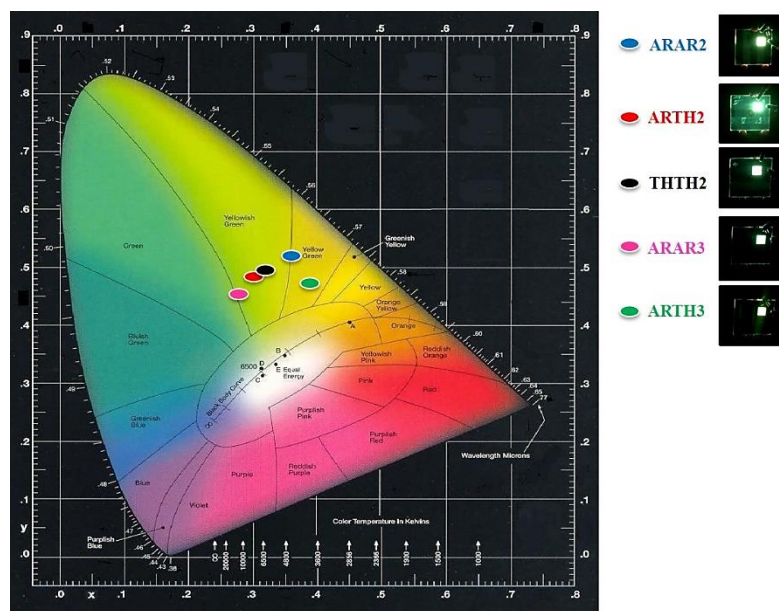


Figure 4.24 CIE coordinates and emission colour for OLED devices of target compounds

4.7 OFET performances

All five compounds were applied as a semiconductor property in OFETs with a bottom-gate-top-contact configuration which is shown in Figure 4.25. We optimized the OFETs device performances under conditions of the thin film substrate thermal evaporation at 80 °C with rate 0.1 Å/s at thickness 30 nm by using pentacene as an external standard.

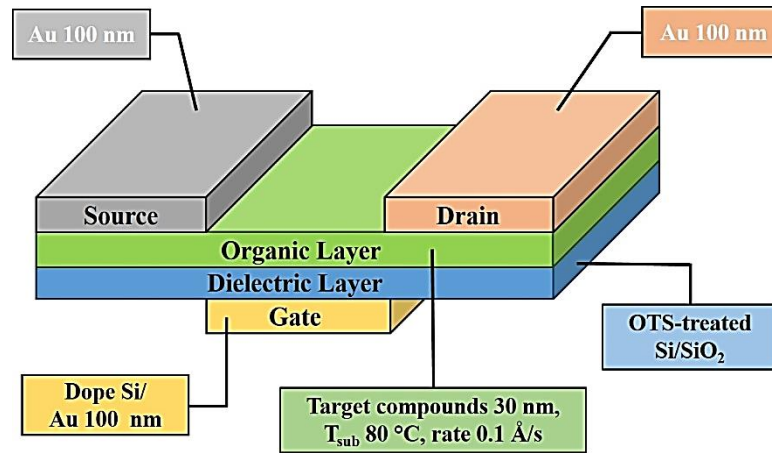


Figure 4.25 OFETs device configuration in this work

With condition in hand, we observed that only pentacene and **THTH2** devices were exhibited p-type organic semiconductor with the transfer and output characteristics which are shown in Figure 4.26 and Figure 4.27.

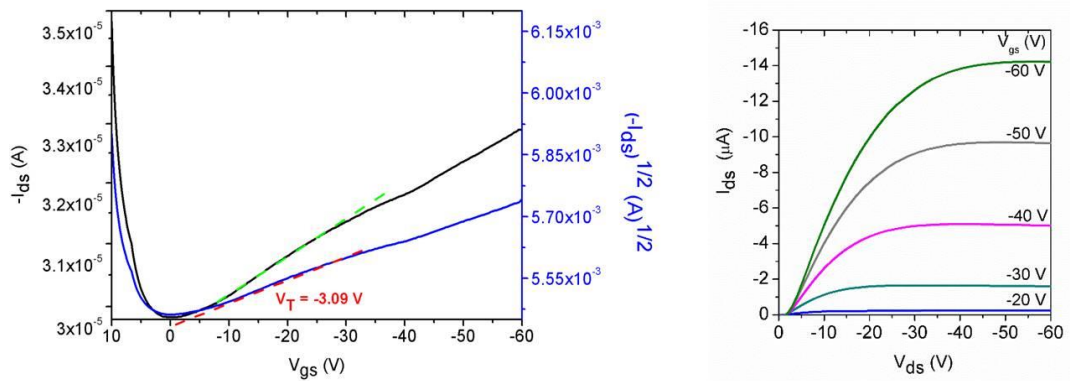


Figure 4.26 Transfer curve (left) and output curve (right) of pentacene

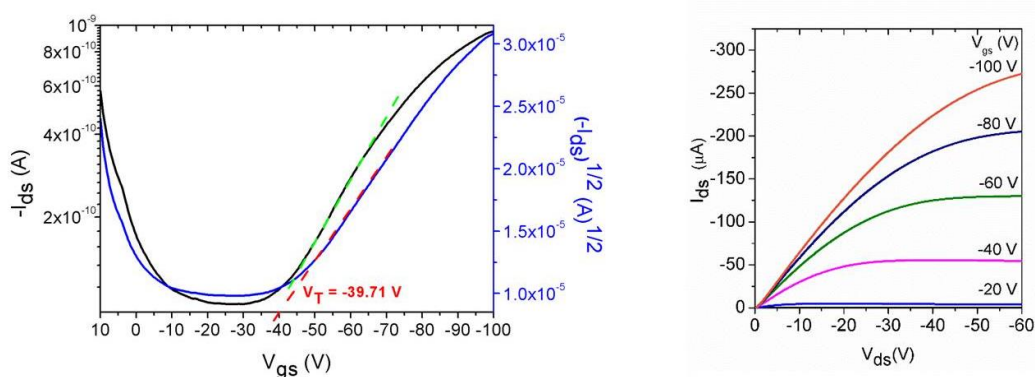


Figure 4.27 Transfer curve (left) and output curve (right) of THTH2

The mobility was calculated from the saturation region with the following equation: $\mu = (I_{DS})(2L)/(W)(C_i)(V_G - V_T)^2$, where μ is the hole mobility, I_{DS} is the drain-source current, L is the channel length ($20 \mu\text{m}$), W is the channel width ($17,000 \mu\text{m}$), C_i is the capacitance per unit area of the gate dielectric layer ($1.09 \times 10^{-8} \text{ F/cm}^2$), and V_G and V_T are the gate voltage and threshold voltage, respectively. This equation defines the important characteristics of hole mobility (μ) and threshold voltage (V_T), which could be deduced by the equation from the plot of transfer and output curves [48]. The detail for the hole mobility calculations are described in the Appendix and summarized in Table 4.8.

Table 4.8 Summary of OFETs device performances with configurations of the materials investigated in this work

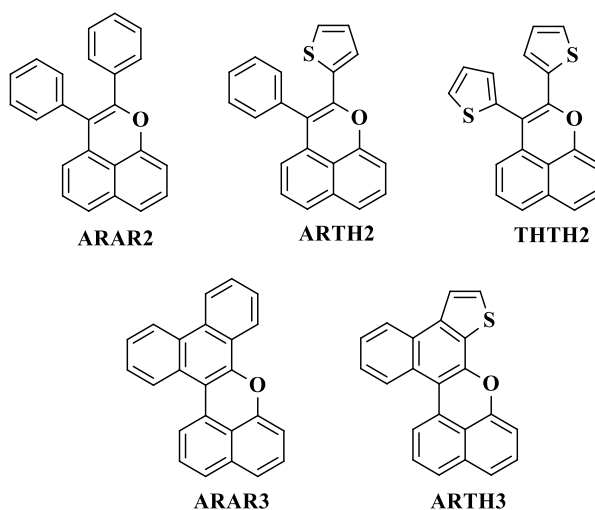
Device	Organic layer	V_{DS}^a (V)	V_{GS}^b (V)	V_T^c (V)	μ^d (cm^2/Vs)	I_{on}/I_{off}
1	Pentacene	-60	10 to -60	-3.09	9.33×10^{-4}	1.07
2	ARAR2	-60	10 to -60	-	-	-
3	ARTH2	-60	10 to -60	-	-	-
4	THTH2	-60	10 to -100	-39.71	1.64×10^{-2}	6.48
5	ARAR3	-60	10 to -60	-	-	-
6	ARTH3	-60	10 to -60	-	-	-

^aDrain-source voltage, ^bGate-source voltage, ^cThreshold voltage and ^dHole mobility

CHAPTER 5

CONCLUSIONS

We successfully synthesized and characterized a π -conjugated compounds of benzo[*d,e*]chromene (**ARAR2** and **ARAR3**) and thioarene (**ARTH2**, **ARTH3** and **THTH2**) derivatives by using Sonogashira, direct cross-coupling, ruthenium cyclization and Scholl reactions. To obtain the target molecules were **ARAR2** (73%), **ARTH2** (57%), **THTH2** (18%), **ARAR3** (75%) and **ARTH3** (32%), respectively. The molecular structures were confirmed by using NMR, FT-IR, and mass spectroscopy. In addition, **ARTH2** was confirmed the molecular isomer by COSY NMR.



The target molecules were investigated the photophysical properties. All compounds gave two main absorption bands. The strong absorption originated from the delocalized π - π^* transition at 320-365 nm of benzo[*d,e*]chromene moiety. Moreover, the spectra showed peak around 366-500 nm which was assigned to the delocalized n - π^* transition. The photoluminescence spectra gave the green emission regions which related with energy band gaps. In addition, the thermal properties were studied by thermogravimetric analysis (TGA). We found that the thioarene products (**ARTH2**, **ARTH3** and **THTH2**) showed the good thermal stabilities.

All target compounds were used as a dopant in optimized host-guest OLEDs devices with the configuration of ITO/NPB/MADN: 20 %wt of dopants/Bphen/LiF/Al. The result indicated that the **ARTH2** showed the best performance and exhibited yellowish green colour with maximum luminance at 4,699 cd/m², maximum current and maximum power efficiencies at 2.71 cd/A and 0.79 Lm/W, respectively. Moreover, the target molecules were investigated of OFETs performance. It was found that the **THTH2** showed a p-type character with hole mobility of 1.64 x 10⁻² cm²/Vs and on/off current ratio of 6.48.

REFERENCES

REFERENCES

- [1] Shaheen, S and et al. "Energy and charge transfer in organic light-emitting diodes: a soluble quinacridone study", **Journal of Applied Physics**. 85(11): 7939-7945; May, 1999.
- [2] Savvate'ev, V and et al. "Nanosecond transients in the electroluminescence from multilayer blue organic light-emitting devices based on 4, 4'-bis (2, 2' diphenyl vinyl)-1, 1'-biphenyl", **Applied Physics Letters**. 76(12): 1501-1503; March, 2000.
- [3] Kappaun, S and et al. "Phosphorescent organic light-emitting devices: Working principle and iridium based emitter materials", **International Journal of Molecular Sciences**. 9(8): 1527-1547; August, 2008.
- [4] Cleave, V and et al. "Harvesting singlet and triplet energy in polymer LEDs", **Advanced Materials**. 11(4): 285-288; April, 1999.
- [5] Lee, J. K and et al. "Thin film light emitting devices from an electroluminescent ruthenium complex", **Applied Physics Letters**. 69(12): 1686-1688; August, 1996.
- [6] Wu, K. C and et al. "The photophysical properties of dipyrrenylbenzenes and their application as exceedingly efficient blue emitters for electroluminescent devices", **Advanced Functional Materials**. 18(1): 67-75; January, 2008.
- [7] Rajamalli, P and et al. "A new molecular design based on thermally activated delayed fluorescence for highly efficient organic light emitting diodes", **Journal of the American Chemical Society**. 138(2); January, 2016.
- [8] Tang, C. W and et al. "Organic electroluminescent diodes", **Applied Physics Letters**. 51(12): 913-915; June, 1987.
- [9] Baldo, M and et al. "Very high-efficiency green organic light-emitting devices based on electrophosphorescence", **Applied Physics Letters**. 75(1): 4-6; June, 1999.
- [10] Lendino, J and et al. "OLED technology", **The development of OLED displays**. <https://www.extremetech.com>. November, 2018.

REFERENCES (CONTINUED)

- [11] Steve, J and et al. “OLED technology”, **The development of OLED displays**.
<https://www.apple.com>. November, 2018.
- [12] Geffroy, B and et al. “Organic light-emitting diode (OLED) technology: materials, devices and display technologies”, **Polymer International**.
55(6): 572-582; February, 2006.
- [13] Kim, D.-H and et al. “Novel Green Small-molecule Host Materials for Solution-processed Organic Light-emitting Diodes”, **Chemistry Letters**. 37(11):
1150-1151; August, 2008.
- [14] Zimmermann, J and et al. “A generalization of the Jablonski diagram to account for polarization and anisotropy effects in time-resolved experiments”,
Physical Chemistry Chemical Physics. 5(14): 2964-2969; January, 2003.
- [15] Jablonski, A and et al. “Efficiency of anti-Stokes fluorescence in dyes”, **Nature**.
131(3319): 839; June, 1933.
- [16] Thoms, T and et al. “Improved host material design for phosphorescent guest-host systems”, **Thin Solid Films**. 436(2): 264-268; July, 2003.
- [17] Marcus, R. A and et al. “On the theory of oxidation-reduction reactions involving electron transfer. I”, **The Journal of Chemical Physics**. 24(5): 966-978;
December, 2004.
- [18] VanSlyke, S. A and et al. **Electroluminescent device with organic luminescent medium**. Google Patents, 1988.
- [19] Robert, L and et al. “OFET technology”, **The development of OFET displays**.
www.cstf.kyushu-u.ac.jp. November, 2018.
- [20] Prat, C and et al. “OFET technology”, **The development of OFET displays**.
<https://www.photonics.com>. November, 2018.
- [21] Kymissis, I and et al. “A lithographic process for integrated organic field-effect transistors”, **Journal of Display Technology**. 1(2): 289-294; December,
2005.

REFERENCES (CONTINUED)

- [22] Allard, S and et al. “Organic semiconductors for solution-processable field-effect transistors (OFETs)”, **Angewandte Chemie International Edition**. 47(22): 4070-4098; May, 2008.
- [23] Ryu, K and et al. **Characterization of organic field effect transistors for OLED displays**. Massachusetts: Institute of Technology, 2005.
- [24] Yan, K and et al. “Iridium-Catalyzed Tandem Cyclization of Benzoylacetonitriles with Diazo Compounds Leading to Substituted Naphtho [*1, 8-bc*] pyrans by Sequential C-H Functionalization”, **Advanced Synthesis & Catalysis**. 360(12): 2272-2279; April, 2018.
- [25] Wang, M and et al. “Naphthoquinone-Directed C-H Annulation and Csp³-H Bond Cleavage: One-Pot Synthesis of Tetracyclic Naphthoxazoles”, **The Journal of Organic Chemistry**. 79(10): 4553-4560; April, 2014.
- [26] Mochida, S and et al. “Synthesis of Naphtho [*1, 8-bc*] pyran Derivatives and Related Compounds through Hydroxy Group Directed C-H Bond Cleavage under Rhodium Catalysis”, **Chemistry an Asian Journal**. 5(4): 847-851; March, 2010.
- [27] Tan, X and et al. “Rhodium-Catalyzed Cascade Oxidative Annulation Leading to Substituted Naphtho [*1, 8-bc*] pyrans by Sequential Cleavage of C (sp²)-H/C (sp³)-H and C (sp²)-H/O-H Bonds”, **Journal of the American Chemical Society**. 134(39): 16163-16166; October, 2012.
- [28] Xie, H-T and et al. “Construction of the oxaphenalene skeletons of mansonone F derivatives through C-H bond functionalization and their evaluation for anti-proliferative activities”, **RSC Advances**. 7(34): 20919-20918; April, 2017.
- [29] Thirunavukkarasu, V.S and et al. “Hydroxyl-Directed Ruthenium-Catalyzed C-H Bond Functionalization: Versatile Access to Fluorescent Pyrans”, **Organic Letters**. 14(13): 3416-3419; September, 2012.

REFERENCES (CONTINUED)

- [30] Shimizu, M and et al. "Rhodium-Catalyzed Oxidative Coupling between Salicylaldehydes and Internal Alkynes with C-H Bond Cleavage to Produce 2, 3-Disubstituted Chromones", **Chemistry an Asian Journal**. 3(5): 881-886; April, 2008.
- [31] Somchob, B and et al. "A Novel Benzo [*d, e*] Chromene for Organic Light Emitting Diodes (OLEDs)", **Paper Presented at the Applied Mechanics and Materials**. 876: 71-75; February, 2018.
- [32] Grzybowski, M and et al. "Comparison of oxidative aromatic coupling and the Scholl reaction", **Angewandte Chemie International Edition**. 52(38): 9900-9930; July, 2013.
- [33] Benschafut, R and et al. "An unusual charge umpolung: synthesis of the bay region diketone 2, 3: 10, 11-dibenzoperylene-1, 12-dione", **The Journal of Organic Chemistry**. 64(2): 644-647; December, 1998.
- [34] Larsen, J and et al. "Direct Oxidative Cyclization of 1, 2-Bis (benzothiophene-2-yl) ethylenes as a Replacement of Photocyclization in the Synthesis of Thiaheterohelicenes", **The Journal of Organic Chemistry**. 61(3): 1151-1151; February, 1996.
- [35] Wang, J and et al. "New fused heteroarenes for high-performance field-effect transistors", **Chemistry of Materials**. 21(13): 2595-2597; May, 2009.
- [36] Krzeszewski, M and et al. "Color-Tunable Fluorescent Dyes Based on Benzo [*c*] coumarin", **European Journal of Organic Chemistry**. 2013(25): 5631-5644; July, 2013.
- [37] Liu, W.-J and et al. "Thin Film Organic Transistors from Air-Stable Heteroarenes: Anthra [*1, 2-b*: 4, 3-*b'*: 5, 6-*b''*: 8, 7-*b'''*] tetrathiophene Derivatives", **Organic Letters**. 9(21): 4187-4190; September, 2007.
- [38] Laquindanum, J. G and et al. "Synthesis, morphology, and field-effect mobility of anthradithiophenes", **Journal of the American Chemical Society**. 120(4): 664-672; January, 1998.

REFERENCES (CONTINUED)

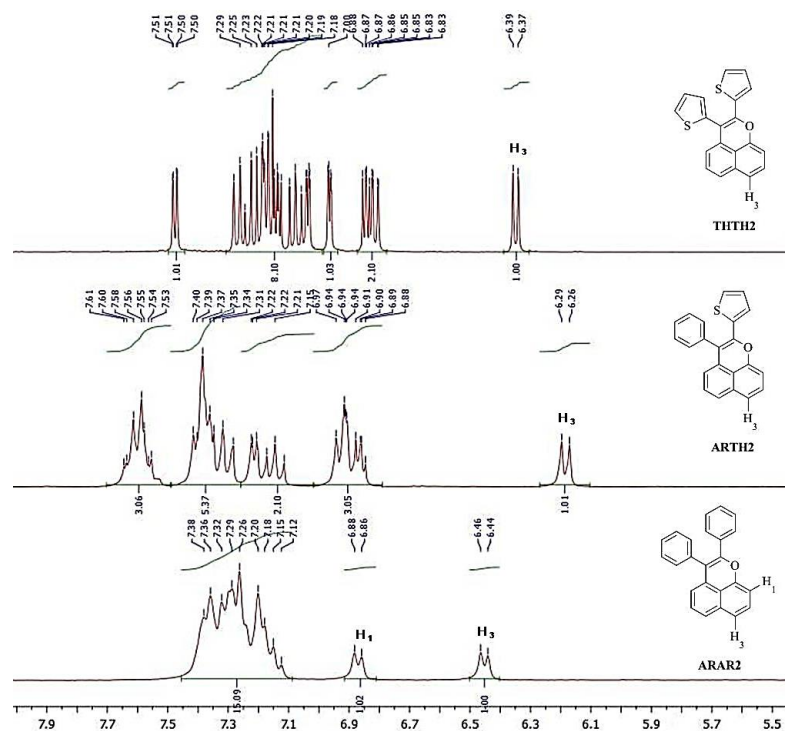
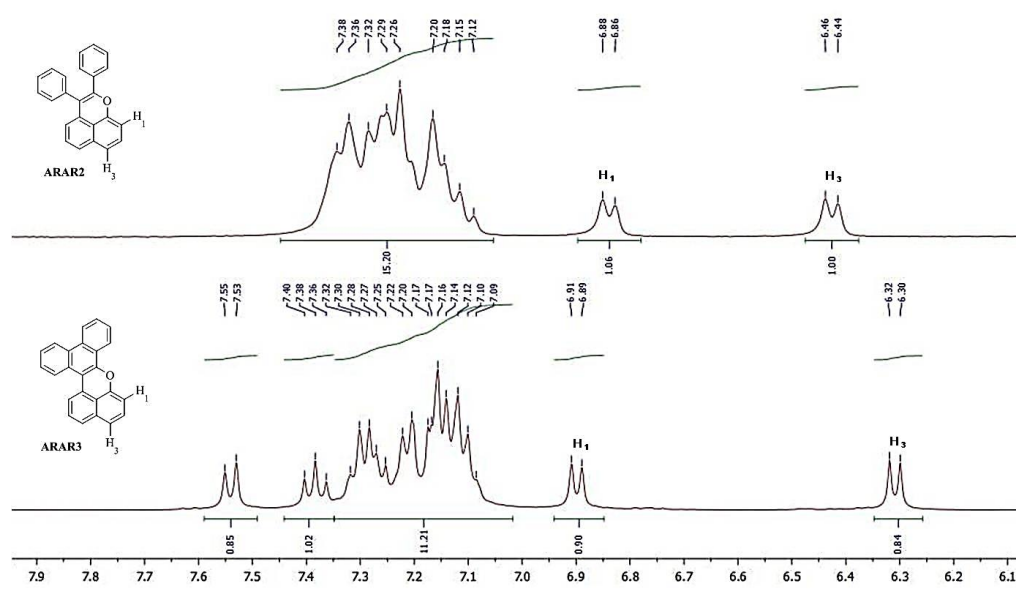
- [39] Sun, Y and et al. “High-performance and stable organic thin-film transistors based on fused thiophenes”, **Advanced Functional Materials**. 16(3): 426-432; December, 2005.
- [40] Takimiya, K and et al. “2, 7-Diphenyl [1] benzothieno [3, 2-*b*] benzothiophene, a new organic semiconductor for air-stable organic field-effect transistors with mobilities up to $2.0 \text{ cm}^2 \text{ V}^{-1} \text{ s}^{-1}$ ”, **Journal of the American Chemical Society**. 128(39): 12604-12605; September, 2006.
- [41] Yamamoto, T and et al. “Facile Synthesis of Highly π -Extended Heteroarenes, Dinaphtho[2, 3-*b*: 2', 3'-*f*]chalcogenopheno[3, 2-*b*]chalcogenophenes, and Their Application to Field-Effect Transistors”, **Journal of the American Chemical Society**. 129: 2224-2225; February, 2007.
- [42] Thathong, Y. **The synthesis and characterization of ruthenium complexes for dye sensitized solar cells application**. Master's Thesis: Ubon Ratchathani University, 2013.
- [43] Coulson, D.-R and et al. “Tetrakis (triphenylphosphine) palladium (0)”, **Inorganic Syntheses**. 13: 121-124; January, 2007.
- [44] Wöhrle, T and et al. “Pushing steric bias in the Scholl reaction to access liquid crystalline crown ethers”, **The Journal of Organic Chemistry**. 79(21): 10143-10152; October, 2014.
- [45] Zhao, K and et al. “Design of Janus triphenylene mesogens: facile synthesis, mesomorphism, photoluminescence, and semiconductivity”, **Dyes and Pigments**. 143: 252-260; August, 2017.
- [46] Koseki, Y and et al. “Silver salt-promoted direct cross-coupling reactions of alkynylsilanes with aryl iodides: synthesis of aryl-substituted alkynylamides”, **Tetrahedron Letters**. 41(14): 2377-2380; April, 2000.
- [47] Dong, Y and et al. “Aggregation-induced emissions of tetraphenylethene derivatives and their utilities as chemical vapor sensors and in organic light-emitting diodes”, **Applied Physics Letters**. 91(1): 011111; July, 2007.

REFERENCES (CONTINUED)

- [48] Generali, G and et al. “Correlation among morphology, crystallinity, and charge mobility in OFETs made of quaterthiophene alkyl derivatives on a transparent substrate platform”, **The Journal of Physical Chemistry C**. 115(46): 23164-13169; October, 2011.

APPENDICES

APPENDIX A
Characterization data

1. ^1H and ^{13}C NMR spectraFigure A.1 ^1H NMR in CDCl_3 and the assignment of ARAR2, ARTH2 and THTH2Figure A.2 ^1H NMR in CDCl_3 and the assignment of ARAR2 and ARAR3

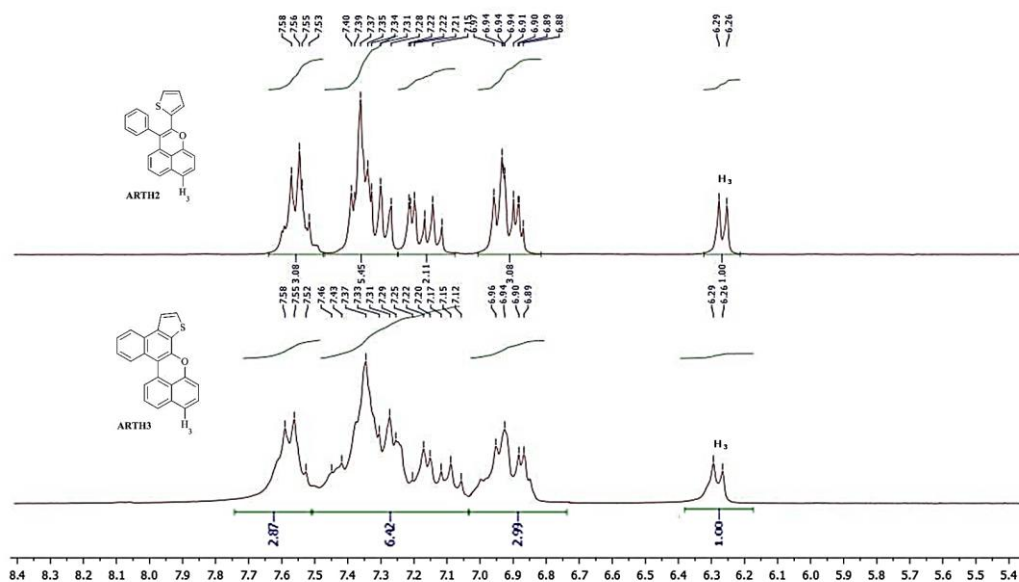


Figure A.3 ^1H NMR in CDCl_3 and the assignment of ARTH2 and ARTH3

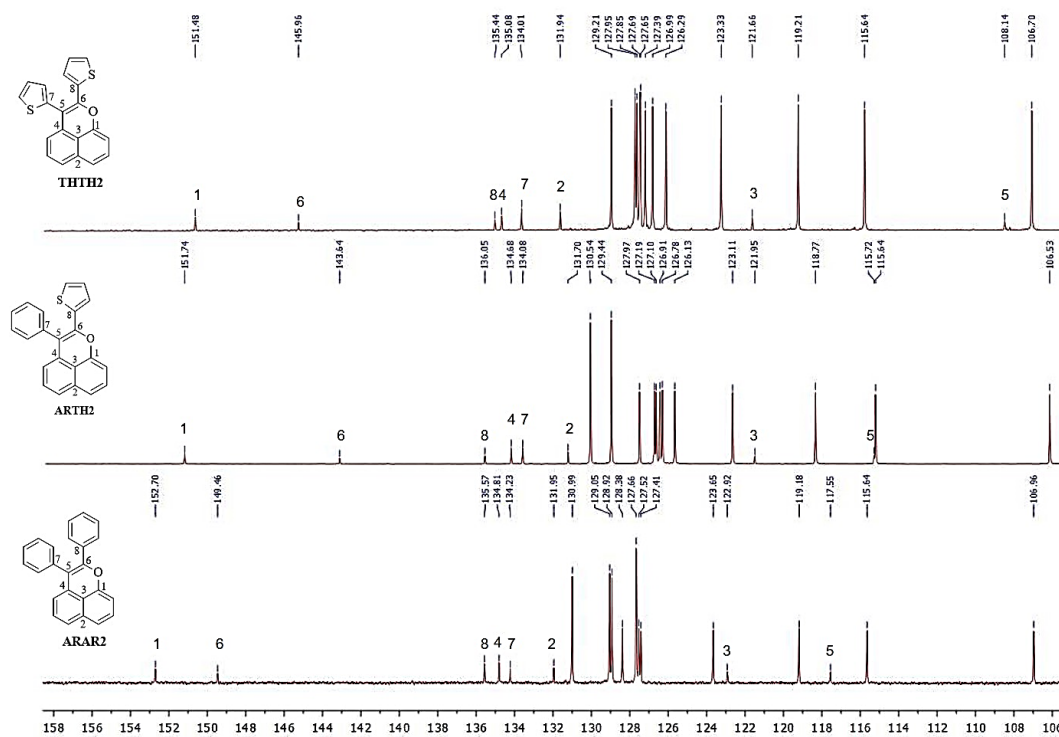


Figure A.4 ^{13}C NMR in CDCl_3 and the assignment of ARAR2, ARTH2 and THTH2

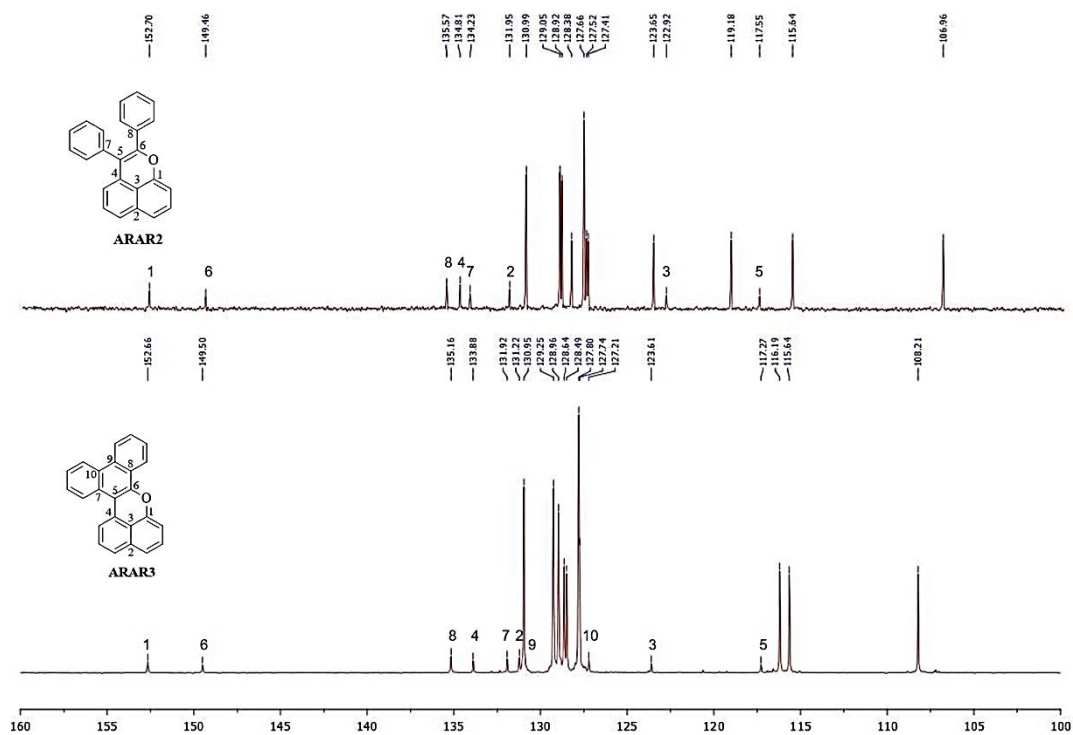


Figure A.5 ^{13}C NMR in CDCl_3 and the assignment of ARAR2 and ARAR3

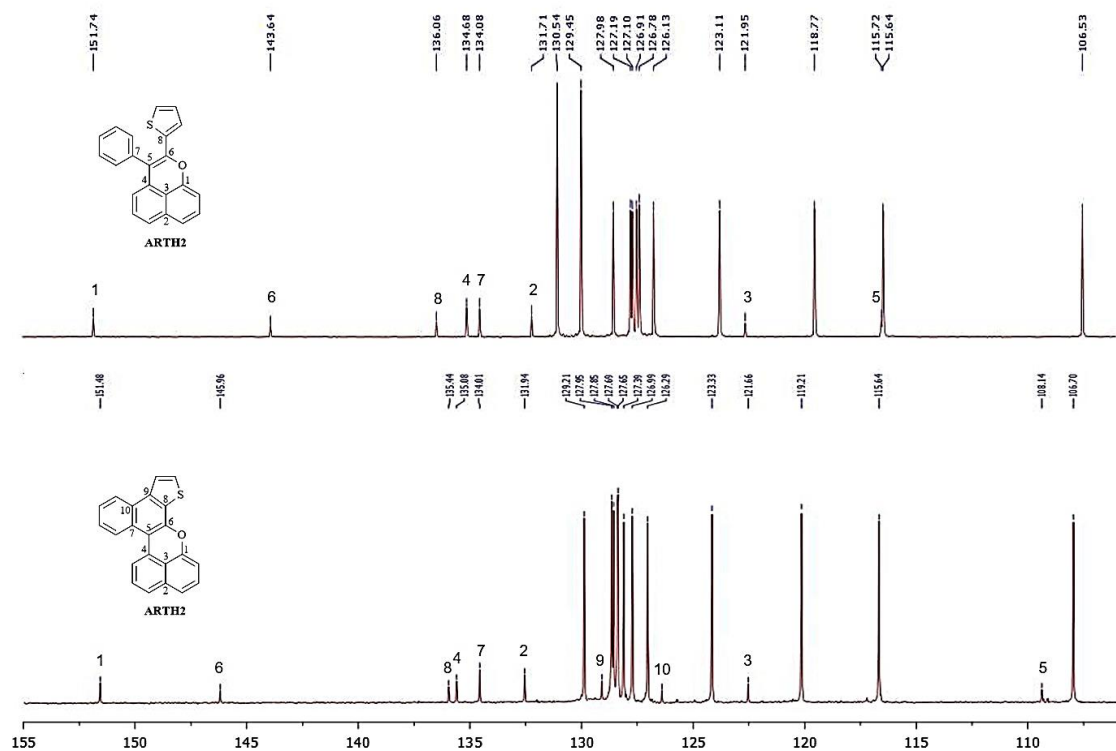


Figure A.6 ^{13}C NMR in CDCl_3 and the assignment of ARTH2 and ARTH3

2. Mass spectra

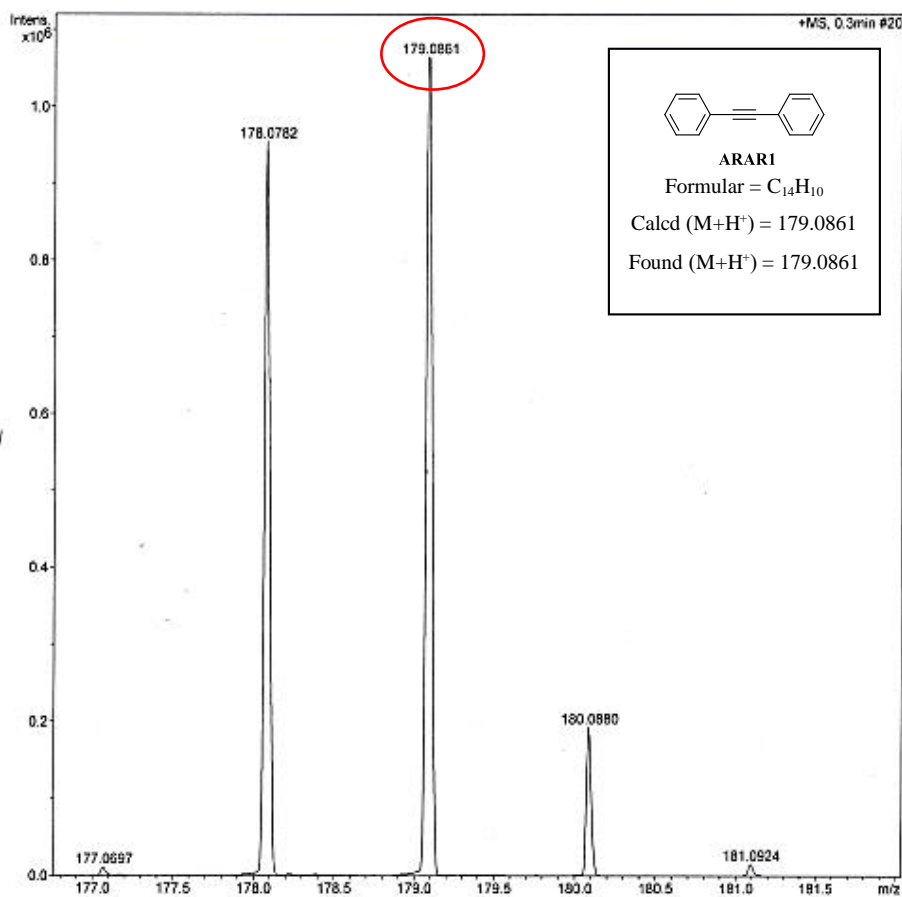


Figure A.7 Mass spectra and the assignment of ARAR1

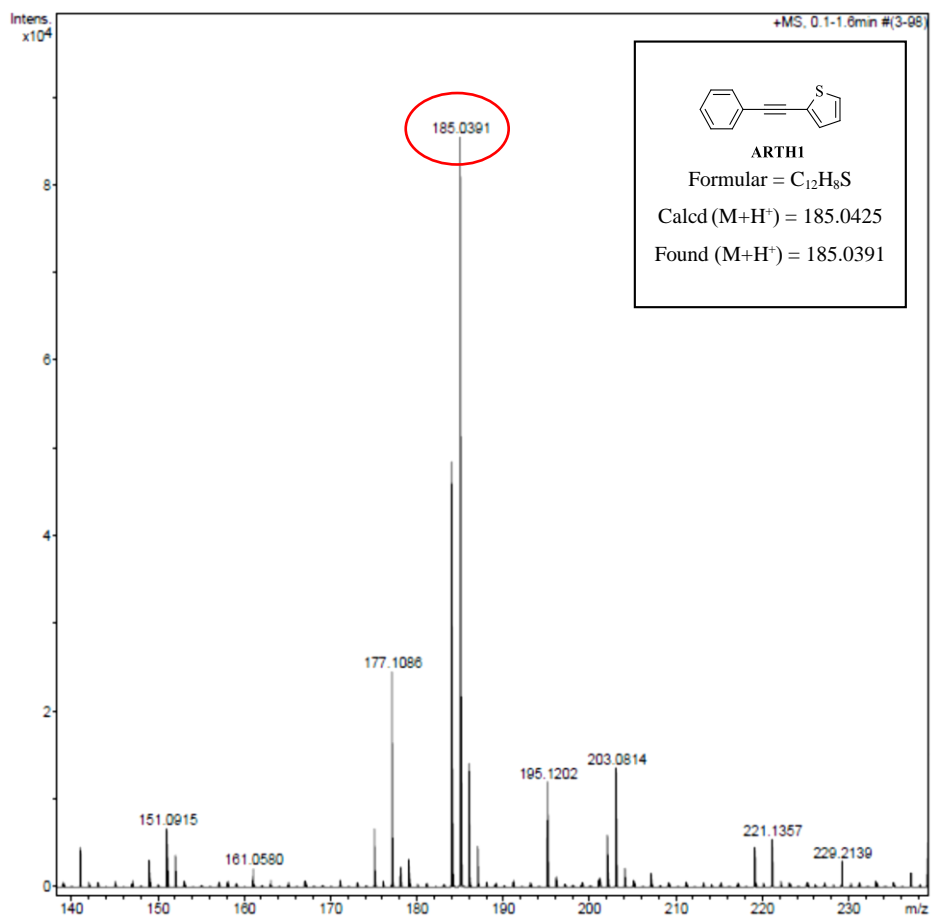


Figure A.8 Mass spectra and the assignment of ARTH1

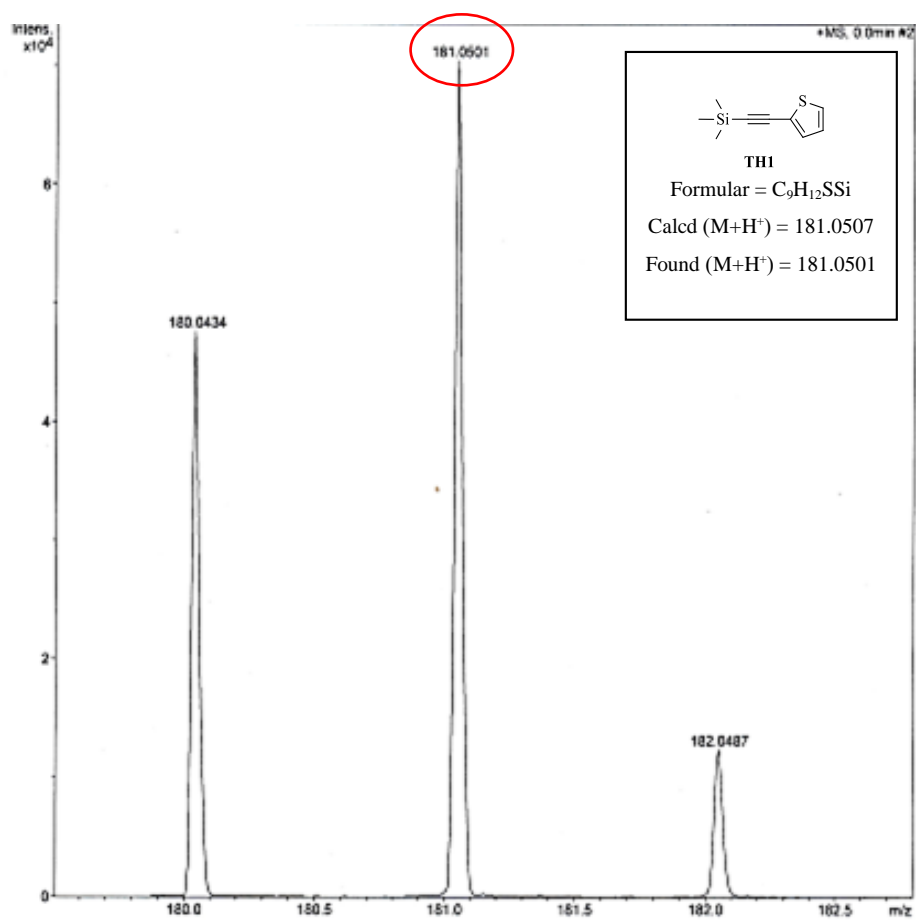


Figure A.9 Mass spectra and the assignment of TH1

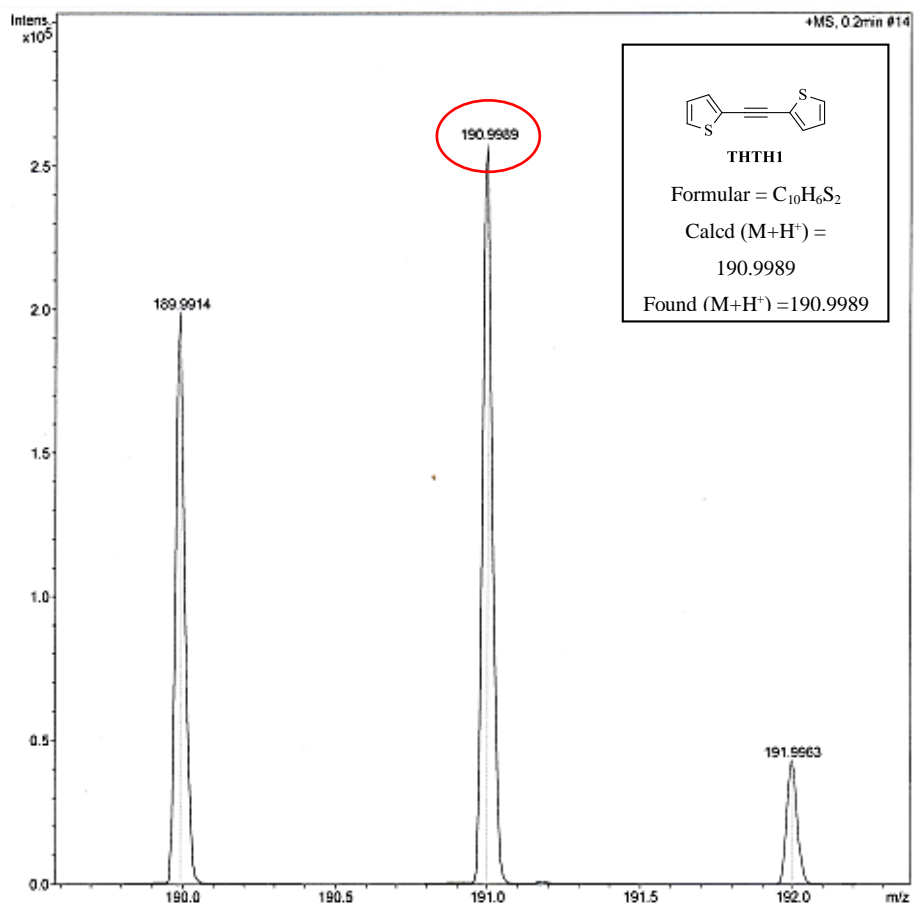


Figure A.10 Mass spectra and the assignment of THTH1

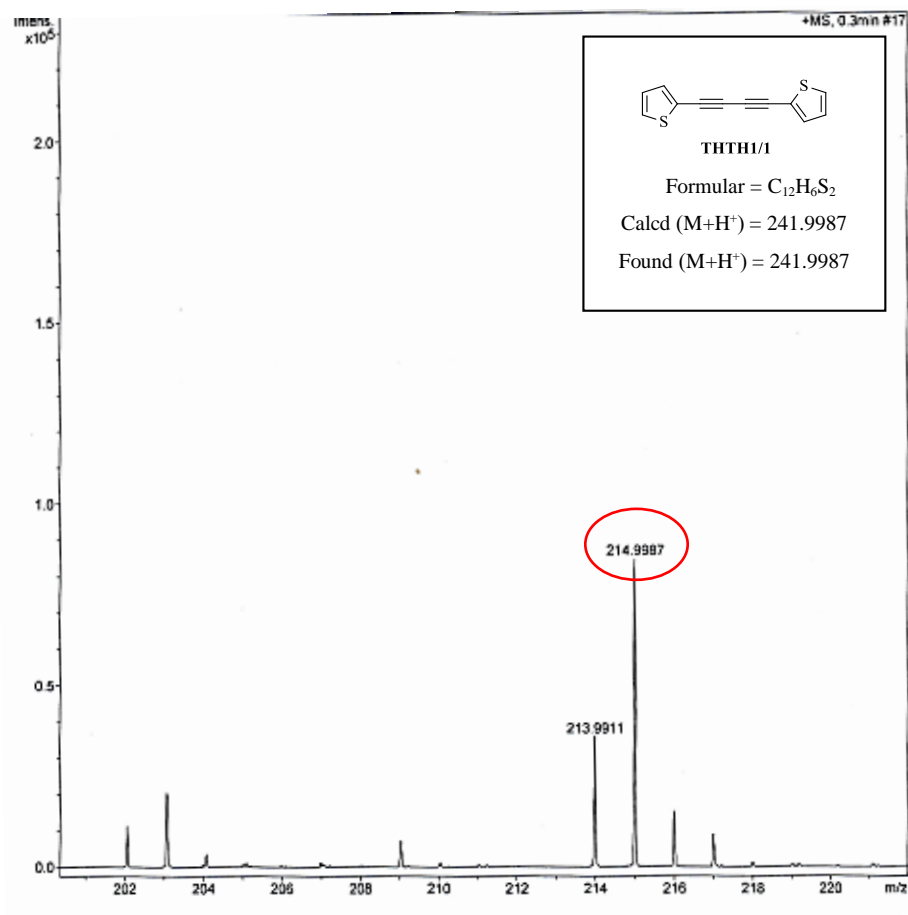


Figure A.11 Mass spectra and the assignment of THTH1/1

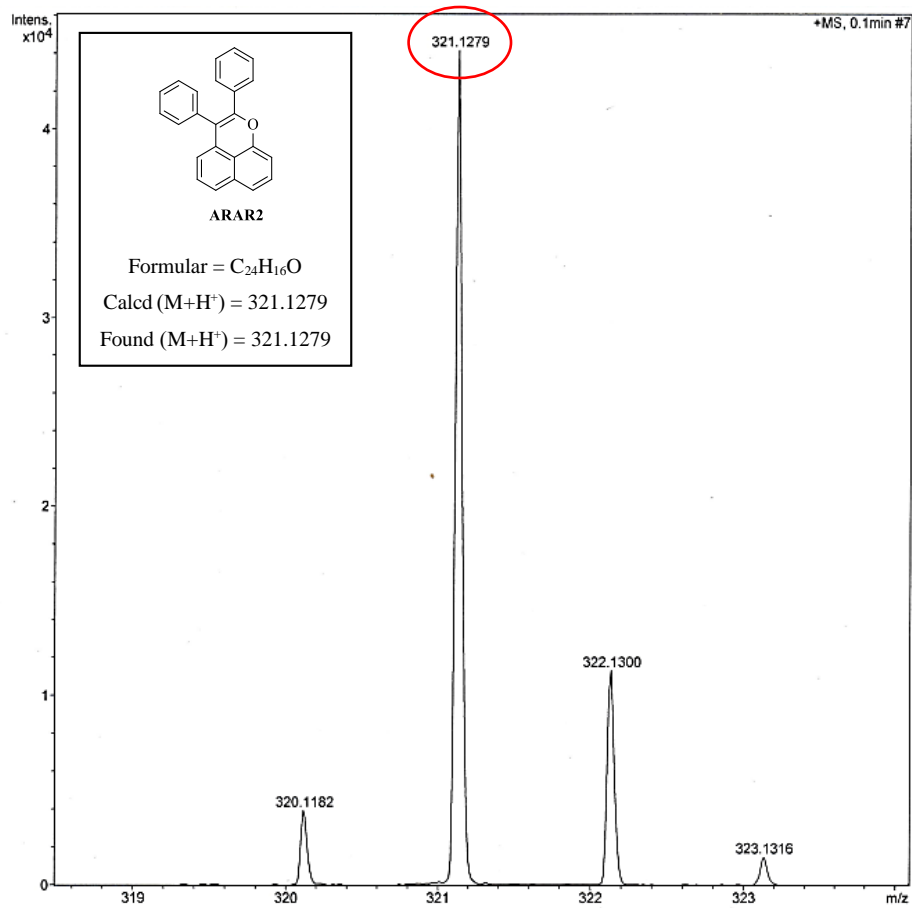


Figure A.12 Mass spectra and the assignment of ARAR2

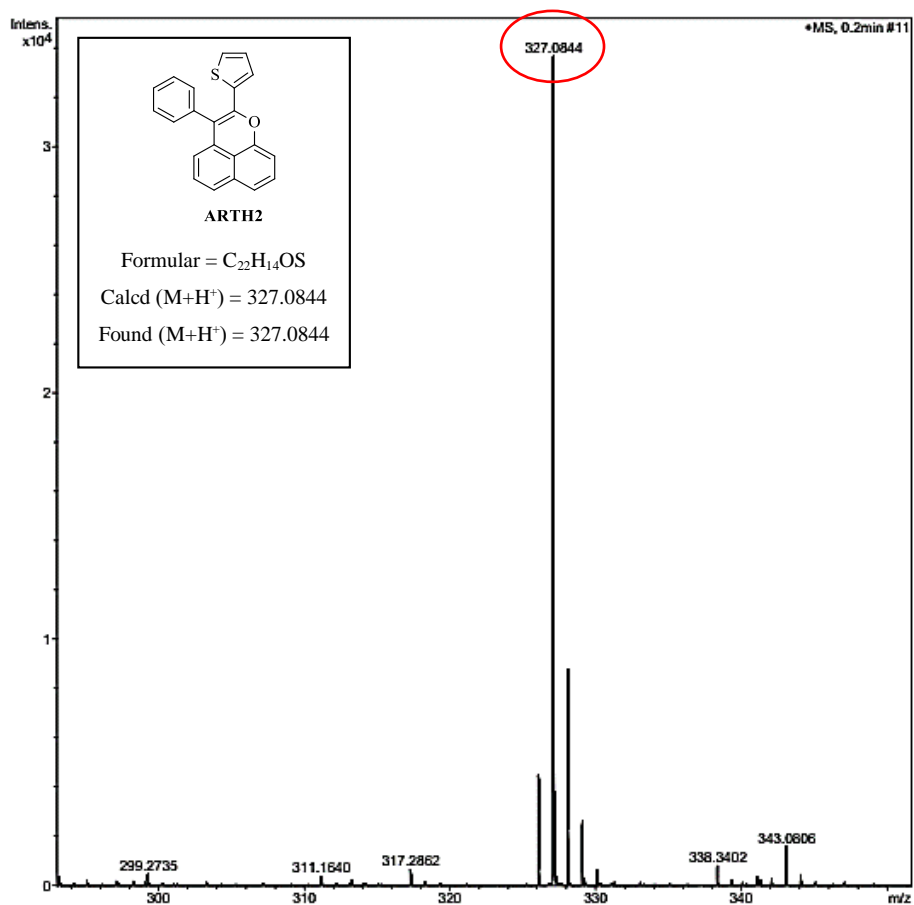


Figure A.13 Mass spectra and the assignment of ARTH2

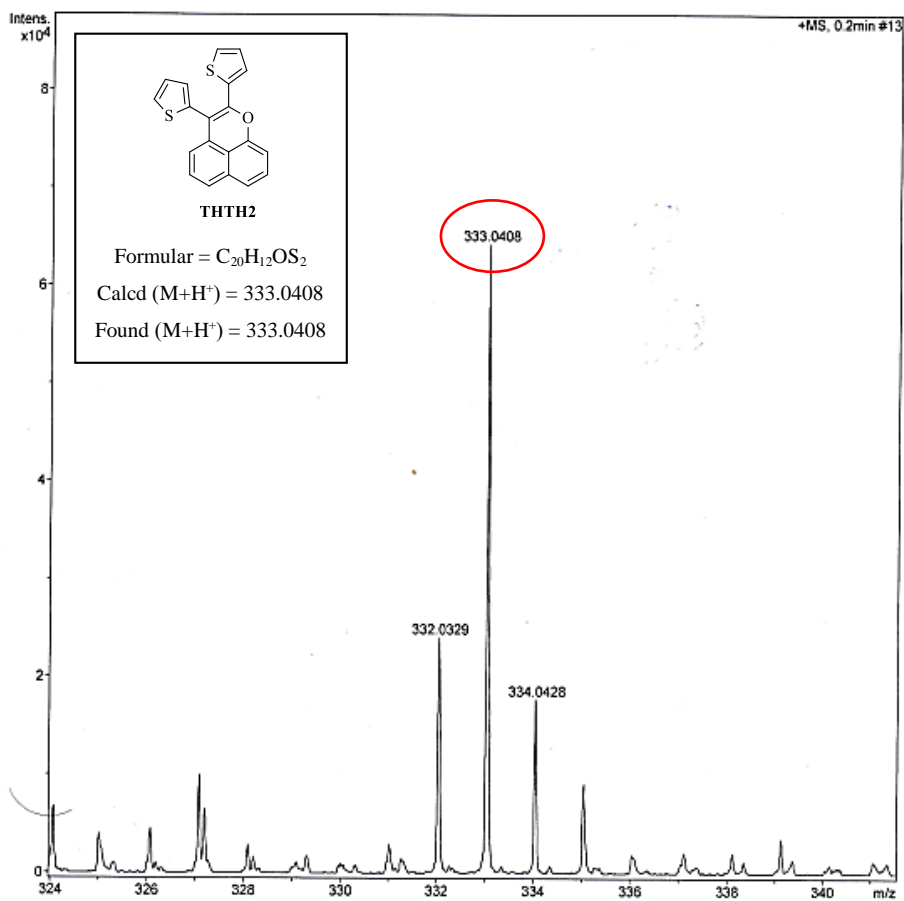


Figure A.14 Mass spectra and the assignment of THTH2

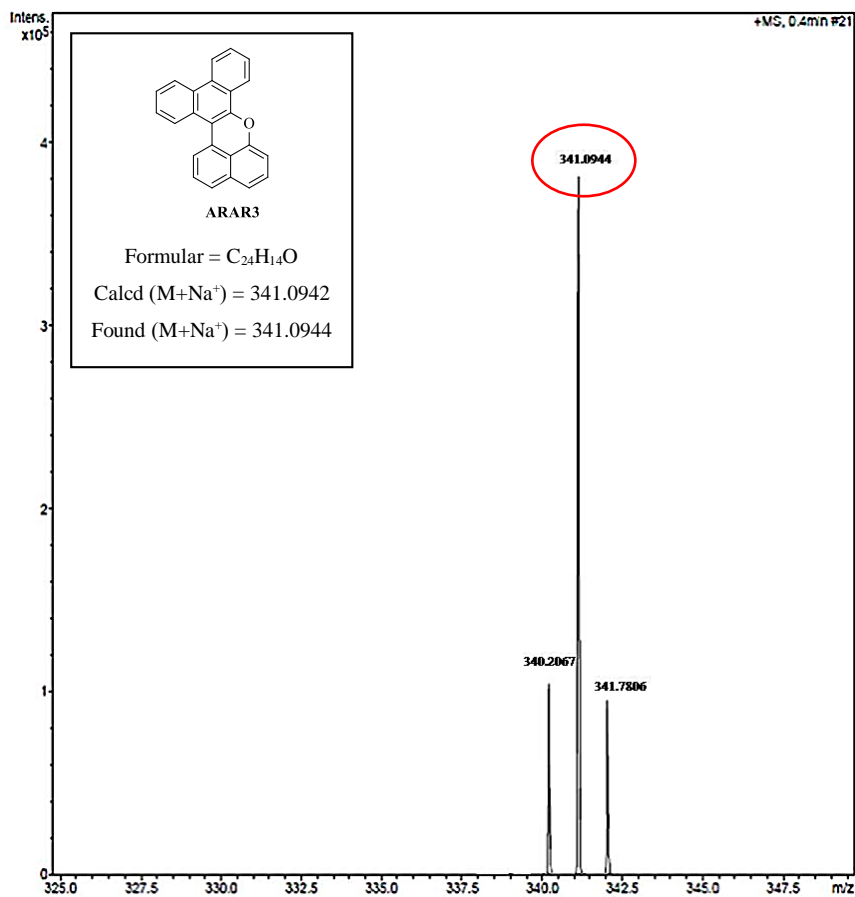


Figure A.15 Mass spectra and the assignment of ARAR3

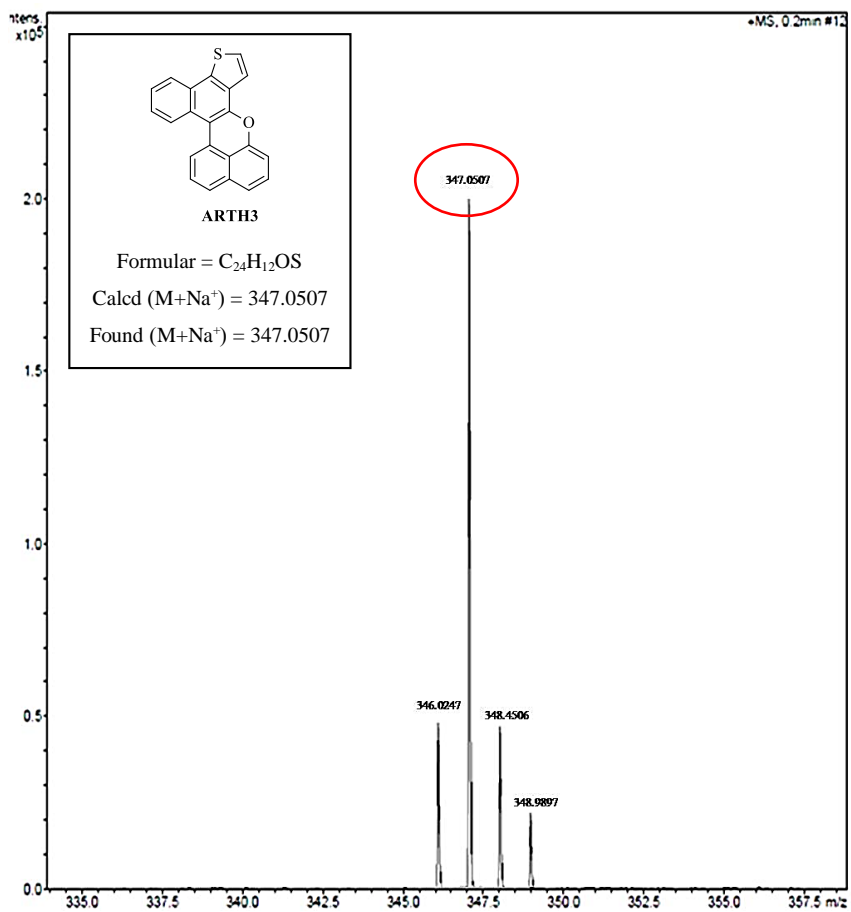


Figure A.16 Mass spectra and the assignment of ARTH3

3. FT-IR spectra

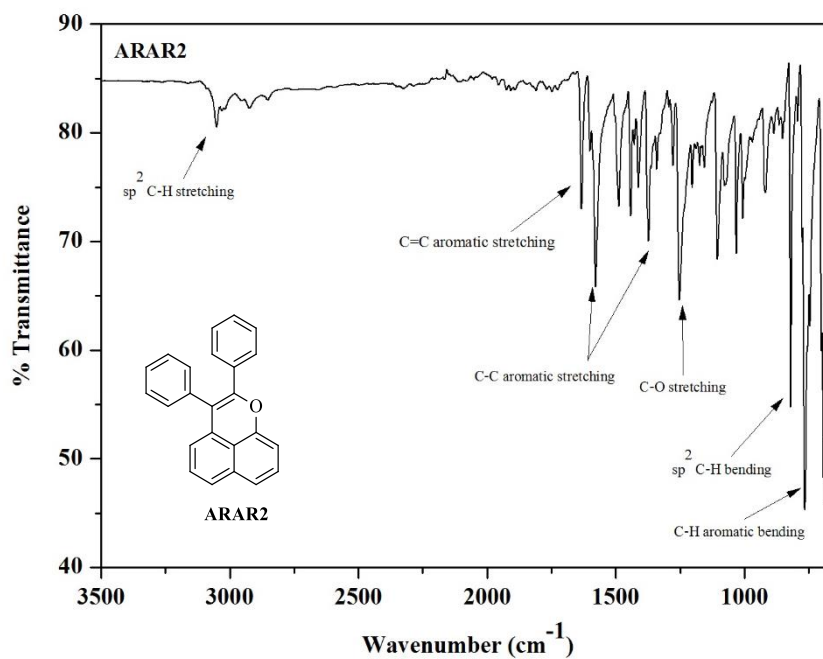


Figure A.17 FT-IR spectra and the assignment of ARAR2

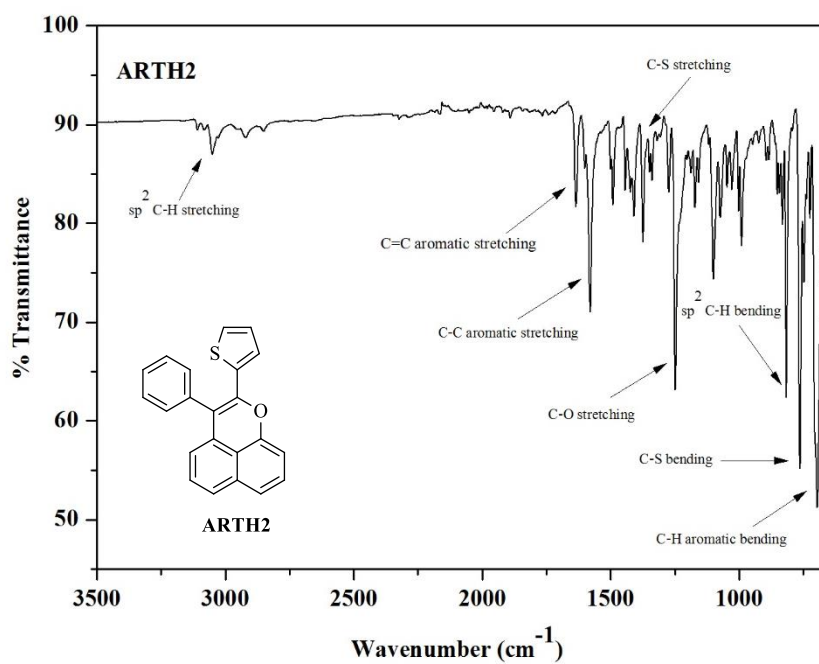


Figure A.18 FT-IR spectra and the assignment of ARTH2

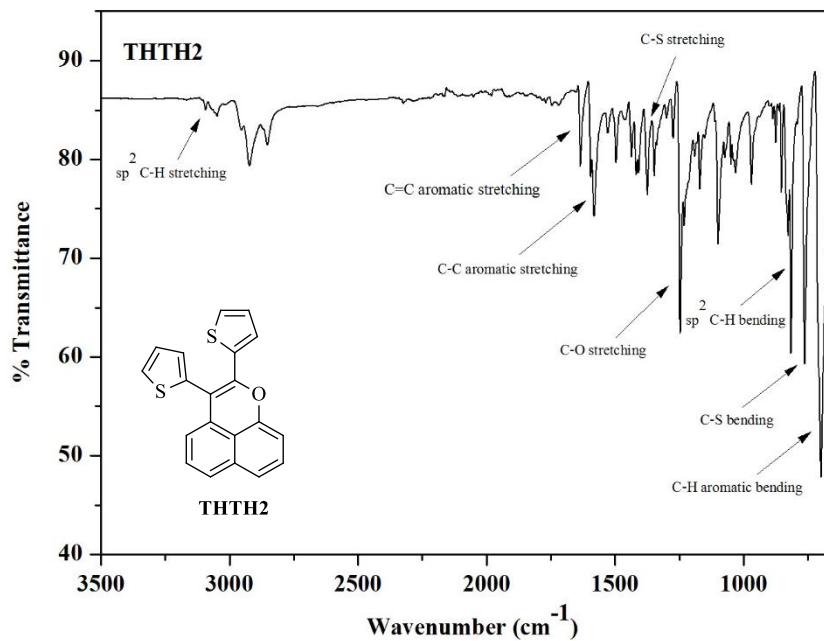


Figure A.19 FT-IR spectra and the assignment of THTH2

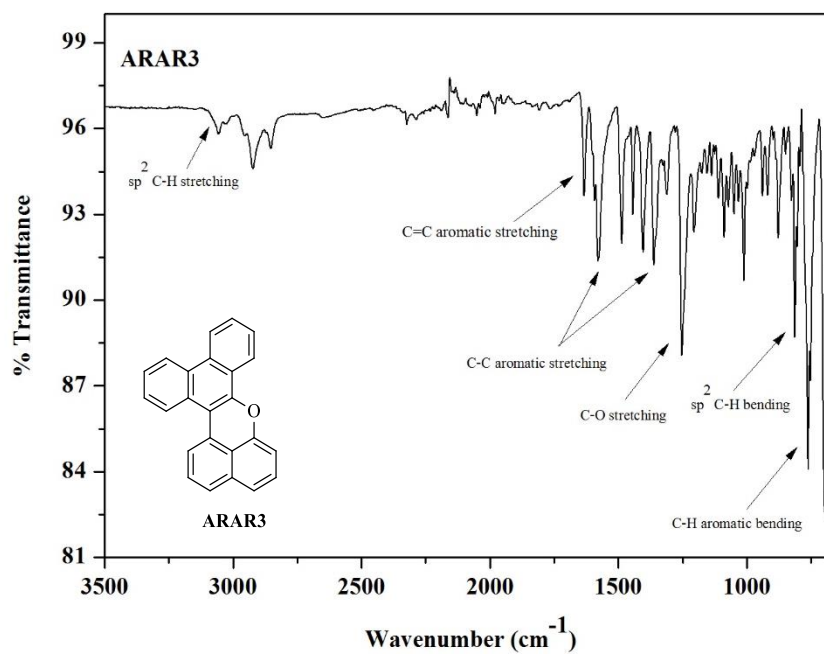


Figure A.20 FT-IR spectra and the assignment of ARAR3

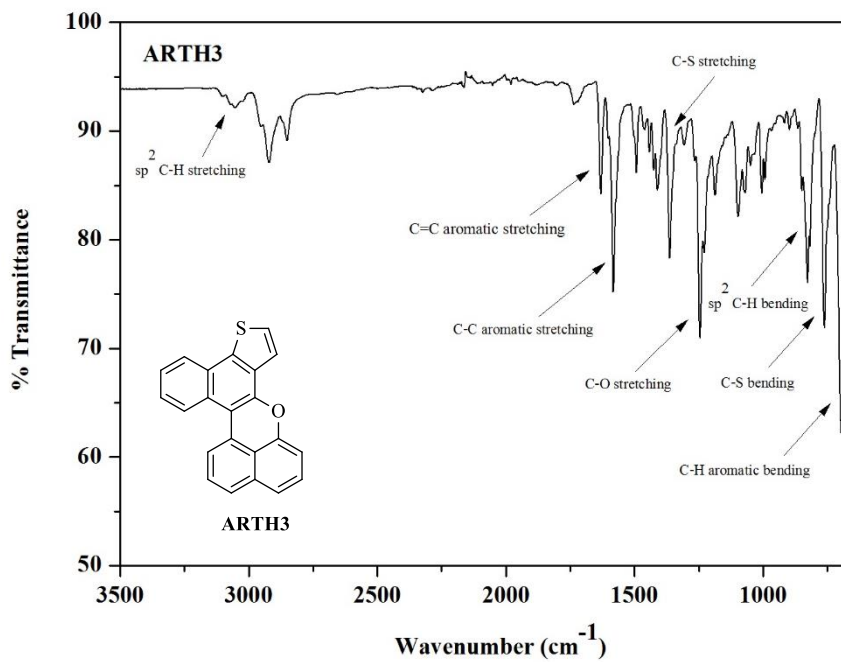


Figure A.21 FT-IR spectra and the assignment of ARTH3

APPENDIX B
Photophysical and electrochemical data

1. Photophysical data calculation

The onset absorption wavelength (λ_{onset}) of UV-Visible spectrum could be used to calculate the energy gap (E_g) of material. The value of λ_{onset} can be obtained from λ at 1% absorption of absorption at the longest absorption wavelength (λ_{abs}). From Bohr-Einstein equation, the energy gap could be derived as shown in equation below.

$$E_g(eV) = \frac{hc}{\lambda_{onset}(nm) \times 10^{-9}} \times \frac{1}{1.6 \times 10^{-19}} \cong \frac{1240}{\lambda_{onset}(nm)}$$

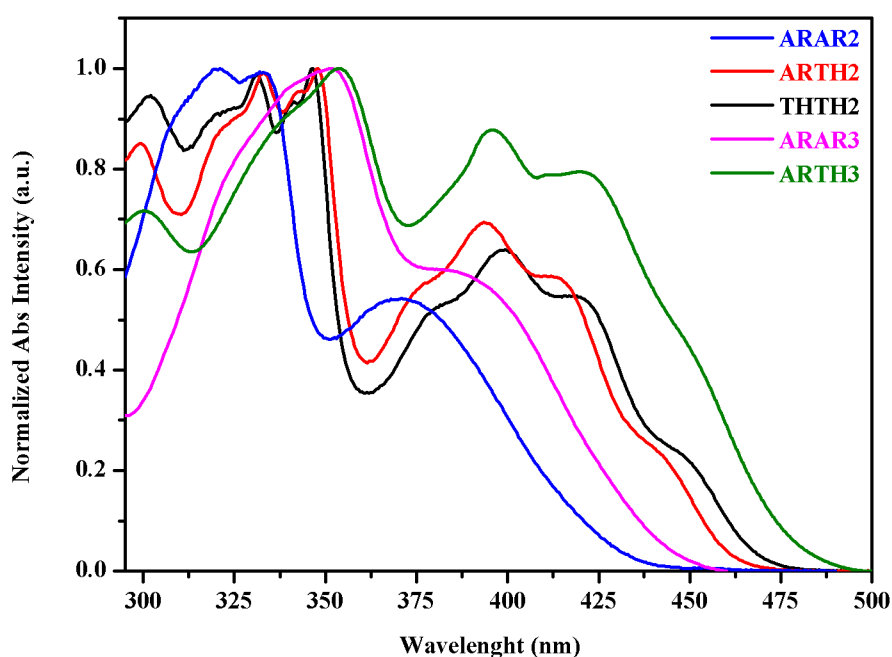


Figure A.22 UV-Visible absorption spectra of all products

1.1 E_g calculation for **ARAR2** (blue line; $\lambda_{onset} = 435$ nm)

$$E_g = 1240/\lambda_{onset}$$

$$E_g = 1240/435$$

$$E_g = 2.85 \text{ eV}$$

1.2 E_g calculation for **ARTH2** (red line; $\lambda_{onset} = 462$ nm)

$$E_g = 1240/\lambda_{onset}$$

$$E_g = 1240/462$$

$$E_g = 2.68 \text{ eV}$$

1.3 E_g calculation for **THTH2** (black line; $\lambda_{onset} = 469$ nm)

$$E_g = 1240/\lambda_{onset}$$

$$E_g = 1240/469$$

$$E_g = 2.64 \text{ eV}$$

1.4 E_g calculation for **ARAR3** (pink line; $\lambda_{onset} = 446$ nm)

$$E_g = 1240/\lambda_{onset}$$

$$E_g = 1240/446$$

$$E_g = 2.78 \text{ eV}$$

1.5 E_g calculation for **ARTH3** (green line; $\lambda_{onset} = 485$ nm)

$$E_g = 1240/\lambda_{onset}$$

$$E_g = 1240/485$$

$$E_g = 2.56 \text{ eV}$$

2. Lifetime spectra

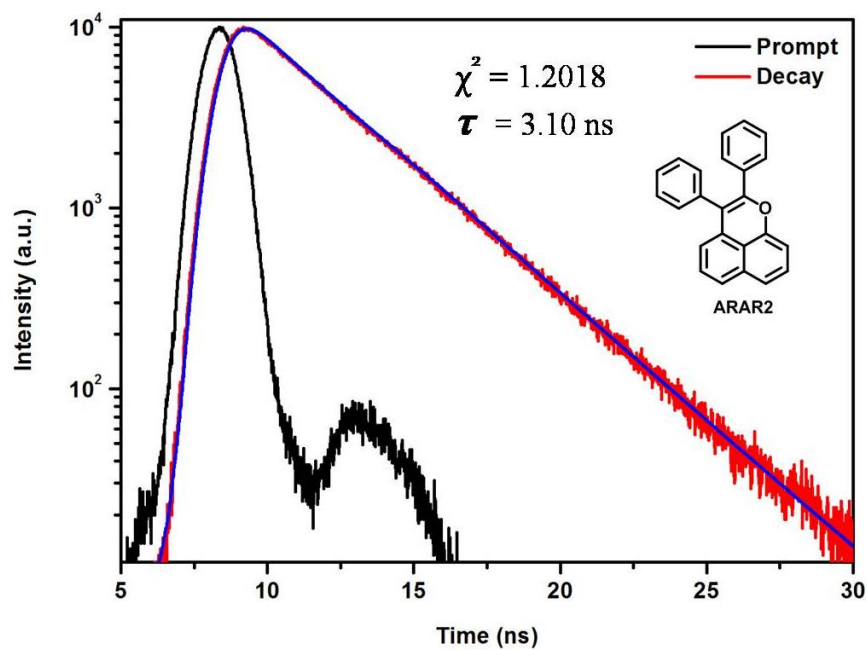


Figure A.23 Lifetime spectra of ARAR2

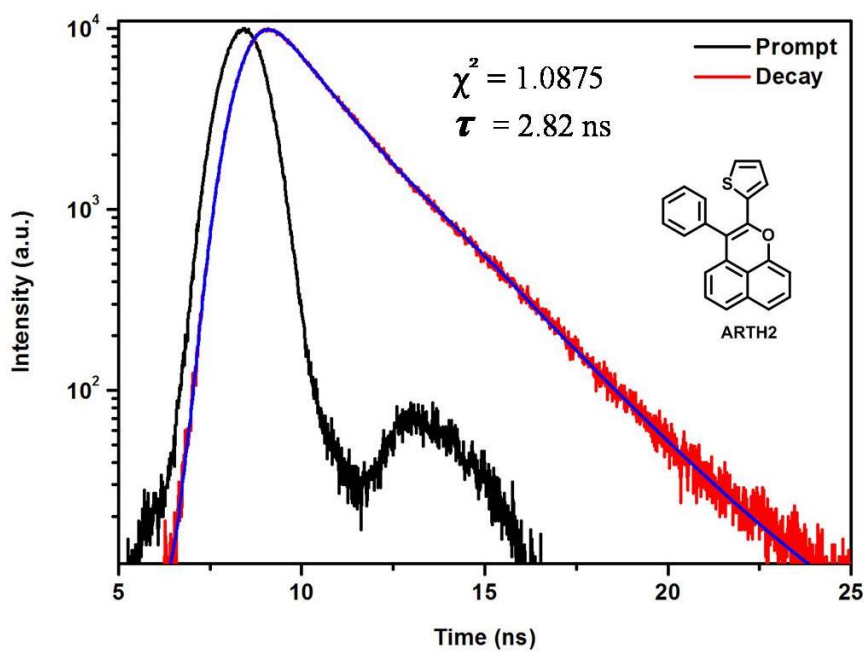


Figure A.24 Lifetime spectra of ARTH2

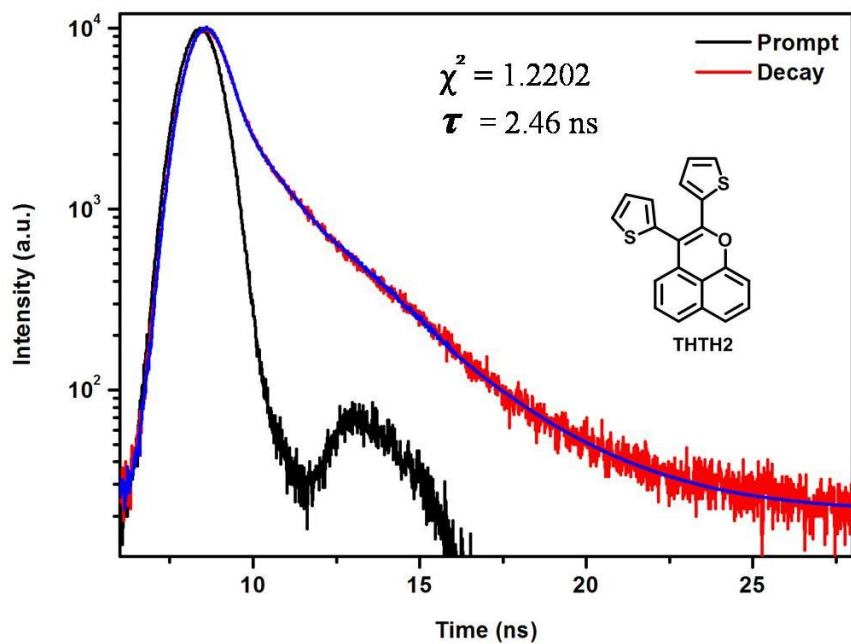


Figure A.25 Lifetime spectra of THTH2

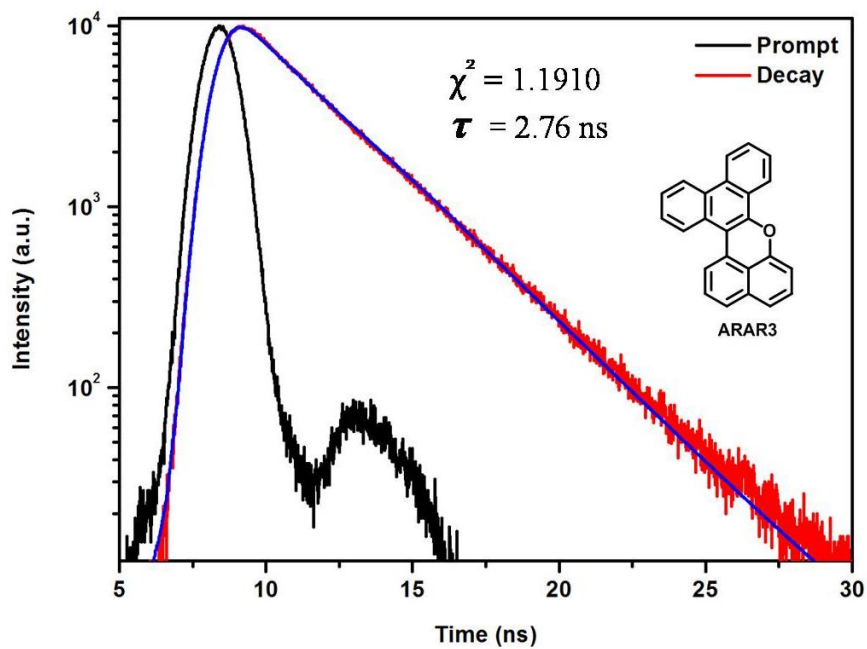


Figure A.26 Lifetime spectra of ARAR3

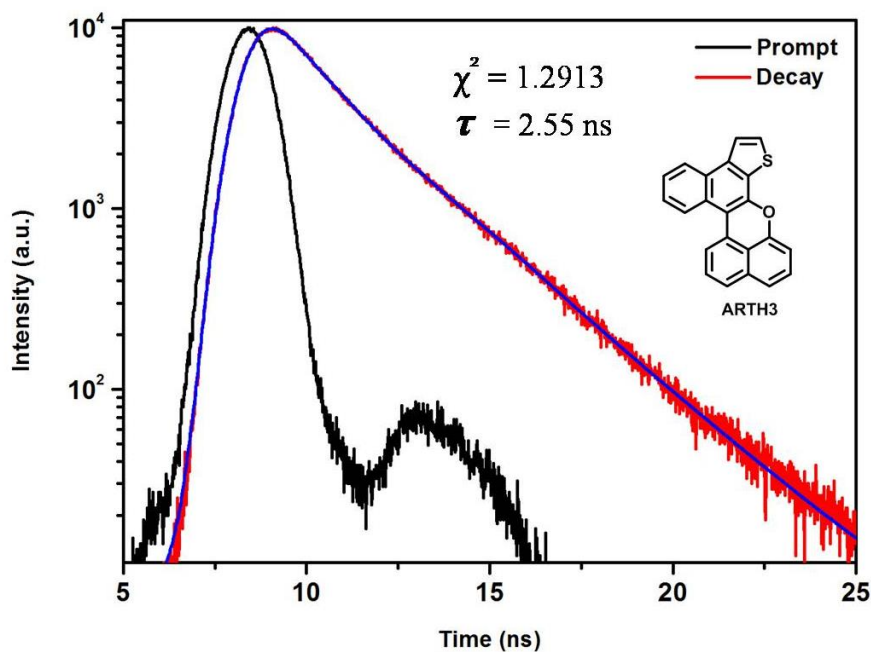


Figure A.27 Lifetime spectra of ARTH3

3. Quantum yield data calculation

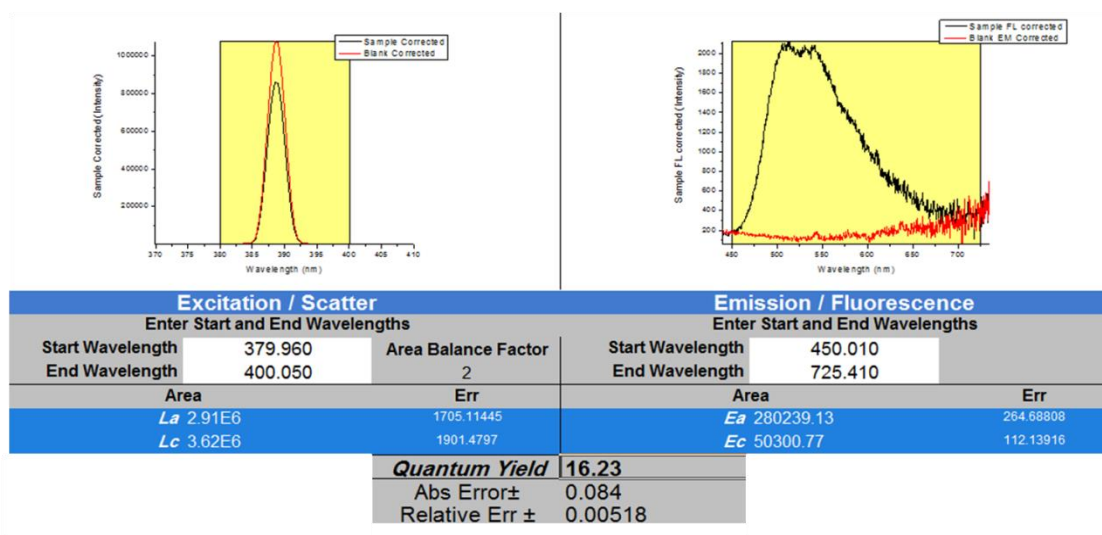


Figure A.28 Fluorescence quantum yield spectra of ARAR2

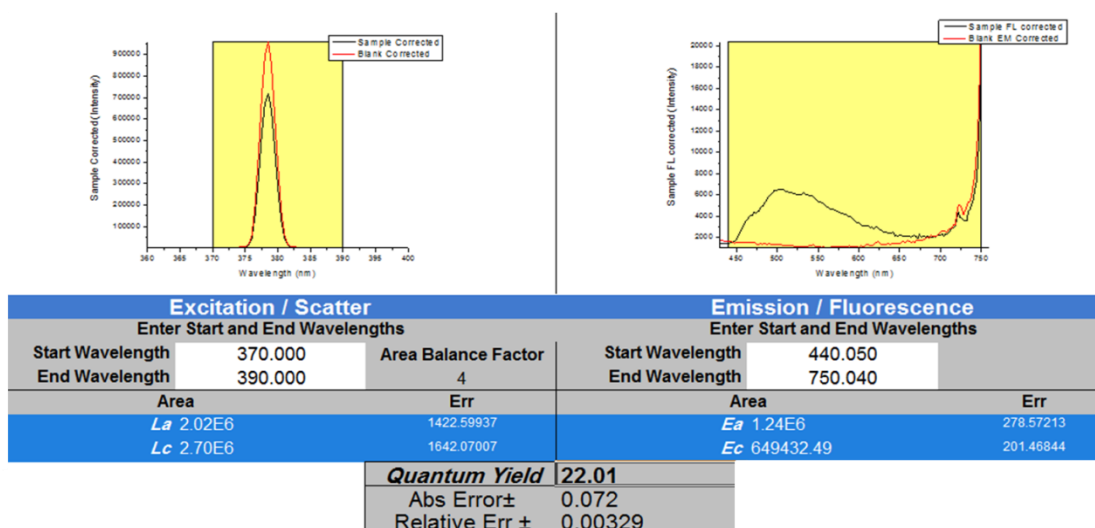


Figure A.29 Fluorescence quantum yield spectra of ARTH2

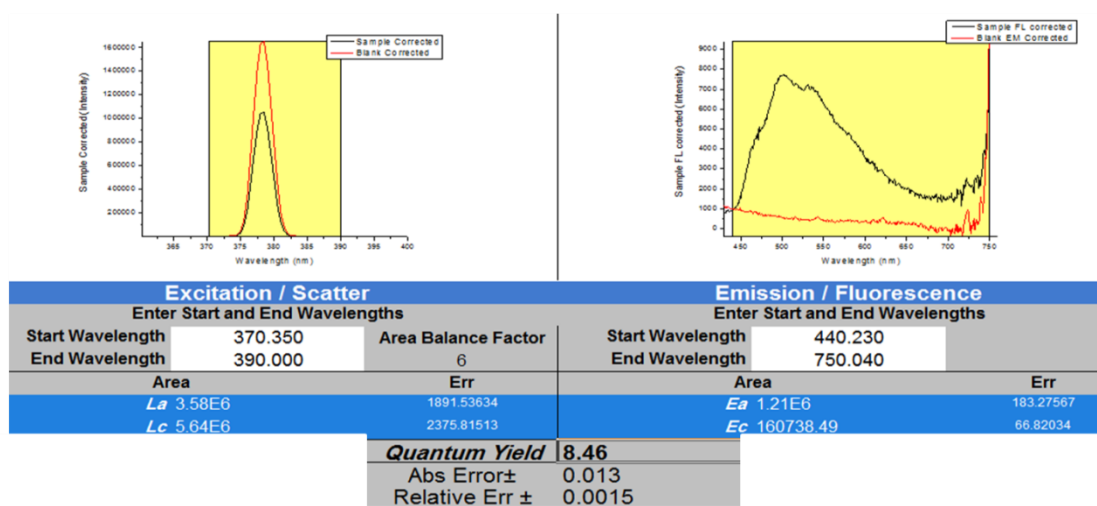


Figure A.30 Fluorescence quantum yield spectra of THTH2

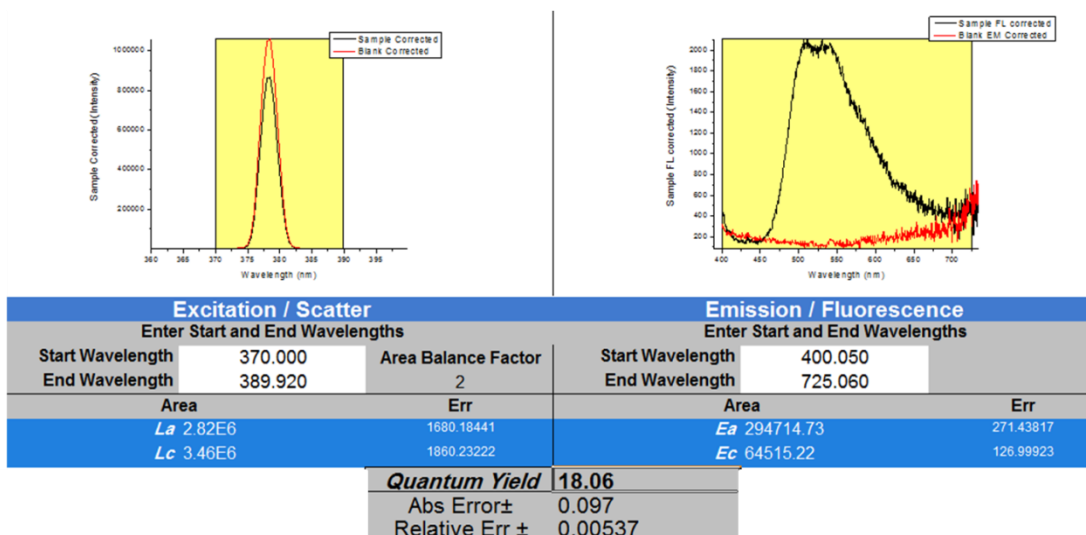


Figure A.31 Fluorescence quantum yield spectra of ARAR3

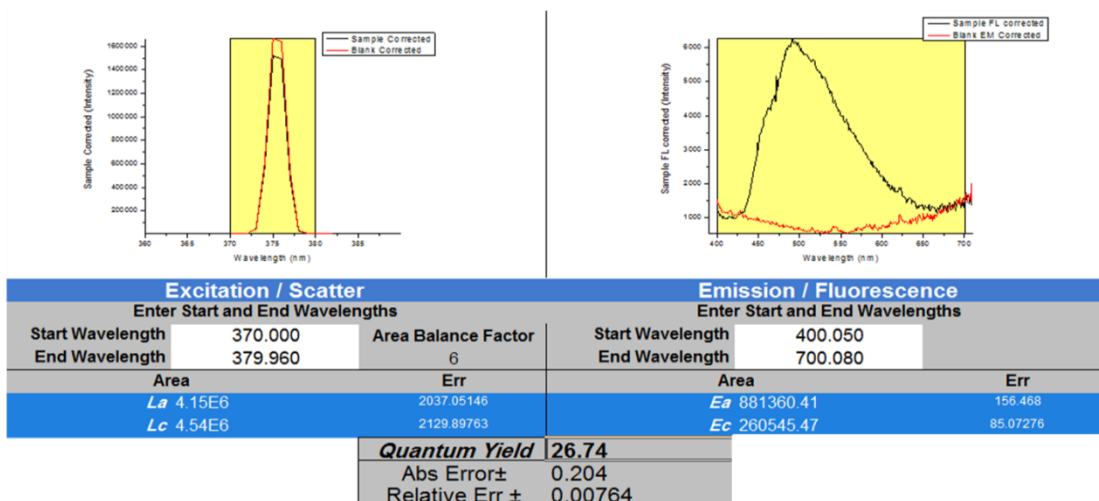


Figure A.32 Fluorescence quantum yield spectra of ARTH3

4. Electrochemical data calculation

Electrochemical data obtained from cyclic voltammetry measurement can be applied to estimate the LUMO energy levels of the materials. In this study, the LUMO energy levels can be determined from the reduction onset potential. Additionally, the HOMO energy levels were calculated from the difference of LUMO energy level and energy band gap of materials, as shown in equation below.

$$\text{LUMO} = -e \left(E_{\text{re, onset}} + 4.8 \text{ eV} - E_{1/2, \text{ Fe/Fe}^+} \right)$$

$$E_g = \text{LUMO} - \text{HOMO}$$

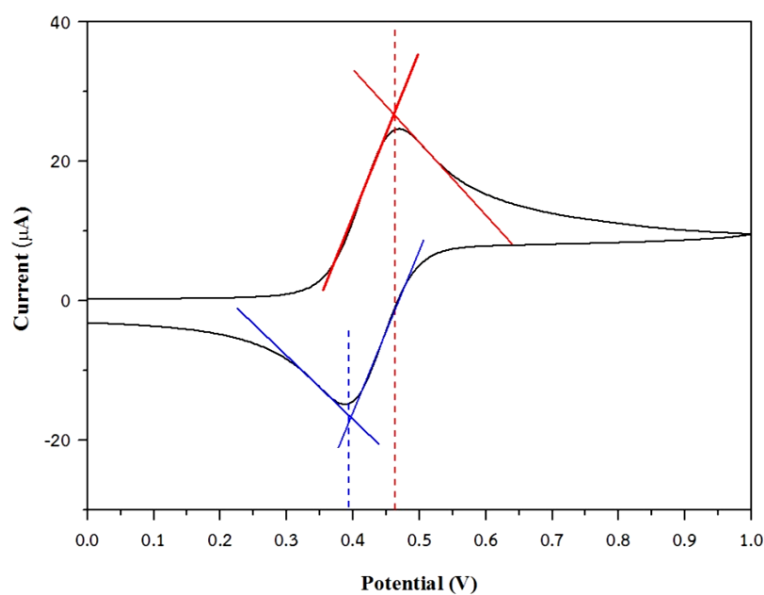


Figure A.33 Cyclic voltammogram of ferrocene in acetonitrile

$$\begin{aligned} E_{1/2, \text{ Fe/Fe}^+} &= (E_{\text{ox}} + E_{\text{re}})/2 \\ &= (0.46 + 0.39)/2 \\ &= 0.43 \text{ V} \end{aligned}$$

4.1 HOMO and LUMO levels calculation of ARAR2

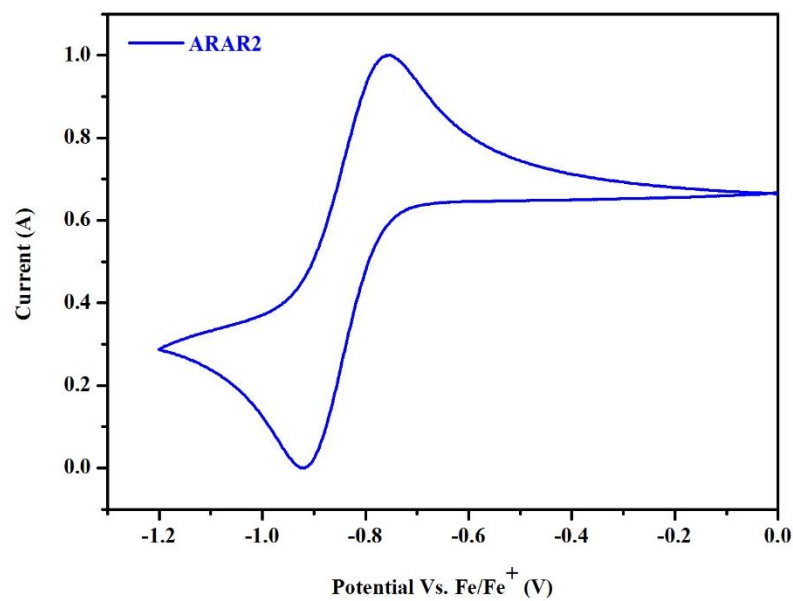


Figure A.34 Reduction potentials of ARAR2 in acetonitrile

ARAR2; $E_{\text{re, onset}} = -0.77 \text{ eV}$, $E_{1/2, \text{Fe/Fe}^+} = 0.43 \text{ eV}$, $E_g = 2.85 \text{ eV}$

$$\begin{aligned} \text{LUMO} &= -e (E_{\text{re, onset}} + 4.8 \text{ eV} - E_{1/2, \text{Fe/Fe}^+}) \\ &= -e (-0.77 \text{ eV} + 4.8 \text{ eV} - 0.43 \text{ eV}) \\ &= -3.60 \text{ eV} \end{aligned}$$

$$\begin{aligned} \text{HOMO} &= \text{LUMO} - E_g \\ &= -3.60 \text{ eV} - 2.85 \text{ eV} \\ &= -6.45 \text{ eV} \end{aligned}$$

4.2 HOMO and LUMO levels calculation of ARTH2

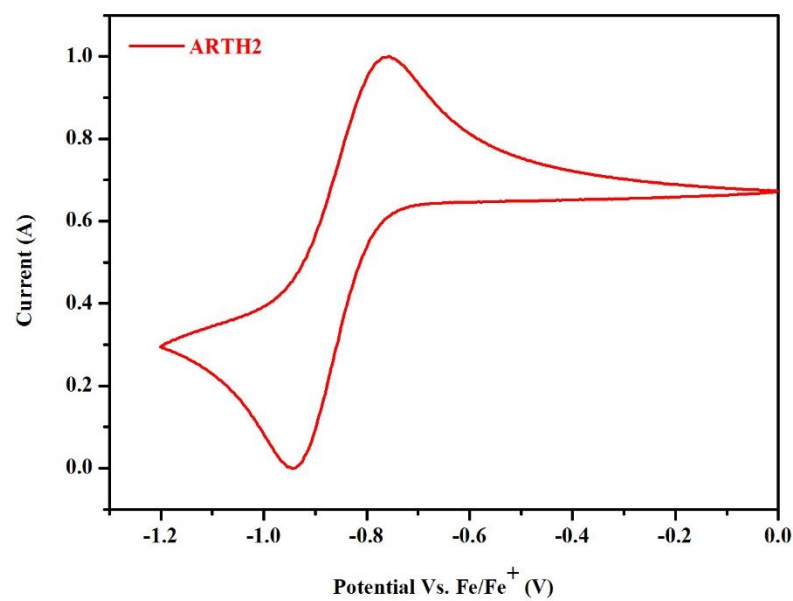


Figure A.35 Reduction potentials of ARTH2 in acetonitrile

ARTH2; $E_{\text{re, onset}} = -0.79 \text{ eV}$, $E_{1/2, \text{Fe/Fe}^+} = 0.43 \text{ eV}$, $E_g = 2.68 \text{ eV}$

$$\begin{aligned} \text{LUMO} &= -e (E_{\text{re, onset}} + 4.8 \text{ eV} - E_{1/2, \text{Fe/Fe}^+}) \\ &= -e (-0.79 \text{ eV} + 4.8 \text{ eV} - 0.43 \text{ eV}) \\ &= -3.58 \text{ eV} \end{aligned}$$

$$\begin{aligned} \text{HOMO} &= \text{LUMO} - E_g \\ &= -3.58 \text{ eV} - 2.68 \text{ eV} \\ &= -6.26 \text{ eV} \end{aligned}$$

4.3 HOMO and LUMO levels calculation of THTH2

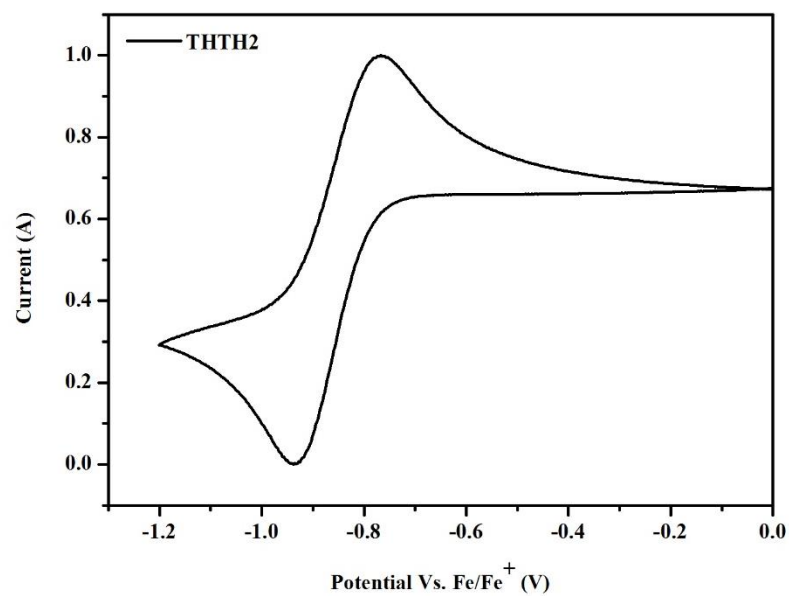


Figure A.36 Reduction potentials of THTH2 in acetonitrile

THTH2; $E_{\text{re, onset}} = -0.78 \text{ eV}$, $E_{1/2, \text{Fe/Fe}^+} = 0.43 \text{ eV}$, $E_{\text{g}} = 2.64 \text{ eV}$

$$\begin{aligned} \text{LUMO} &= -e (E_{\text{re, onset}} + 4.8 \text{ eV} - E_{1/2, \text{Fe/Fe}^+}) \\ &= -e (-0.78 \text{ eV} + 4.8 \text{ eV} - 0.43 \text{ eV}) \\ &= -3.59 \text{ eV} \end{aligned}$$

$$\begin{aligned} \text{HOMO} &= \text{LUMO} - E_{\text{g}} \\ &= -3.59 \text{ eV} - 2.64 \text{ eV} \\ &= -6.23 \text{ eV} \end{aligned}$$

4.4 HOMO and LUMO levels calculation of ARAR3

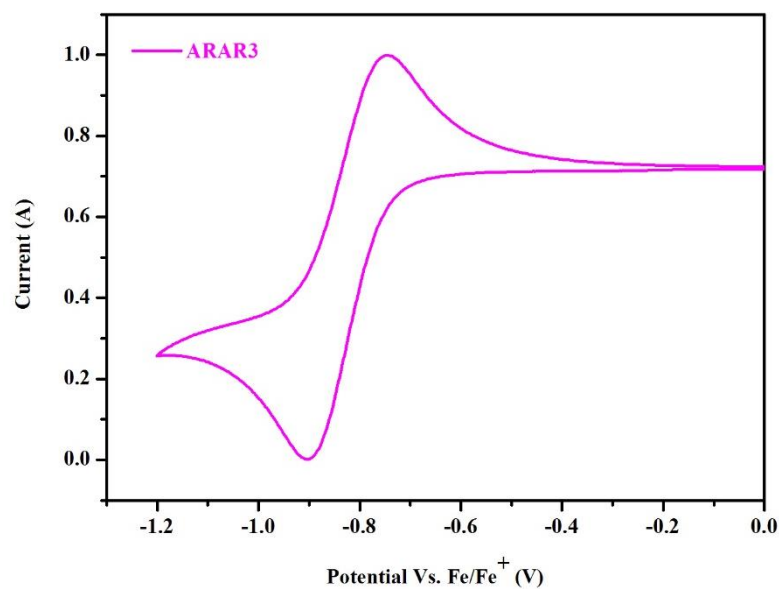


Figure A.37 Reduction potentials of ARAR3 in acetonitrile

ARAR3; $E_{re} = -0.74$ eV, $E_{1/2, Fe/Fe^+} = 0.43$ eV, $E_g = 2.78$ eV

$$\begin{aligned} \text{LUMO} &= -e (E_{re, \text{onset}} + 4.8 \text{ eV} - E_{1/2, Fe/Fe^+}) \\ &= -e (-0.74 \text{ eV} + 4.8 \text{ eV} - 0.43 \text{ eV}) \\ &= -3.63 \text{ eV} \end{aligned}$$

$$\begin{aligned} \text{HOMO} &= \text{LUMO} - E_g \\ &= -3.63 \text{ eV} - 2.78 \text{ eV} \\ &= -6.41 \text{ eV} \end{aligned}$$

4.5 HOMO and LUMO levels calculation of ARTH3

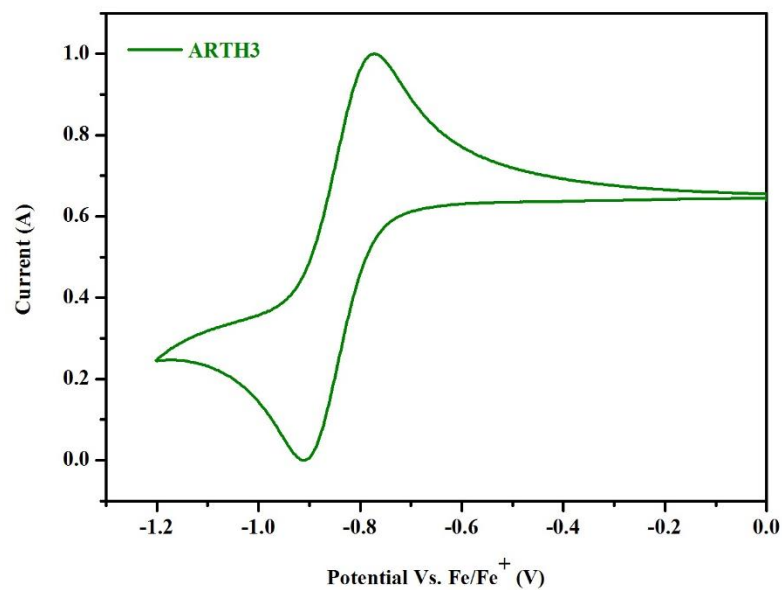


Figure A.38 Reduction potentials of ARTH3 in acetonitrile

ARTH3; $E_{re} = -0.76$ eV, $E_{1/2, Fe/Fe^+} = 0.43$ eV, $E_g = 2.56$ eV

$$\begin{aligned} \text{LUMO} &= -e (E_{re, \text{onset}} + 4.8 \text{ eV} - E_{1/2, Fe/Fe^+}) \\ &= -e (-0.76 \text{ eV} + 4.8 \text{ eV} - 0.43 \text{ eV}) \\ &= -3.61 \text{ eV} \end{aligned}$$

$$\begin{aligned} \text{HOMO} &= \text{LUMO} - E_g \\ &= -3.61 \text{ eV} - 2.56 \text{ eV} \\ &= -6.17 \text{ eV} \end{aligned}$$

APPENDIX C
Device performances data

1. OLEDs performance data

1.1 OLEDs performance of ARAR2

ITO/NPB(30nm)/MADN: 20%**ARAR2**(40nm)/Bphen(30nm)/LiF(0.5nm)/Al(100nm)

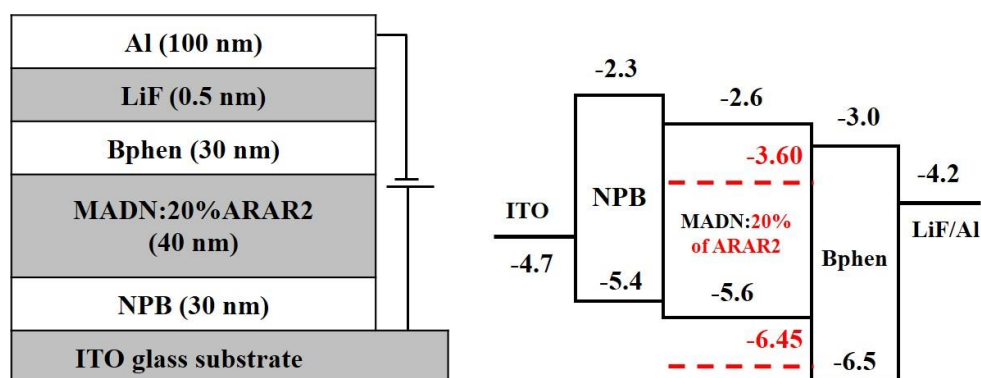


Figure A.39 OLEDs device fabrication and energy level diagram of ARAR2

Emitting layer 40 nm (host 33 nm: guest 7 nm)	CE (cd/A)	PE (Lm/W)	L (cd/m ²)	V _{turn on} (V)	CIE (x, y)
MADN:20% ARAR2	2.09	0.57	4,114	7.3	(0.36, 0.52)

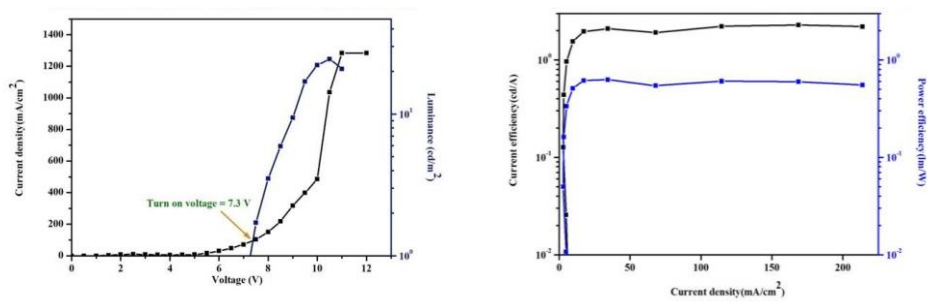


Figure A.40 Current density and luminance versus applied bias voltage (left) and current and power efficiencies (right) of ARAR2 device

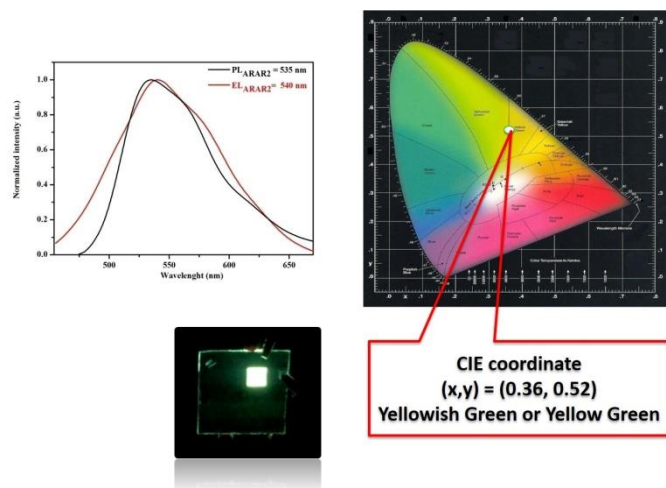


Figure A.41 PL, EL, CIE coordinate and emission colour of ARAR2 device

1.2 OLEDs performance of ARTH2

ITO/NPB(30nm)/MADN: 20% ARTH2(40nm)/Bphen(30nm)/LiF(0.5nm)/Al(100nm)

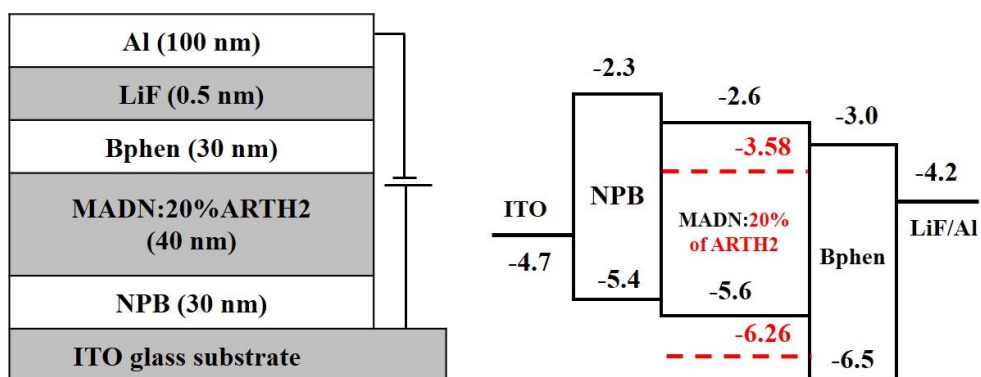


Figure A.42 OLEDs device fabrication and energy level diagram of ARTH2

Emitting layer 40 nm (host 33 nm: guest 7 nm)	CE (cd/A)	PE (Lm/W)	L (cd/m ²)	$V_{\text{turn on}}$ (V)	CIE (x, y)
MADN:20% ARTH2	2.71	0.79	4,699	6.3	(0.30, 0.48)

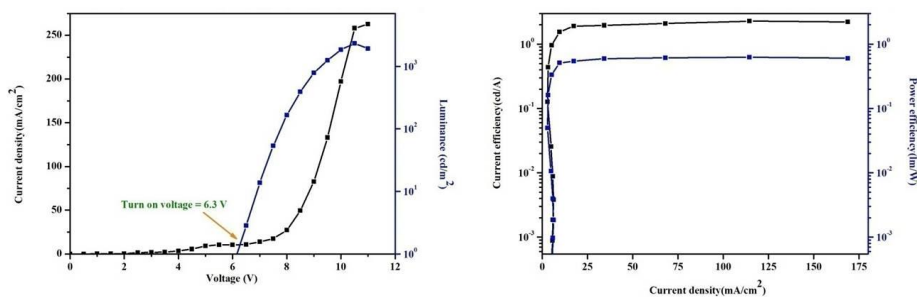


Figure A.43 Current density and luminance versus applied bias voltage (left) and current and power efficiencies (right) of ARTH2 device

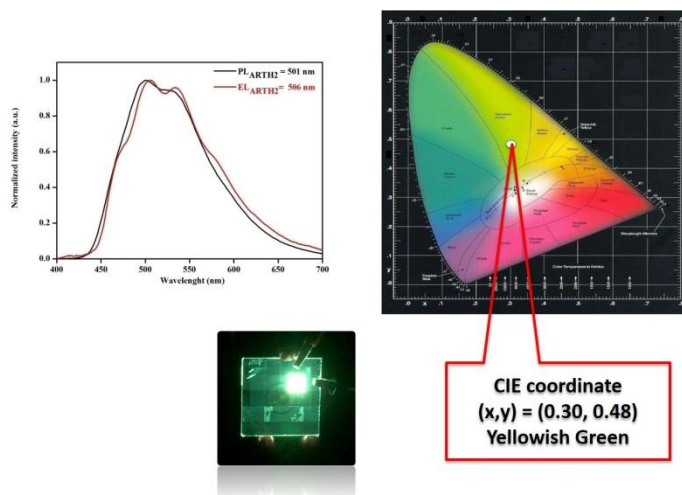


Figure A.44 PL, EL, CIE coordinate and emission colour of ARTH2 device

1.3 OLEDs performance of THTH2

ITO/NPB(30nm)/MADN: 20% THTH2(40nm)/Bphen(30nm)/LiF(0.5nm)/Al(100nm)

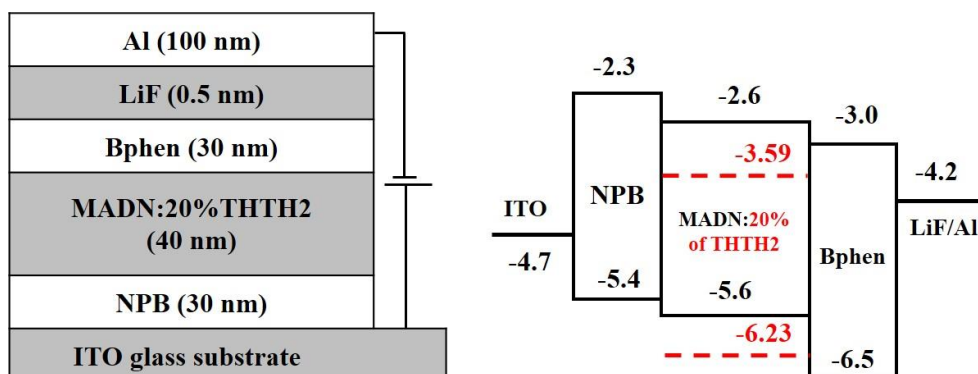


Figure A.45 OLEDs device fabrication and energy level diagram of THTH2

Emitting layer 40 nm (host 33 nm: guest 7 nm)	CE (cd/A)	PE (Lm/W)	L (cd/m ²)	$V_{\text{turn on}}$ (V)	CIE (x, y)
MADN:20% THTH2	1.36	0.33	3,492	6.5	(0.32, 0.49)

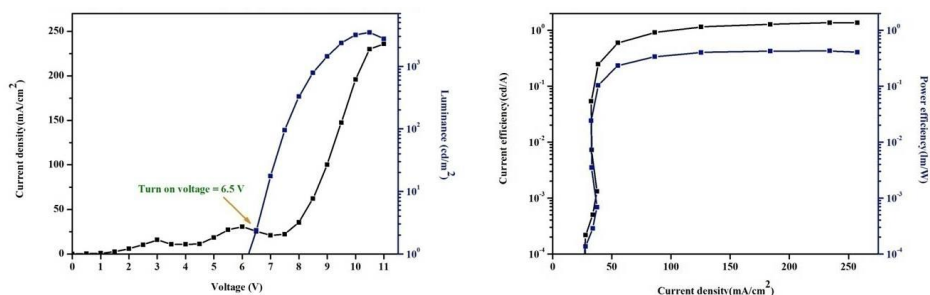


Figure A.46 Current density and luminance versus applied bias voltage (left) and current and power efficiencies (right) of THTH2 device

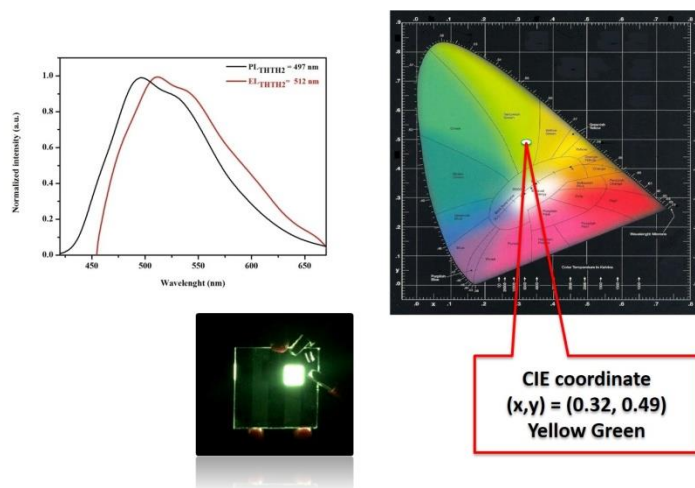


Figure A.47 PL, EL, CIE coordinate and emission colour of THTH2 device

1.4 OLEDs performance of ARAR3

ITO/NPB(30nm)/MADN: 20% ARAR3(40nm)/Bphen(30nm)/LiF(0.5nm)/Al(100nm)

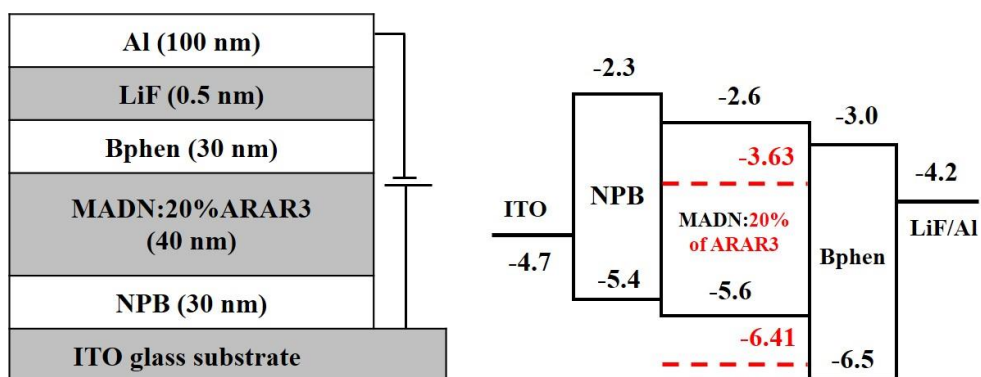


Figure A.48 OLEDs device fabrication and energy level diagram of ARAR3

Emitting layer 40 nm (host 33 nm: guest 7 nm)	CE (cd/A)	PE (Lm/W)	L (cd/m ²)	$V_{\text{turn on}}$ (V)	CIE (x, y)
MADN:20% ARAR3	1.85	0.29	2,670	8.7	(0.28, 0.45)

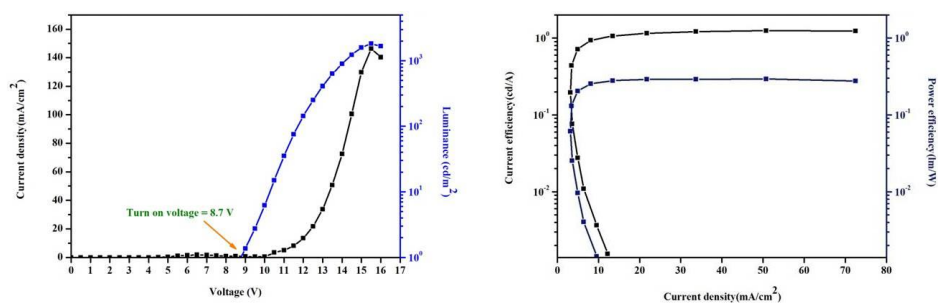


Figure A.49 Current density and luminance versus applied bias voltage (left) and current and power efficiencies (right) of ARAR3 device

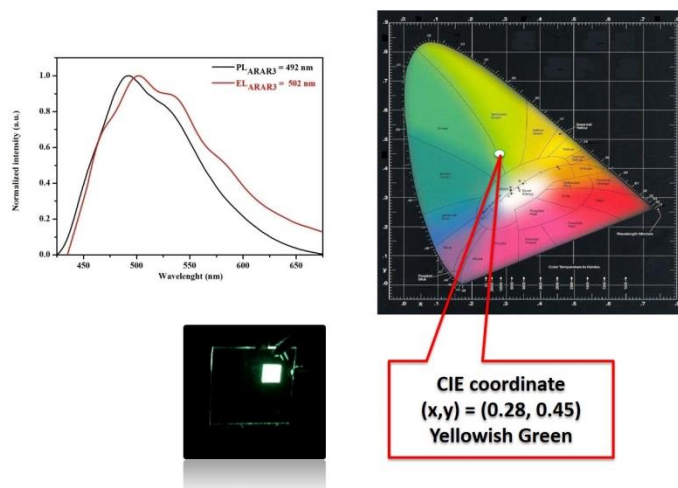


Figure A.50 PL, EL, CIE coordinate and emission colour of ARAR3 device

1.5 OLEDs performance of ARTH3

ITO/NPB(30nm)/MADN: 20%**ARTH3**(40nm)/Bphen(30nm)/LiF(0.5nm)/Al(100nm)

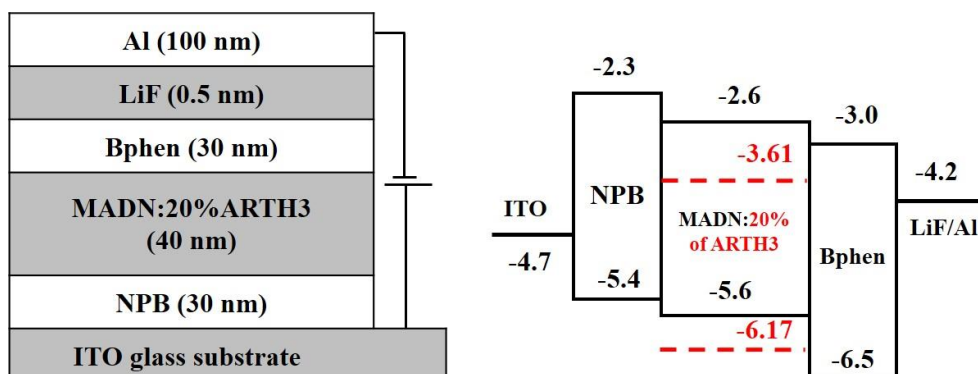


Figure A.51 OLEDs device fabrication and energy level diagram of ARTH3

Emitting layer 40 nm (host 33 nm: guest 7 nm)	CE (cd/A)	PE (Lm/W)	<i>L</i> (cd/m ²)	<i>V</i> _{turn on} (V)	CIE (x, y)
MADN:20% ARTH3	2.28	0.43	2,941	7.5	(0.39, 0.47)

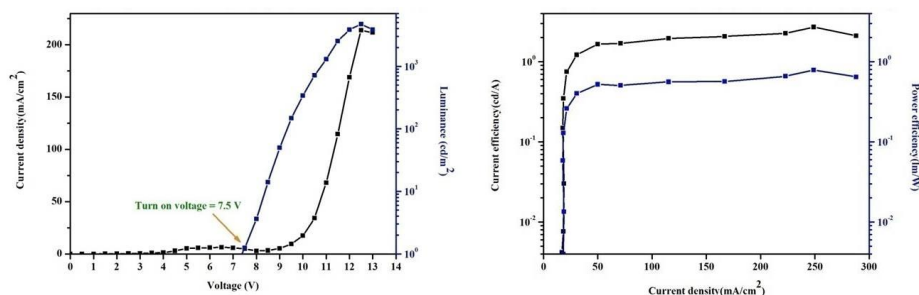


Figure A.52 Current density and luminance versus applied bias voltage (left) and current and power efficiencies (right) of ARTH3 device

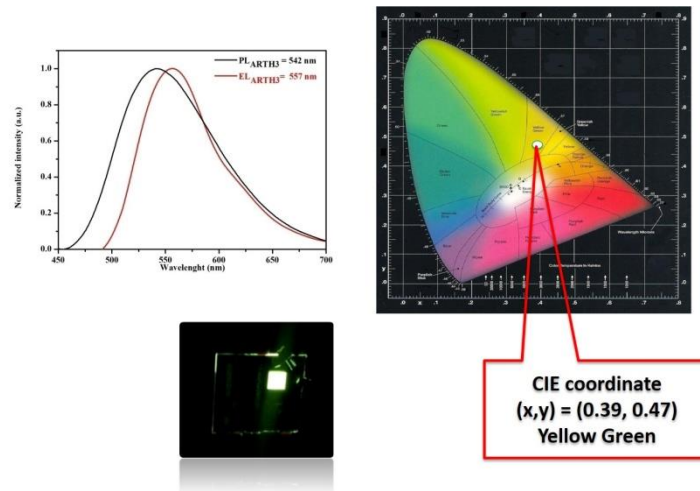


Figure A.53 PL, EL, CIE coordinate and emission colour of ARTH3 device

2. OFETs performance data

The relationship between the carrier speed in a material and the applied electric field, measured in unit of square centimeter per volt second (cm^2/Vs). The field-effect mobility was calculated from the saturation region with the following equation.

$$\mu = \frac{I_{DS}2L}{WC_i(V_G - V_T)^2}$$

Where μ is the hole mobility, I_{DS} is the drain-source current, L is the channel length ($20 \mu\text{m}$), W is the channel width ($17,000 \mu\text{m}$), C_i is the capacitance per unit area of the gate dielectric layer ($1.09 \times 10^{-8} \text{ F}/\text{cm}^2$), and V_G and V_T are the gate voltage and threshold voltage, respectively.

2.1 OFETs performance of pentacene

Pentacene (30 nm)/ T_{sub} (80°C)/ rate (0.1 Å/s)/ Au (100 nm)

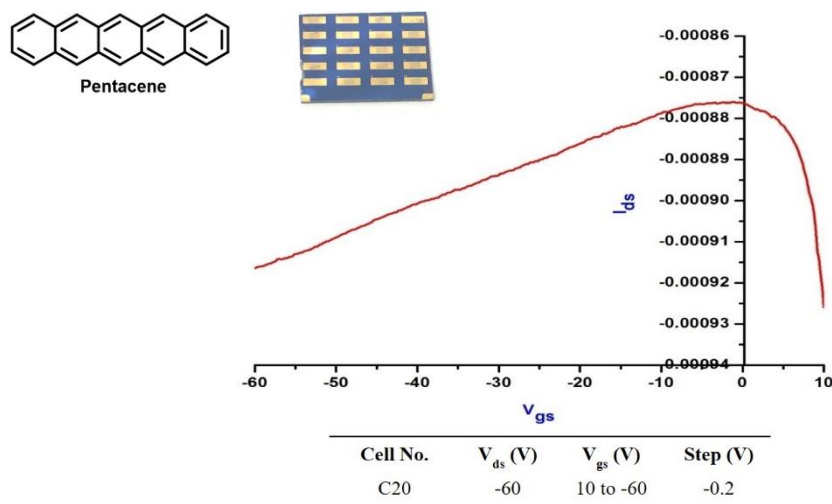


Figure A.54 Transfer curve at gate-source voltage 10 to -60 V of pentacene

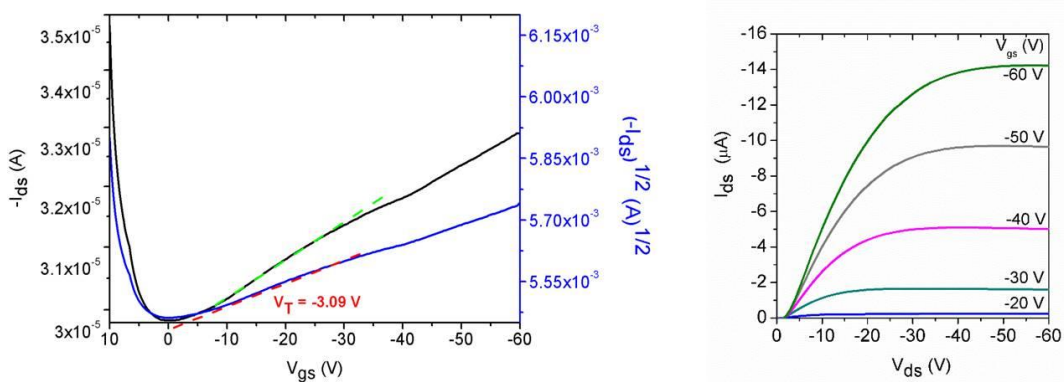


Figure A.55 Transfer curve (left) and output curve (right) of pentacene

2.1.1 Hole mobility calculation of pentacene ($I_{DS} = 14 \times 10^{-6}$ C/s, $V_G = -60$ V, $V_T = -3.09$ V, $W = 17,000 \mu\text{m}$, $L = 20 \mu\text{m}$, $C_i = 1.09 \times 10^{-8}$ C/Vcm²)

$$\mu = \frac{I_{DS} 2L}{WC_i (V_G - V_T)^2}$$

$$\mu = (14 \times 10^{-6})(2 \times 20) / (17,000)(1.09 \times 10^{-8}) [(-60) - (-3.09)]^2$$

$$\mu = 9.33 \times 10^{-4} \text{ cm}^2/\text{Vs}$$

2.2 OFETs performance of ARAR2

ARAR2 (30 nm)/ T_{sub} (80°C)/ rate (0.1 Å/s)/ Au (100 nm)

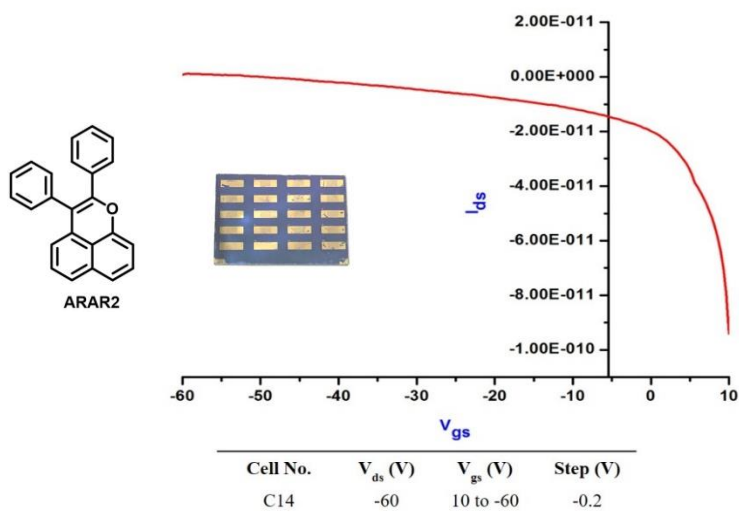


Figure A.56 Transfer curve at gate-source voltage 10 to -60 V of ARAR2

2.3 OFETs performance of ARTH2

ARTH2 (30 nm)/ T_{sub} (80°C)/ rate (0.1 Å/s)/ Au (100 nm)

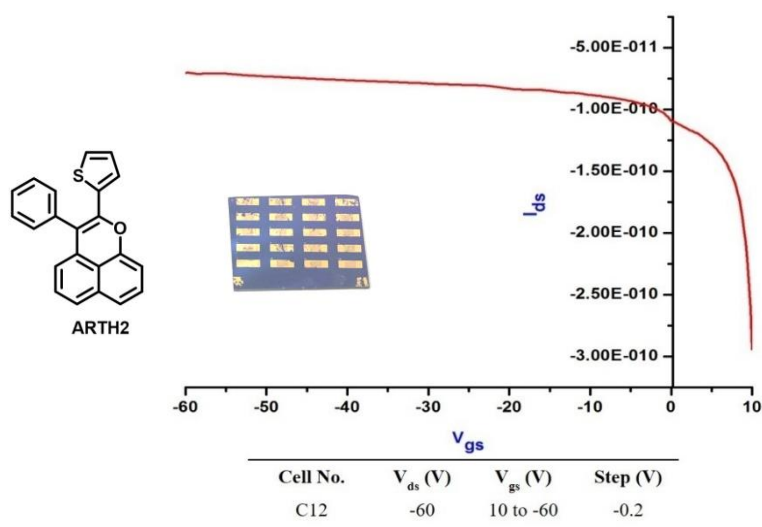


Figure A.57 Transfer curve at gate-source voltage 10 to -60 V of ARTH2

2.4 OFETs performance of THTH2

THTH2 (30 nm)/ T_{sub} (80°C)/ rate (0.1 Å/s)/ Au (100 nm)

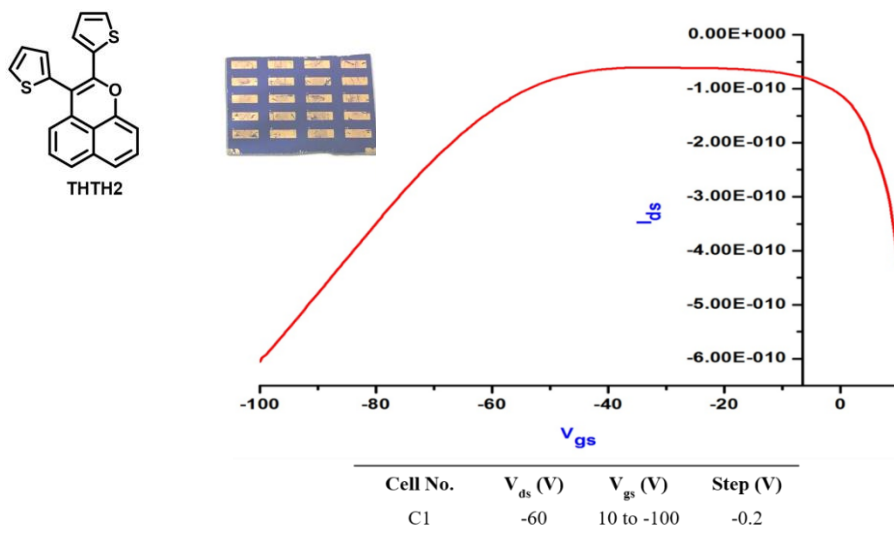


Figure A.58 Transfer curve at gate-source voltage 10 to -100 V of THTH2

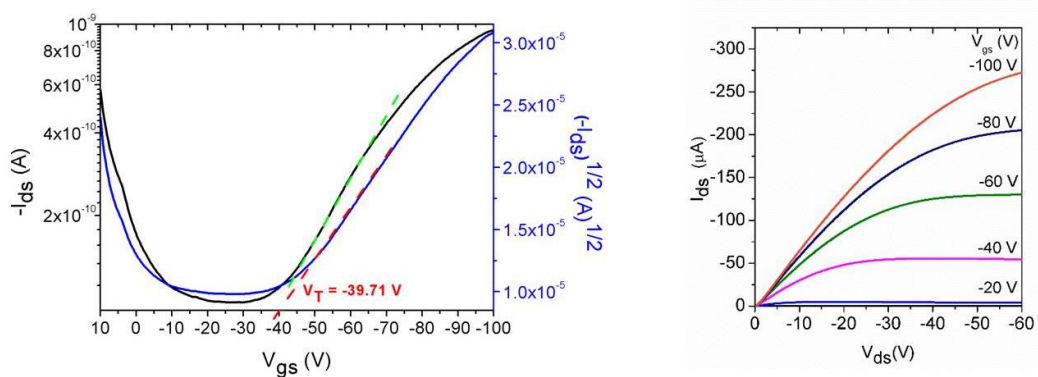


Figure A.59 Transfer curve (left) and output curve (right) of THTH2

2.4.1 Hole mobility calculation of THTH2 ($I_{DS} = 275 \times 10^{-6}$ C/s, $V_G = -100$ V, $V_T = -39.37$ V, $W = 17,000 \mu\text{m}$, $L = 20 \mu\text{m}$, $C_i = 1.09 \times 10^{-8}$ C/Vcm²)

$$\mu = \frac{I_{DS} 2L}{WC_i (V_G - V_T)^2}$$

$$\mu = (275 \times 10^{-6})(2 \times 20) / (17,000)(1.09 \times 10^{-8}) [(-100) - (-39.37)]^2$$

$$\mu = 1.64 \times 10^{-2} \text{ cm}^2/\text{Vs}$$

2.5 OFETs performance of ARAR3

ARAR3 (30 nm)/ T_{sub} (80°C)/ rate (0.1 Å/s)/ Au (100 nm)

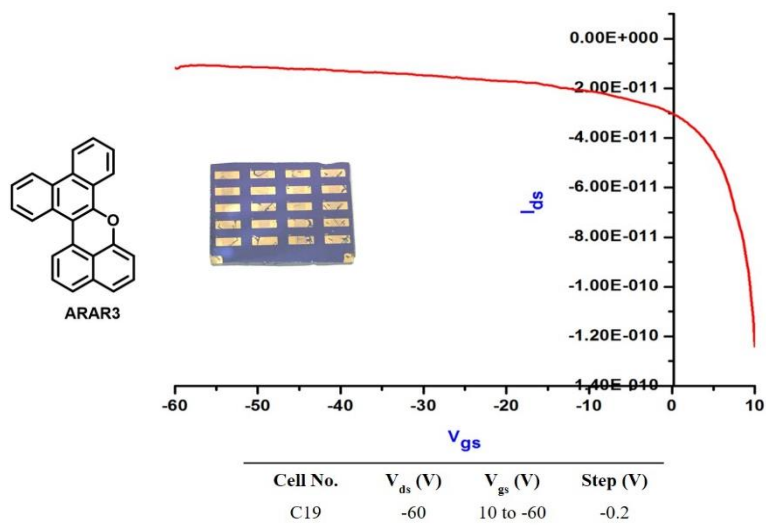


Figure A.60 Transfer curve at gate-source voltage 10 to -60 V of ARAR3

2.6 OFETs performance of ARTH3

ARTH3 (30 nm)/ T_{sub} (80°C)/ rate (0.1 Å/s)/ Au (100 nm)

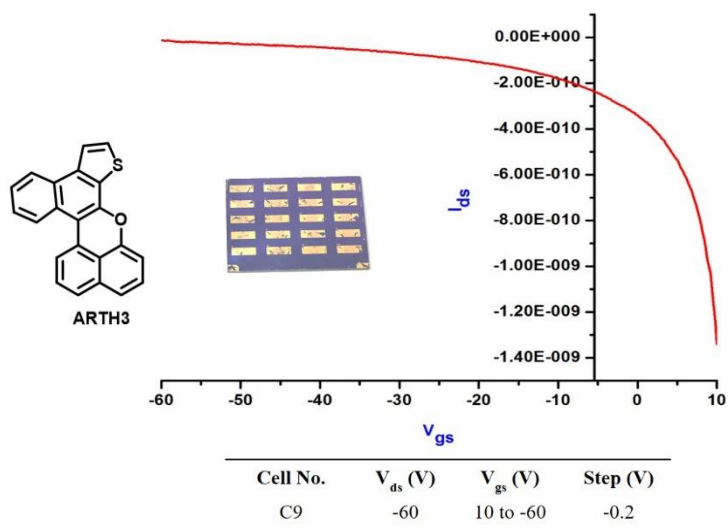


Figure A.61 Transfer curve at gate-source voltage 10 to -60 V of ARTH3

APPENDIX D
Publication

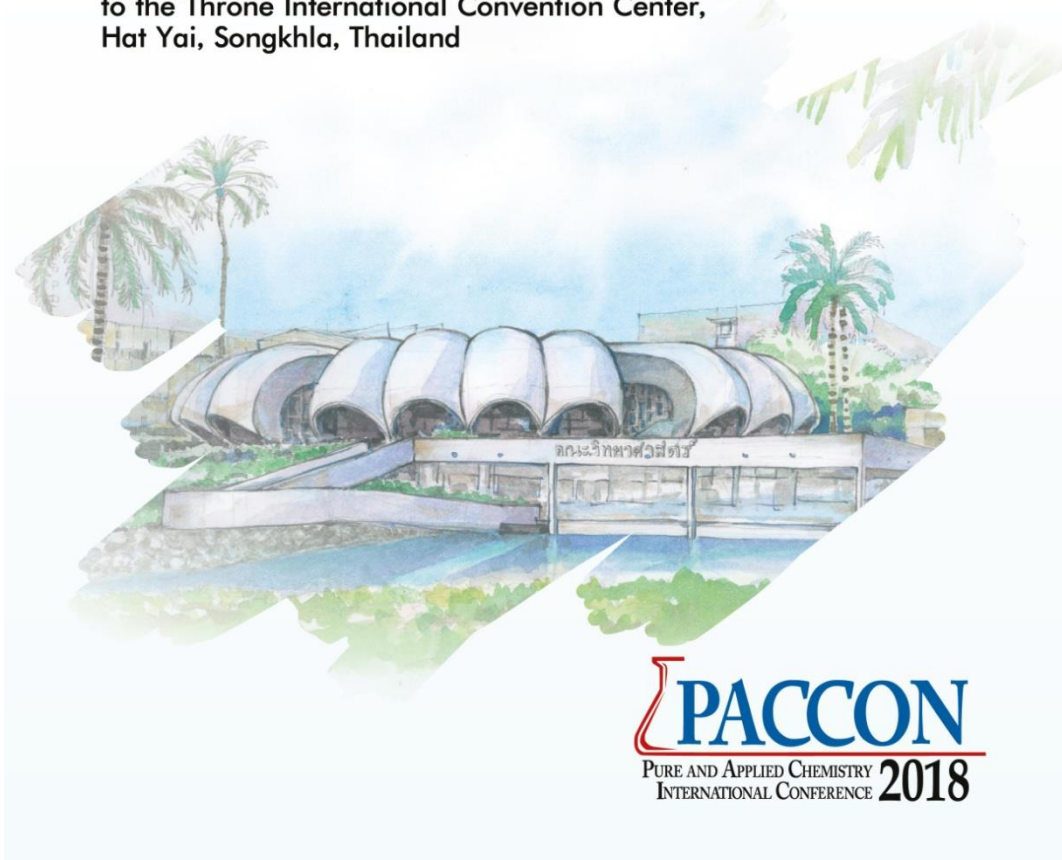


CHEMISTRY TOWARD A SUSTAINABLE FUTURE

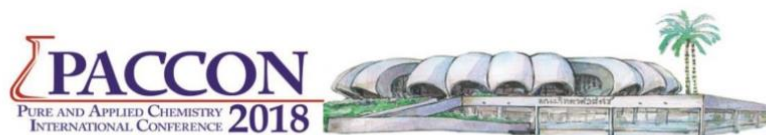
Proceedings

February 7-9, 2018

The 60th Anniversary of His Majesty the King's Accession
to the Throne International Convention Center,
Hat Yai, Songkhla, Thailand



PACCON
PURE AND APPLIED CHEMISTRY
INTERNATIONAL CONFERENCE **2018**



**Tribenzo[*a,c,k,l*]xanthene:
a novel fluorophore from an intramolecular Scholl reaction**

Thikhamporn Uppalabat, Rukkiat Jitchati*

*Department of Chemistry, Faculty of Science, Ubon Ratchathani University, Warinchumrap,
Ubon Ratchathani 34190, Thailand*

**E-mail: rukkiat_j@hotmail.com*

Abstract:

The Scholl reaction has been known as a coupling reaction of aromatic hydrocarbons (arenes) with the oxidative coupling reagents. The authors have reported the synthesis of tribenzo[*a,c,k,l*]xanthene (**ARAR3**) via Fe-catalyzed intramolecular Scholl reaction, from the diphenylbenzo[*d,e*]chromene (**ARAR2**). The optimization reaction was quite enough in the case that the yield was satisfied at 75%. The chemical structure was characterized by ¹H and ¹³C NMR. The photophysical properties were studied by UV-Vis absorption and emission techniques. The results showed the maximum $\pi-\pi^*$ absorption at 335 nm and emission at 500 nm. In addition, the highest occupied molecular orbital (HOMO) and the lowest unoccupied molecular orbital (LUMO) levels were obtained at -5.04 and -2.21 eV, respectively. The results showed that the **ARAR3** was quite promising to be widely useful organic material in the future.

1. Introduction

Scholl reaction or oxidative dehydrogenative cyclization used for the construction of new carbon-carbon bonds to fuse π -conjugated systems has been witnessed as a useful chemical strategy for the synthesis of novel fluorophore.¹ Wide studies on the mechanistic aspects of this reaction have been carried out both experimentally and theoretically to better understand because the unexpected cyclization routes are frequently observed. The intramolecular Scholl reaction² can be proceeded with the oxidant coupling reagents as a valuable procedure to access a new biaryl units.³

More specifically, the intramolecular Scholl reaction has been extended the formation the six-membered rings.⁴ Recently, Cao et al. investigated a novel compound containing fused the six-membered rings of oligobenzofuran derivatives by using ferric chloride as an oxidative reagent.⁵

In this work, we studied the intramolecular Scholl reaction of 2,3-diphenylbenzo[*d,e*]chromene by using the oxidative coupling reagent (FeCl₃). The authors also performed the study of

molecular properties, such as optical, thermal, photophysical and electrochemical properties.

2. Materials and Methods

2.1 General

All reactants and solvents were purchased from commercial sources and used without further purification unless otherwise noted. The substrate (**ARAR2**) was prepared from cyclization reaction. ¹H and ¹³C NMR spectra were recorded on a Bruker ARX-300 spectrometer. Molecular weight was obtained using a Bruker MicroTOF-Q II. UV-visible absorption and emission spectra were studied with Perkin Elmer spectrophotometer (LS50). The thermal gravimetric analysis (TGA) was measured on a Thermo plus TG 8120 with heating rate of 10 °C/min in nitrogen atmosphere.

2.2 Synthesis and characterization

The synthesis of **ARAR2** compound from cyclization reaction⁶ was obtained the yellow solid (73%); m.p. 134-138 °C; ¹H NMR (300 MHz, CDCl₃) δ 7.38-7.12 (m, *J* = 7.25 Hz, 14H), 6.88, 6.86 (d, *J* = 6.87 Hz, 1H), 6.46, 6.44 (d, *J* = 6.45 Hz, 1H); ¹³C NMR (75 MHz, CDCl₃) δ 152.7, 149.4,

135.5, 134.8, 134.2, 131.9, 130.9, 129.0, 128.9, 128.3, 127.6, 127.5, 127.4, 123.6, 122.9, 119.1, 117.5, 115.6, 106.9; HRMS calcd for $C_{24}H_{17}O$ ($M+H^+$): 321.1279, found: 321.1279.

The study of the intramolecular Scholl reaction was obtained **ARAR3** compound. The mixture of **ARAR2** (1 eq.) in 15 ml of dried dichloromethane (CH_2Cl_2) at 0 °C and then $FeCl_3$ (6-15 eq.) in 1-3 ml of nitromethane (CH_3NO_2). The mixture was stirred under nitrogen atmosphere for 5, 30, 60 minutes. After that, the reaction was quenched by the addition of methanol and water, respectively. Crude reaction was extracted with dichloromethane and water. Then the organic part was purified by column chromatography (hexane as a mobile phase) to obtain the yellow solid (6-75%); m.p. 162-164 °C; 1H NMR (400 MHz, $CDCl_3$) δ 7.55, 7.53 (d, $J = 7.54$ Hz, 1H), 7.40, 7.38, 7.46 (t, $J = 7.38$ Hz, 1H), 7.32-7.09 (m, $J = 7.20$ Hz, 10H), 6.91, 6.89 (d, $J = 6.90$ Hz, 1H), 6.32, 6.30 (d, $J = 6.31$ Hz, 1H); ^{13}C NMR (75 MHz, $CDCl_3$) δ 152.6, 149.4, 135.1, 133.8, 131.8, 131.1, 130.9, 129.2, 128.9, 128.6, 128.4, 127.7, 127.1, 123.5, 117.2, 116.1, 115.6, 108.1.

3. Results and Discussion

3.1 Intramolecular Scholl reaction study

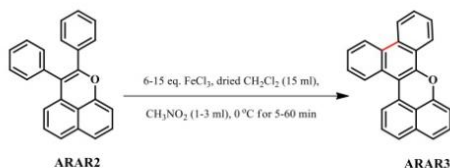


Figure 1. The study of intramolecular Scholl reaction

From Table 1, the intramolecular Scholl reaction of **ARAR2** was studied with a varied equivalents of $FeCl_3$. The results found that the entry 12 with 6 equivalents of $FeCl_3$ after 60 minutes showed a good yield at 75%. It should be noted that the minor products may be the conjugated dimer or trimer or other products from the similar 1H NMR with **ARAR3**.

Table 1. The optimization of intramolecular Scholl reaction^a

Entry	eq. of $FeCl_3$	Time (min)	%yield (ARAR3)
1 ⁷	15	5	6
2		30	11
3		60	18
4 ⁸	12	5	12
5		30	26
6		60	33
7	10	5	11
8		30	30
9		60	38
10	6	5	18
11		30	44
12		60	75

^aCondition: **ARAR2** (0.94 mmol), $FeCl_3$ (6-15 eq.), dried CH_2Cl_2 , CH_3NO_2 at 0 °C under nitrogen atmosphere

3.2 Optical property

The photophysical properties in dichloromethane at room temperature of **ARAR2** and **ARAR3** were studied in UV-visible region. The results showed that the similar absorption spectra of both compounds were obtained at the maximum absorption and shoulder peaks at 335 and 380 nm, respectively. They were assigned to $\pi-\pi^*$ transition of benzo[*d,e*]chromene core. Interestingly, the different maximum emission wavelengths were obtained at 476 and 500 nm, respectively. They located in the green emission region in Figure 2. The results indicated that the red-shifted of **ARAR3** molecule was related to the planar structure.

3.3 Thermal properties

The TGA spectra in Figure 3. The results found that the thermal stability of **ARAR3** exhibited high decomposition temperature at 269 °C compared with **ARAR2** due to the rigidity.⁹

The HOMO and LUMO and energy levels were estimated from the absorption spectra and the electrochemical data performance and UV-visible absorption spectra.¹⁰ From Table 2, the **ARAR3** showed the smaller band gap (2.75 eV) compared with **ARAR2** due to a long π -conjugated systems which the HOMO and LUMO levels located at -5.04 and -2.21 eV, respectively.

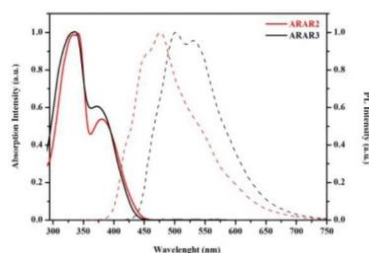


Figure 2. Normalized absorption (solid line) and emission (dash line) spectra of compounds in CH_2Cl_2 solution

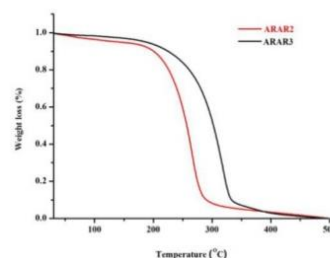


Figure 3. TGA spectra of compounds

Table 2. Photophysical and electrochemical characteristics of compounds

Compound	$\lambda_{\text{max,abs}}^a$ (nm)	$\lambda_{\text{max,em}}^a$ (nm)	λ_{onset}^a (nm)	E_g^b (eV)	$E_{\text{HOMO}}^{c,d}$ (eV)	E_{LUMO}^e (eV)
ARAR2	342	476	448	2.77	-5.07	-2.23
ARAR3	335	500	450	2.75	-5.04	-2.21

^aMeasured in dichloromethane (1×10^{-6} M)

^bEstimated from the onset of the absorption spectra ($E_g = 1240/\lambda_{\text{onset}}$)

^cMeasured in acetonitrile containing 0.1 M n-Bu₄NPF₆ as a supporting electrolyte at a scan rate of 100 mV/s

^dCalculated from HOMO = $-(E_{\text{ox}} + 4.8\text{eV} - E_{\text{ox}}(\text{ferrocene}))$; $E_{\text{ox}}(\text{ferrocene}) = 0.44$ V

^eCalculated from LUMO = HOMO + E_g

4. Conclusion

We studied the intramolecular Scholl reaction to obtain tribenzo[*a,c,k,l*] xanthene by using FeCl_3 as the coupling reagent. The product showed the red-shifted emission as well as high thermal stability. The results showed that the ARAR3 was quite promising to be widely useful organic material in the future.

Acknowledgements

The authors would like to acknowledge the financial support from Ubon Ratchathani University and Science Achievement Scholarship of Thailand (SAST) for Thikhamporn Uppalabat.

References

- Grzybowski, M.; Skonieczny, K.; Butenschön, H.; Gryko, D. T. *Angew. Chem. Int. Ed.* **2013**, *52*, 9900–9930.
- Narita, A.; Wang, X.-Y.; Feng, X.; Müllen, K. *Chem. Soc. Rev.* **2015**, *44*, 6616–6643.
- Sarhan, A. A.; Bolm, C. *Chem. Soc. Rev.* **2009**, *38*, 2730–2744.
- Chai, W.-Y.; Yang, E.-Q.; Zhang, Y.-L.; Xie, A.-L.; Cao, X.-P. *Synthesis* **2012**, *44*, 439–445.
- Tasior, M.; Kim, D.; Singha, S.; Krzeszewski, M.; Ahn, K. H.; Gryko, D. T. *J. Mater. Chem. C* **2015**, *3*, 1421–1446.
- Thirunavukkarasu, V. S.; Donati, M.; Ackermann, L. *Org. Lett.* **2012**, *14*, 3416–3419.
- Wöhrle, T.; Kirres, J.; Kaller, M.; Mansueto, M.; Tussetschläger, S.; Laschat, S. *J. Org. Chem.* **2014**, *79*, 10143–10152.
- Zhao, K.-Q.; Du, J.-Q.; Long, X.-H.; Jing, M.; Wang, B.-Q.; Hu, P.; Monobe, H.; Henrich, B.; Donnio, B. *Dyes and Pigments* **2017**, *143*, 252–260.
- Chu, Z.; Wang, D.; Zhang, C.; Fan, X.; Tang, Y.; Chen, L.; Zou, D. *Macromol. Rapid Commun.* **2009**, *30*, 1745–1750.
- Keawin, T.; Prachumrak, N.; Namuangruk, S.; Pansay, S.; Kungwan, N.; Maensiri, S.; Jungstittiwong, S.; Sudyoadsuk, T.; Promarak, V. *J. RSC Adv.* **2015**, *5*, 73481–73489.

CURRICULUM VITAE

NAME	Miss Thikhamporn Uppalabat
BIRTH DATE	07 March 1994
BIRTH PLACE	UbonRatchathani, Thailand
EDUCATION	2012-2018, B. Sc. Chemistry, Department of Chemistry, Faculty of Science, Ubon Ratchathani University
SCHOLARSHIP	Human Resource Development in Science Project (Science Achievement Scholarship of Thailand, SAST) program
RESEARCH GROUP	Organometallic and Catalytic Center (OCC)